NONLINEAR RESPONSE MODELING OF LOW-RISE STRUCTURAL WALLS

by

Simon Karabulut

B.S., Civil Engineering, Boğaziçi University, 2012

Submitted to the Institute for Graduate Studies in
Science and Engineering in partial fulfillment of
the requirements for the degree of
Master of Science

Graduate Program in Civil Engineering

Boğaziçi University

2016

NONLINEAR RESPONSE MODELING OF LOW-RISE STRUCTURAL WALLS

APPROVED BY:

Assoc. Prof. Kutay Orakçal (Thesis Supervisor)	.....
Prof. Hilmi Lus	.....
Prof. Alper Ilki	.....

DATE OF APPROVAL: 11.01.2016

To my mother,

ACKNOWLEDGEMENTS

This thesis would not have been possible without the support of Assoc. Prof. Kutay Orakçal. I would like to thank for his precious guidance and help during the preparation of the thesis. I would like to acknowledge his patience and his positive approach during the impasse moments of my studies.

I would like to express my special thanks to my colleagues M. Fethi Güllü and Burak Horoz for their support during the implementation process of models.

I would also like to express my thanks to my friends Selahattin Akalp, Sarper Saygi, and Mustafa Sekman for their help in the preparation of this thesis.

I would also like to thank Leonardo M. Massone from University of Chile and Tevfik Terzioglu from Texas A & M University for providing the experimental data.

Most of all, I would like to express my special thanks to my family for their invaluable support. I cannot compensate their patience, belief and love.

ABSTRACT

NONLINEAR RESPONSE MODELING OF LOW-RISE STRUCTURAL WALLS

A finite element modeling approach was validated and improved in this study, for simulating the behavior of reinforced concrete structural walls with aspect ratios of 1.0 or less, whose behavior is governed by shear deformations as well as interaction between shear and flexural responses. To validate the model, a total of fifteen squat structural walls were calibrated and analyzed using Matlab. Mechanisms of shear aggregate interlock in concrete and dowel action on reinforcing bars were explicitly incorporated in model formulation, and cyclic degradation parameters associated with these mechanisms were implemented in model for better representation of the in-plane hysteretic lateral load behavior of squat structural walls. The effect of strain penetration within the wall foundation was considered in the model predictions, to capture the initial stiffness and lateral load capacity of the walls in early drift levels more accurately. Refined constitutive models were used in the model formulation to represent the hysteretic stress-strain behavior of reinforcing steel and concrete. Features of the experimental conditions, such as loading under double-curvature or single-curvature, or presence of a weakened plane joint in the wall, were represented in the model calibration and analysis conditions. Analytical predictions of the lateral load vs. displacement responses obtained using the finite element model were compared with the experimental measurements. Comparisons revealed that the model reasonably predicts the overall lateral load vs. displacement behavior, as well as important response attributes such as the initial stiffness, lateral load capacity, cyclic strength and stiffness degradation, and pinching characteristics of the walls investigated. While subject to further refinement, the analytical model in its current improved form is shown to be a feasible candidate for simulating the hysteretic lateral load behavior of squat structural walls.

ÖZET

BODUR PERDE DUVARLARIN DOĞRUSAL OLMAYAN DAVRANIŞLARININ MODELLENMESİ

Bu çalışma kapsamında boy/en oranı 1.0 ve daha az olan perde duvarların davranışını irdelemek üzere bir sonlu eleman modelleme yöntemi kullanılmış, kullanılan model deney sonuçları ile doğrulanmış ve geliştirilmiştir. Yatay yük davranışı kayma ve eğilme davranışlarının etkileşiminin yanısıra çoğunlukla kayma deformasyonları tarafından etkilenen bodur perde duvarların modellenmesi kapsamında bu çalışmada on beş adet bodur duvar numunesi irdelenmiştir. Kullanılan model, incelenen deney numuneleri için kalibre edilmiş ve Matlab ortamında analiz edilmiştir. Modelde betonda agrega kenetlenmesi ve donatıda kama etkisi mekanizmaları iyileştirilmiş, bu mekanizmalar ile ilişkili çevrimsel dayanım azalması parametreleri modele işlenerek perdelerin çevrimsel yanal yük davranışının daha doğru temsil edilmesi amaçlanmıştır. Model sonuçları ile deney sonuçlarının karşılaştırılmasında perde temellerindeki gerinim penetrasyonu etkileri gözetilmiş, böylelikle perdelerin başlangıç rijitliği ve düşük öteleme oranlarında yanal yük kapasitesinin daha doğru temsil edilmesi hedeflenmiştir. Modelde beton ve donatı çeliği için kapsamlı gerilme-şekil değiştirme bağıntıları kullanılmıştır. Tekil ya da çift eğrilik altında yanal yükleme ve perde numunesindeki zayıflatılmış kesit bölgeleri gibi deneysel koşullar model kalibrasyonunda ve analiz koşullarında gözetilmiştir. Model sonuçları, perdelerin deneysel olarak elde edilmiş olan yanal yük-öteleme davranışları ile karşılaştırılmıştır. Sunulan karşılaştırmalar ışığında analitik modelin incelenen perde numunelerinin çevrimsel yanal yük-yerdeğiştirme davranışını, başlangıç rijitliğini, yanal yük kapasitesini, döngüsel kapasite/rijitlik bozunması ve orijin bölgesinde daralma gibi özellikleri makul doğruluk ile kestirebildiği gözlemlenmiş, iyileştirilmiş hali ile kullanılan analitik modelleme yönteminin bodur perde duvarların çevrimsel yanal yük davranışının kestirimi için uygun bir yaklaşım olduğu gösterilmiştir.

TABLE OF CONTENTS

ACKNOWLEDGEMENTS iv
ABSTRACT v
ÖZET vi
LIST OF FIGURES ix
LIST OF TABLES xv
LIST OF SYMBOLS xvii
LIST OF ACRONYMS/ABBREVIATIONS xx
1. INTRODUCTION 1
1.1. General 1
1.2. Literature Review 3
1.3. Objectives and Scope 13
1.4. Thesis Outline 14
2. MODEL DESCRIPTION 15
2.1. Overview 15
2.2. Constitutive Panel Model 16
2.3. Constitutive Material Models 19
2.3.1. Constitutive Model for Reinforcement 19
2.3.2. Constitutive Model for Concrete 20
2.3.3. Constitutive Modeling of the Shear Aggregate Interlock Effect in Concrete 22
2.3.4. Constitutive Modeling of Dowel Action on Reinforcing Bars . . 24
2.3.5. Constitutive Modeling of Cyclic Degradation in Shear Aggregate Interlock and Dowel Action 27
2.3.6. Consideration of the Strain Penetration Effect 29
2.4. Finite Element Modeling Methodology 31
2.4.1. 4 Nodes, 8 Degree of Freedom Rectangular Element 32
2.4.2. Finite Element Model Stiffness Assembly 33
2.4.3. Internal Force Vector Assembly 34
2.4.4. Support Conditions and Constraints 35

2.4.5. Nonlinear Analysis Solution Strategy 36
3. EXPERIMENTAL CALIBRATION OF THE MODEL 39
3.1. Description of the Wall Specimens 39
3.1.1. Wall Specimens Tested at University of California Los Angeles . 39
3.1.2. Wall Specimens Tested at Boğaziçi University 43
3.2. Test Setup 48
3.3. Material Properties 51
3.4. Failure Modes of the Wall Specimens 54
3.5. Calibration of the Model for the Wall Specimens 55
3.5.1. Calibration of Model Element Dimensions and Reinforcement Ratios 55
3.5.2. Calibration of Constitutive Material Parameters 56
3.5.2.1. Calibration of the Constitutive Model for Reinforcing Steel 57
3.5.2.2. Calibration of the Constitutive Model for Concrete . . 63
4. COMPARISON OF ANALYTICAL AND EXPERIMENTAL RESULTS . . 71
4.1. Wall Specimens Tested at University of California Los Angeles 71
4.2. Wall Specimens Tested at Boğaziçi University 77
4.3. Overview 86
5. SUMMARY AND CONCLUSIONS 87
5.1. Overview 87
5.2. Conclusions 87
5.3. Recommendations for Future Studies 88
REFERENCES 90

LIST OF FIGURES

Figure 1.1. Coupled Model Element (Massone *et al.*, 2006, 2009). 5

Figure 1.2. Element Models. 6

Figure 1.3. Transfer Mechanism in Cracked RC Members (Ince *et al.*, 2006). . 8

Figure 2.1. Uncracked Behavior of Concrete in the FSAM (Orakcal *et al.*, 2012). 16

Figure 2.2. Behavior of Concrete after the First Crack Formation in the FSAM (Orakcal *et al.*, 2012). 17

Figure 2.3. Behavior of Concrete after the Second Crack Formation in the FSAM (Orakcal *et al.*, 2012). 18

Figure 2.4. Constitutive Model for Reinforcing Steel (Menegotto and Pinto, 1973). 19

Figure 2.5. Constitutive Model for Concrete (Chang and Mander, 1994). . . . 20

Figure 2.6. Compression Softening Effects Implemented in the Panel Model (Ulugtekin, 2010). 22

Figure 2.7. (a) Friction Based Constitutive Model for Shear Aggregate Interlock (Orakcal *et al.*, 2012), (b) Shear Friction Mechanism along a Crack in ACI-318. 23

Figure 2.8. Dowel Action of a Reinforcement Bar Crossing a Crack (He and Kwan, 2001). 26

Figure 2.9. Cracked Concrete Elements Containing a Reinforcement Bar Running (a) in the x-direction and (b) in the y-direction Crossing the Cracks at Acute Angle (He and Kwan, 2001). 27

Figure 2.10. Response to Cyclic Loading, (a) Friction (b) Dowel (Kappos *et al.*, 2011). 28

Figure 2.11. Calculation and Update of the Degradation Factor and Envelopes for Dowel Action (Kappos *et al.*, 2014). 28

Figure 2.12. Origin-Oriented Model for Dowel Action. 29

Figure 2.13. Strain Penetration Model (Massone *et al.*, 2009). 30

Figure 2.14. Effect of Strain Penetration. 31

Figure 2.15. Tangent Stiffness (Elasticity) Matrix Calculation Path. 33

Figure 2.16. Global and Local DOFs for a Wall Model. 34

Figure 2.17. Stress Vector Calculation Path. 34

Figure 2.18. Numeration of Internal Forces for a Mesh. 35

Figure 2.19. Conversion of DOFs after the Assignment of Body Constraint (Gullu, 2013). 36

Figure 2.20. Representation of the Nonlinear Analysis Solution Strategy for a Single Degree of Freedom System (Clarke and Hancock, 1990). . . 37

Figure 2.21. Iterative Strategy and Residual Displacements (Clarke and Hancock, 1990). 38

Figure 3.1. Specimen Name Description for Tests Conducted at UCLA. 40

Figure 3.2. Weakened Plate Joint on Wall Spandrels (Massone *et al.*, 2009). . 41

Figure 3.3. Wall Spandrel Geometry and Reinforcement (Massone *et al.*, 2009). 42

Figure 3.4. Geometry and Steel Reinforcement for Wall Piers (Massone *et al.*, 2009). 43

Figure 3.5. Specimen Name Description for Tests Conducted at Boğaziçi University. 43

Figure 3.6. Geometry and Wall Reinforcement of Specimen T1-S1 (Terzioglu, 2011). 46

Figure 3.7. Geometry and Wall Reinforcement of Specimen T3-S1 (Terzioglu, 2011). 47

Figure 3.8. Geometry and Wall Reinforcement of Specimen T5-S1 (Terzioglu, 2011). 48

Figure 3.9. Test Setup (Massone, 2006). 49

Figure 3.10. Displacement History (Massone, 2006). 49

Figure 3.11. Test Setup (Terzioglu, 2011). 50

Figure 3.12. Steel Tensile Stress-Strain Curves for ϕ 13 and ϕ 16 bars of Type 1 Wall Specimen (Massone, 2006). 51

Figure 3.13. Steel Stress-Strain Curves for Specimen Set 1 (Terzioglu, 2011). . 53

Figure 3.14. Steel Stress-Strain Curves for Web Reinforcement of Specimen Set 2 and Set 3 (Terzioglu, 2011). 53

Figure 3.15. Steel Stress-Strain Curves for Boundary Reinforcement of Specimen Set 2 and Set 3 (Terzioglu, 2011). 53

Figure 3.16. The Stress-Strain Behavior of Bare Rebar and Rebar Embedded in Concrete. 57

Figure 3.17. Stress-Strain Relationship for a Bar Embedded in Concrete (Belarbi and Hsu, 1994). 58

Figure 3.18. Compression and Tension Envelope Curves of the Model by Chang and Mander (1994). 64

Figure 3.19. Stress-Strain Diagrams for Concrete in Compression for WS-T3-S2. 66

Figure 3.20. Stress-Strain Relationship for Concrete in Tension (Belarbi and Hsu, 1994). 68

Figure 3.21. Stress-Strain Diagrams for Concrete in Tension for SW-T2-S1-1. . 69

Figure 4.1. Lateral Load - Top Displacement Response of Specimen WS-T1-S1. 72

Figure 4.2. Lateral Load - Top Displacement Response of Specimen WS-T1-S2. 73

Figure 4.3. Lateral Load - Top Displacement Response of Specimen WS-T2-S2. 74

Figure 4.4. Lateral Load - Top Displacement Response of Specimen WS-T3-S1. 75

Figure 4.5. Lateral Load - Top Displacement Response of Specimen WP-T5-N0-S1. 76

Figure 4.6. Lateral Load - Top Displacement Response of Specimen WP-T5-N5-S1. 76

Figure 4.7. Lateral Load - Top Displacement Response of Specimen WP-T5-N10-S2. 77

Figure 4.8. Lateral Load - Top Displacement Response of Specimen SW-T1-S1-2. 78

Figure 4.9. Lateral Load - Top Displacement Response of Specimen SW-T1-N5-S1-10. 79

Figure 4.10. Lateral Load - Top Displacement Response of Specimen SW-T1-N10-S1-11. 79

Figure 4.11. Lateral Load - Top Displacement Response of Specimen SW-T2-S1-1. 80

Figure 4.12. Lateral Load - Top Displacement Response of Specimen SW-T2-S3-4. 81

Figure 4.13. Lateral Load - Top Displacement Response of Specimen SW-T4-S1-6. 81

Figure 4.14. Lateral Load - Top Displacement Response of SW-T6-S1-7. 82

Figure 4.15. Lateral Load - Top Displacement Response of SW-T3-S1-5 (Original Model). 84

Figure 4.16. Lateral Load - Top Displacement Response of SW-T3-S1-5 (Concrete Friction Coefficient in Shear Aggregate Interlock Mechanism Reduced in the Model). 84

Figure 4.17. Peak-Oriented Model for Contribution of Reinforcing Steel on Shear Aggregate Interlock. 85

Figure 4.18. Lateral Load - Top Displacement Response of SW-T3-S1-5 (Peak-Oriented). 85

LIST OF TABLES

Table 3.1. Test Specimen Details for Tests Conducted at UCLA. 41

Table 3.2. Test Specimen Details for Tests Conducted at Boğaziçi University. 44

Table 3.3. Average Compressive Strength of Concrete (Massone, 2006). 52

Table 3.4. Average Compressive Strength of Concrete (Terzioglu, 2011). . . . 54

Table 3.5. Wall Model Geometry Details for Tests Conducted at UCLA. . . . 56

Table 3.6. Wall Model Geometry Details for Tests Conducted at Boğaziçi University. 56

Table 3.7. Calibrated Values of the Constitutive Parameters of Reinforcing Steel Bars for Specimens WS-T1-S1, WS-T1-S2, WS-T2-S1, and WS-T2-S2. 60

Table 3.8. Calibrated Values of the Constitutive Parameters of Reinforcing Steel Bars for Specimens WS-T3-S1, WS-T3-S2, WS-T4-S1, and WS-T4-S2. 60

Table 3.9. Calibrated Values of the Constitutive Parameters of Reinforcing Steel Bars for Specimens WP-T5-N0-S1, WP-T5-N0-S2, WP-T5-N5-S1, WP-T5-N5-S2, WP-T5-N10-S1, and WP-T5-N10-S2. 61

Table 3.10. Calibrated Values of the Constitutive Parameters of Reinforcing Steel Bars for Specimens SW-T2-S1-1, SW-T1-S1-2, and SW-T2-S2-3. 62

Table 3.11. Calibrated Values of the Constitutive Parameters of Reinforcing Steel Bars for Specimens SW-T2-S3-4, SW-T3-S1-5, SW-T4-S1-6, and SW-T5-S1-7. 62

Table 3.12. Calibrated Values of the Constitutive Parameters of Reinforcing Steel Bars for Specimens SW-T6-S1-8, SW-T1-S2-9, SW-T1-N5-S1-10, and SW-T1-N10-S1-11. 63

Table 3.13. Calibrated Values of the Constitutive Parameters for Concrete in Compression for the UCLA Specimens. 66

Table 3.14. Calibrated Values of the Constitutive Parameters for Concrete in Compression for the Boğaziçi University Specimens. 67

Table 3.15. Calibrated Values of the Constitutive Parameters for Concrete in Tension for the UCLA Specimens. 69

Table 3.16. Calibrated Values of the Constitutive Parameters for Concrete in Tension for the Boğaziçi University Specimens. 70

LIST OF SYMBOLS

A_g	Gross concrete cross-section area
B	Tension stiffening parameter for reinforcing steel
b	Strain hardening ratio for compression
b'	Strain hardening ratio for tension
d_i	Local nodal displacement
D_i	Global nodal displacement
D_b	Dowel diameter
$\{\mathrm{D}\}$	Global displacement vector
E_0	Modulus of elasticity of steel
E_c	Elastic modulus for concrete
E_p	Plastic (strain hardening) modulus for bare steel bars
E_p^*	Plastic (strain hardening) modulus for steel bars embedded in concrete
E_s	Elastic modulus for steel
$[E]$	Elasticity matrix
f_c'	Compressive strength of concrete
f_{cr}	Tensile cracking stress of concrete
F_D	Dowel force
F_{Deg}	Degradation in the dowel action
f_y	Yield stress of web reinforcement
f_{ult}	Ultimate stress of web reinforcement
$\{f\}$	Local internal force vector of one mesh
$\{F\}$	Global internal force vector
$[G]$	Strain matrix
$[G]^T$	Transpose of strain matrix
h_w	Height of wall
$[k]$	Local stiffness matrix of one mesh
$[K]$	Global stiffness matrix
l_d	Embedment length

l_w	Length of wall
h	Height of mesh
m	Mesh number in horizontal direction
n	Mesh number in vertical direction
R	Exponent controlling the transition between elastic and hardening region
r	Shape parameter of the compression envelope
s	Slip
s_f	Slip due to the friction
$s_{f,u}$	Maximum slip due to the friction
t	Thickness of wall
$[T]$	Transformation matrix for body constraint
$[T]^T$	Transpose of transformation matrix for body constraint
x_{crn}	Critical strain parameter of concrete in compression by Saatcioglu and Razvi Model
x_{crp}	Critical strain parameter of concrete in tension by Belarbi and Hsu Model
w	Width of mesh
$w/$	With
w/o	Without

ε_0	Strain at the intersection point of two asymptotes
ε_y	Yield strain of web reinforcement
ε_{ult}	Ultimate strain of web reinforcement
ε'_c	Strain of concrete at peak stress
ε_{un}	Unloading strain in shear aggregate interlock model
ε_p	Unloading strain in shear aggregate interlock model
ε_r	Plastic strain in shear aggregate interlock model
ε_r	Strain at the point of strain reversal

θ	Rotation
μ	Interface shear friction coefficient
σ_0	Stress at the intersection point of two asymptotes
σ	Concrete stress
σ_n	Normal clamping stress
$\sigma*_n$	Normal stress at tension stiffening
σ_r	Stress at the point of strain reversal
σ_s	Axial stress of bars
σ_y	Yield stress of reinforcing steel
ρ	Reinforcement area ratio
ρ_b	Boundary reinforcement ratio
ρ_l	Longitudinal reinforcement ratio
ρ_t	Transverse reinforcement ratio
τ_{agr}	Shear resistance of the aggregate interlock mechanism
τ_D	Shear stress resisted by dowel action in cracked reinforced concrete
τ_{deg}	Degradation in the aggregate interlock mechanism
τ_f	Friction resistance
$\tau_{f,l}$	Ultimate friction resistance at initial cycle
ξ	Normalized local coordinates of a mesh in x direction
η	Normalized local coordinates of a mesh in y direction
$\Delta\lambda$	Initial load increment
$\Delta\delta_n$	Initial displacement increment
$\Delta\delta$	Displacement increment
$\Delta\delta_R$	Residual displacement increment

LIST OF ACRONYMS/ABBREVIATIONS

ACI	American Concrete Institute
DOF	Degree of freedom
FEM	Finite element model
FSAM	Fixed strut angle model
MVLEM	Multiple-Vertical-Line-Element Model
RC	Reinforced Concrete
SFI	Shear Flexure interaction
UCLA	University of California Los Angeles

1. INTRODUCTION

1.1. General

Improving the seismic performance of reinforced concrete (RC) building-type structures with means to improve their lateral stiffness and lateral load capacity, promotes the use of structural walls. Structural walls are designed and detailed to provide adequate stiffness and strength, as well as sufficient ductility to attain favorable structural performance under moderate and severe earthquake demands. Codes and recommendations for design of new buildings enforce the walls to exhibit ductile flexural behavior, with sufficient shear capacity to prevent brittle failures. Experimental studies have shown that well designed and detailed slender walls exhibit failure under flexure, and shear failure is not expected. Squat walls, on the other hand, are susceptible to fail in shear, which results in early loss of lateral strength and stiffness. Hence, to characterize and to analytically represent the behavior of medium-rise or squat structural walls under earthquake actions is a significant area of research, towards a more reliable design and performance of buildings incorporating such walls.

The so-called aspect (height-to-width) ratio (h_w/l_w) is commonly used to classify structural walls. Shear behavior governs the response of structural walls with aspect ratios less than 1.0-1.5 (squat structural walls), whereas for structural walls with aspect ratios exceeding 2.5-3.0 (slender structural walls), flexural actions predominantly control the wall response. For structural walls with moderate aspect ratios (between 1.5 and 2.5), both flexural yielding and nonlinear shear deformations (which are usually coupled) contribute to wall behavior. For such walls, nonlinear shear deformations can constitute up to 30% to 50% of lateral wall displacements, as investigated experimentally by Tran and Wallace (2012). Reliable behavioral modeling of such structural walls with predominant shear-flexure interaction (SFI) behavior is of particular interest, especially because fiber-based modeling methodologies commonly used in practice for performance-based design of buildings typically consider uncoupled shear and flexural response components. However, analytical models with uncoupled axial, flexure, and

shear responses are shown by previous research to underestimate compressive strains even in relatively slender RC walls controlled by flexure (Orakcal and Wallace, 2006), and overestimate the lateral load capacity of RC walls with moderate aspect ratios (Tran, 2012) and low aspect ratios (Massone *et al.*, 2006). So, there is a need for relatively simple modeling approaches that consider interaction (coupling) between axial, flexural, and shear responses, and capture important hysteretic response features for a wide range of wall geometries and reinforcing details.

The lateral load behavior of structural walls controlled by nonlinear flexural deformations has been investigated both experimentally and analytically by numerous researchers. The lateral force versus deformation response of slender walls in flexure can be captured reasonably well using simple (moment-curvature based) analytical models and improved predictions can be obtained using more detailed (fiber-based) models. However, research focusing on the nonlinear shear behavior and interaction between nonlinear shear and flexural responses of walls is based on various assumptions and simplifications, and are subject to limitations. There is still a need for a reliable and generalized, yet relatively simple modeling approach that can simulate the coupled flexural and shear responses of walls with various geometries and aspect ratios. Therefore, the primary objective of this study was to provide a robust yet practical modeling approach for representing the nonlinear shear behavior as well as the interaction between nonlinear shear and flexural responses of walls.

Accordingly, the finite element modeling methodology developed by Gullu (2013) was adopted and improved in this study for simulating the response of squat walls with coupled shear and flexural responses. The behavior of the constitutive panel elements in the finite element model formulation is described by a previously-developed constitutive relationship named as the Fixed-Strut-Angle Model (Ulugtekin, 2010). Improved constitutive models for shear aggregate interlock and dowel action mechanisms were implemented in the constitutive model formulation for simulating the transfer of shear stress across cracks. The finite element wall model with the improved constitutive formulation was calibrated for wall specimens with low aspect ratios, where coupled flexural yielding and nonlinear shear deformations were observed, resulting in reduced

lateral stiffness, strength and ductility. The model was calibrated for the squat wall specimens tested by Massone (2006), Orakcal *et al.*, (2009), and Terzioglu (2011), and model predictions were compared with the experimentally-observed hysteretic lateral load vs. displacement responses.

1.2. Literature Review

Numerous experimental and analytical studies are available in the literature that investigate the lateral load behavior of slender structural walls, the response of which is governed by nonlinear flexural deformations. On the contrary, relatively few analytical studies focus on squat structural walls, whose behavior is controlled by nonlinear shear deformations as well as interaction (coupling) between shear and flexural responses.

Squat walls are very common in low-rise construction and basement levels of tall buildings, and are likely to experience multiple deformation cycles exceeding yield in maximum earthquake action. Identification of the response and failure modes of squat walls plays a significant role in the design of RC systems as well as in the modeling of such walls. Experimental approaches showed that shear contribution to displacement of squat walls exceed the estimations using elastic shear response (Massone, 2006).

In the past 60+ years, various experimental studies on squat RC walls have been conducted. First monotonic loading tests were conducted at Massachusetts Institute of Technology and Stanford University (Galletly 1952, Benjamin and Williams 1953), which focused on the shear strength of walls with barbell cross-sections. Cyclic tests were also conducted on squat walls in Japan (Hirosawa, 1975) and in the United States (Barda, 1972). Although extensive experimental work was conducted throughout this period, code provisions and building manuals do not correlate well with the experimental data (Wood, 1990).

As shear deformations significantly contribute to the response of squat walls, their failure modes are typically associated with shear. Paulay and Priestley (1992) stated that there are three types of shear failure observed in squat walls. These failure

types are diagonal tension, diagonal compression, and sliding shear. The failure mode is considered mixed if the flexural strength is achieved by the wall followed by a shear failure. Mixed failure is more common in walls with aspect ratios between 1.0 and 2.0 (Gulec, 2009). The behavior and failure type of squat walls are also affected by design parameters such as vertical and horizontal web reinforcement, wall geometry, and axial force.

Diagonal tension failure is generally observed in squat walls with light horizontal web reinforcement. One or more cracks form with respect to loading direction and damage is concentrated in the inclined cracks rather than the overall wall web. The orientation of failure plane is assumed to form at approximately 45° and the web reinforcement yield as cracks widen and displacement demand increases on the reinforcement. If adequate horizontal web reinforcement is provided detailing the wall, inclined cracks open and close with successive cyclic loading. This process deteriorates the concrete compression struts in the web and crushing of these struts results in diagonal compression failure. Sliding shear failure, on the other hand, is a phenomenon when a heavily reinforced wall is subjected to large number of displacement cycles. It is a result of concrete crushing as in diagonal compression failure. Inclined shear cracking forms in sliding shear failure and the inclined cracks intersect with displacement cycles leading to the deterioration of concrete within these cracks. Since the wall is heavily reinforced, damage is spread on the overall wall web and a weakened horizontal plane is formed near the base. Sliding shear is associated with the sliding of the upper part of the wall on this weakened plane.

An analytical model should consider contributions from both shear and flexure into the wall response. Flexural response was simulated by numerous researchers for RC walls using uniaxial stress-strain relationships for concrete and steel. This approach does not consider shear-flexure interaction (SFI) which results in variations from experimental data not only for squat walls but also for slender walls which are mainly governed by flexure. Interaction between shear and flexure was first experimentally observed by Oesterle *et al.*, (1976) for moderately slender walls. The experimental data indicated that nonlinear deformations in shear and flexure occurred almost simul-

taneously which confirmed the coupling of shear and flexure.

Several analytical approaches were presented regarding the uncoupled flexure and shear interaction. The majority of these models neglect or underestimate the influence of the shear-flexure interaction, which influences the response even for slender walls. In late 1990s, Petrangeli (1999) introduced a fiber-based (multi-spring) model approach into RC panel behavior to incorporate the interaction among nonlinear axial, flexural, and shear responses of RC walls. Massone *et al.*, (2006, 2009) assigned shear springs to each uniaxial element and modified original Multiple-Vertical-Line-Element Model (MVLEM) proposed by Vulcano *et al.*, (1988) such that each element is treated as a RC panel element subjected to in-plane uniform normal and shear stresses (Figure 1.1). A rotating-angle modeling approach, such as the Modified Compression-Field Theory (MCFT; Vecchio and Collins, 1986) or the Rotating-Angle Softened-Truss-Model (RA-STM; Hsu, 1993; Belarbi and Hsu, 1994 and 1995; Pang and Hsu, 1995), was used to model the constitutive panel behavior. The assumptions that form the model are as follows: Plane section remains plane, strain fields acting on concrete and reinforcing steel are identical (perfect bond between reinforcement and concrete), shear strains are uniformly distributed along the wall length, principal stress and strain directions coincide, and dowel action of reinforcement is equal to zero.

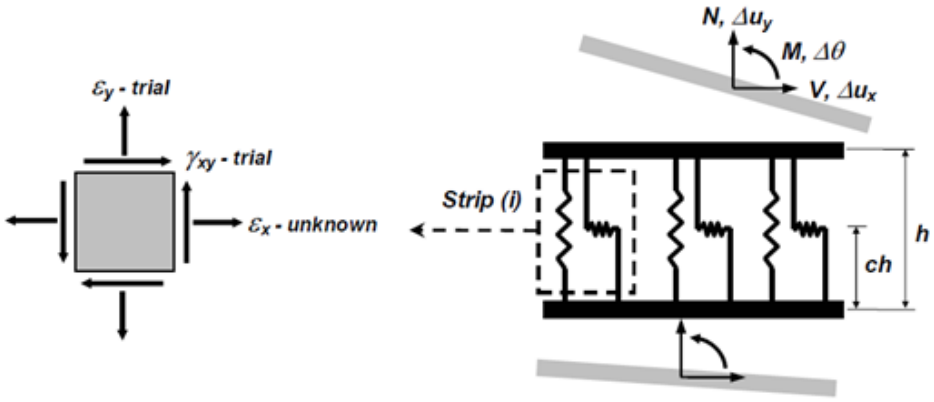

Figure 1.1. Coupled Model Element (Massone *et al.*, 2006, 2009).

Kolozvari *et al.*, (2012) introduced a new cyclic shear-flexure interaction modeling approach in 2012. Experimental data obtained by Tran and Wallace (2012) were used

to validate the analytical model. The experimental study included five one-third scale cantilever RC wall specimens which were heavily instrumented to gain detailed response information. The walls were subjected to reversed cyclic lateral loading applied at the top of the walls with a constant axial load. The test program aimed to obtain the influence of level of axial stress and average shear stress on the wall failure modes and lateral deformation capacity as well as the magnitude and distribution of lateral deformations related with shear and flexure. For walls with moderate aspect ratios, the shear-interaction model predicted the response reasonably accurately. In the proposed model, each uniaxial element from the original formulation of the MVLEM is replaced with a RC panel element subjected to membrane actions (Figure 1.2c). Based on the Fixed-Strut-Angle-Model (FSAM) developed by Ulugtekin (2010) and extended by Orakcal *et al.*, (2012), a 2D constitutive RC panel model formulation was adopted to describe shear aggregate interlock effects for the RC panel elements under reversed cyclic loading conditions. The coupling of axial and shear responses is thus enabled at the panel (macrofiber) level, which further allows coupling of flexural and shear responses at the model element level. The model differentiates from the one proposed by Massone *et al.*, (2006) in terms of its capability to simulate cyclic responses as well as the monotonic ones. Detailed information about the approach can be found in the papers proposed by Kolozvari *et al.*, (2014).

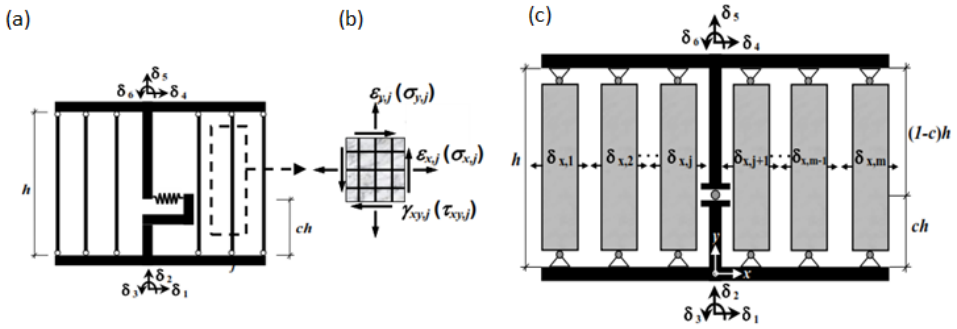

Figure 1.2. Element Models (a) Original MVLEM element, (b) RC panel element, (c) SFI-MVLEM element (Kolozvari *et al.*, 2014).

One of the most recent finite element modeling approach to investigate the inelastic response of RC walls under reversed-cyclic loading was proposed by Gullu (2013).

The fixed-crack-angle modeling approach was implemented due to its ability to be used for reversed cyclic loading conditions. The apprehension of the unexpected shear yielding and nonlinear deformation behavior in slender RC walls are targeted with this modeling approach. The analytical model successfully captured the stiffness degradation, shape of the load-displacement hysteresis loops, plastic displacements, and pinching behavior in slender walls. On the other hand, the model was validated for slender walls, which do not exhibit significant shear-flexure interaction behavior. Shear-aggregate-interlock effects in concrete were implemented in the model, which contributed to the shear stress transfer mechanism across the cracks. Later, Orendil (2014) proposed a new constitutive relationship for the dowel action on reinforcing steel bars and investigated the lateral load responses of squat RC walls with predominantly shear-controlled responses. The model reasonably predicted the experimentally-observed wall responses. Horoz (2015) implemented an origin oriented dowel model for reinforcing bars and introduced a revised constitutive model to represent shear-aggregate-interlock effects in concrete. The accuracy of the model implemented was calibrated for medium-aspect-ratio walls and global and local responses were captured fairly accurately, although the model did not capture failure modes associated with bar buckling and sliding shear failure.

As aforementioned, shear-flexure interaction behavior constitutes a significant response characteristic of RC walls. Therefore, shear effects which lead to behavioral phenomena such as multi-axial stress conditions, interlocking of cracks, and dowel action have been important areas of research. Across a crack, shear forces are transmitted by either through the interaction between rough surfaces of the crack (aggregate interlock mechanism) and through reinforcement crossing the crack (dowel action) (Maekawa and Qureshi, 1997). The relative contributions are affected by the geometry of the member, the arrangement of the loads applied, the reinforcement pattern, and the crack pattern. The contributions scatter through changes in internal stress distributions as concrete cracks and reinforcement bars yield (He and Kwan, 2001). Figure 1.3 shows a typical cracked member with shear transfer mechanisms illustrated.

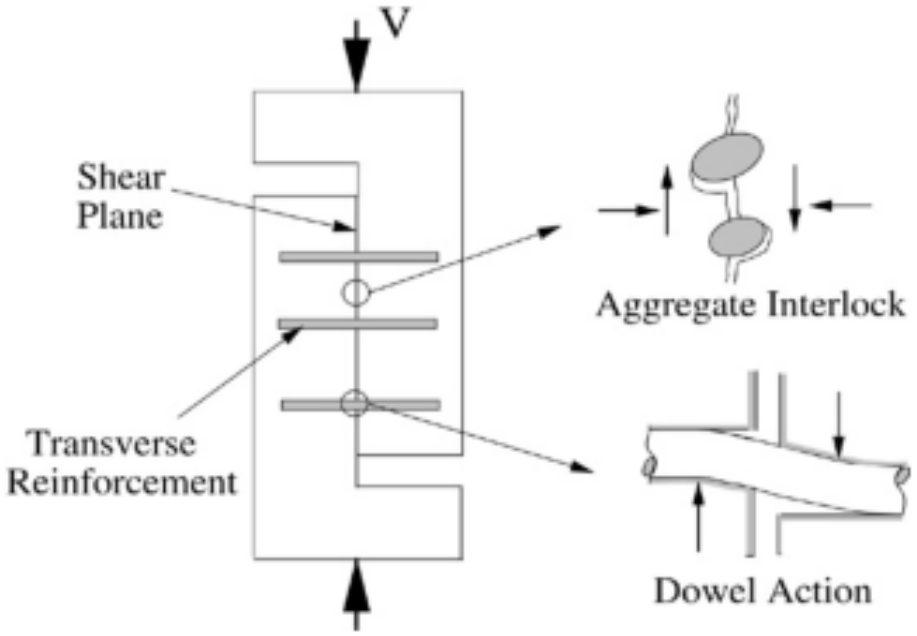

Figure 1.3. Transfer Mechanism in Cracked RC Members (Ince *et al.*, 2006).

Concrete-to-concrete friction (aggregate interlock) as a shear transfer mechanism has been the object of numerous experimental investigations. On the contrary, an analytical model to express aggregate interlock is complex because cracks tend to "dilate" as they slide due to aggregate particles sliding over each other (Sagaseta and Vollum, 2011). Hsu *et al.*, (1987) divided the transfer mechanism into two categories which are the transfer of shear across an uncracked plane and across an initially cracked plane. Transfer of shear across an uncracked plane implies cracks to produce in a direction inclined to the shear plane. Across an initially cracked plane, shear causes concrete segments to slip relative to each other which results in widening of the crack through roughness and irregularities that exist along the crack.

Mattock and Hawkins (1972) conducted monotonic loading tests on RC elements. In the tests, cracks that exist prior to shear loading was investigated. These cracks, which may form unrelated to shear such as due to tension forces caused by restrained shrinkage or temperature deformations, were found to reduce the ultimate shear transfer strength and increase slip at all loading stages. Additionally, for the initially cracked specimens with adequate reinforcement and large compressive stresses applied to the

shear plane, the cracks in the shear plane were displayed to "lock up" and shear transfer strength resembled the one with no initial cracks were present.

Walraven (1981) introduced analysis on aggregate interlock for initially cracked sliding planes. The cracks were studied at both micro and macro-roughness levels and the latter was shown to be the main shear transfer mode. Shear and normal stress transferred across the crack were quantified statistically. The equations were derived using slip and separation of the shear plane. Unlike Mattock and Hawkins (1972), these equations were derived for shear transferred through rather than the shear capacity of a member.

Bazant and Gambarova (1984) introduced the crack band model in which uniform distribution of the relative displacements across the crack exists over a certain specified width of the band.

Theodossius *et al.*, (1987) investigated the aggregate interlock phenomenon through experiments conducted for rough and smooth interfaces. For rough interfaces, it was presented that formation of cracks introduce significant decrease in shear stiffness, and as the surface deteriorates, the force-response deterioration is very high. The deterioration was found to increase with cycling though decrease in the maximum dilatancy was observed with increasing cycles.

Martin-Perez and Pantazopulou (1999) implemented a non-linear smeared-crack / smeared-reinforcement plain-stress model to investigate the dependence of shear resistance of RC elements on deformation demand. In the formulation, concrete was treated as and orthotropic material and the model was described using average stresses and average strains. The analytical results showed that with increased imposed deformation, shear strength degradation occurs and the cause of this degradation is mainly the susceptibility of concrete tensile and compressive strengths to increasing crack width.

Palieraki and Vintzileou (2009) did cyclic tests on RC specimens using two separate blocks casted at different times for each specimen. It was concluded that cyclically

imposed slips lead to significant degradation of the shear resistance of interfaces. The degradation was found to depend on the imposed cyclic slip and the anchorage length of the reinforcing bars in between the blocks.

As aforementioned, Massone *et al.*, (2009) implemented a rotating-angle modeling approach as panel behavior to represent the response of low-rise structural walls. The interaction between shear and flexure were integrated through neglecting dowel action on reinforcement and using only the uniaxial response of reinforcing bars while a constitutive stress-strain model was used for concrete. In the modeling, a rotational spring model was used to incorporate the effects of reinforcing bar extension within the foundation which was proved to improve the results in terms of stiffness and overall hysteretic behavior. Normal strains were also considered as the average horizontal normal strains measured during test rather than zero strain assumption. The comparisons were made at wall mid-heights and shown that experimental and analytical results have similarities. In a more recent attempt, Panagouli and Iordanidou (2013) applied a finite element analysis method to a shear wall which was constructed in Greece during the 70s with the assumption of that cracks already formed. Fractal theory was used to model cracks. The findings of the study included that cracked wall still has the capacity to sustain monotonic horizontal loading. In addition, with higher resolution of the interfaces, more accurate results can be obtained. As roughness of the contact interface plays an important role in the response, with lower resolution values, interlock between two faces of the crack is rather limited.

As stated above, another mechanism to transmit shear forces is through reinforcement crossing the crack. Until 80s, aggregate interlock was the only mechanism considered to transmit shear. In addition, from 1985 to 1991, modeling of the dowel action has never been mentioned in any of the papers due to the difficulties involved (Darwin, 1993). Mainly, there are three difficulties in addressing the dowel action. Firstly, the identification of the exact shear force transferred by dowel action within other components of shear transfer mechanisms is challenging. Secondly, the complicated nature of dowel action in a finite element analysis as it needs large number of elements. Finally, limitations of testing conditions in which post-peak range is required

to investigate the effects of dowel action (He and Kwan, 2001). However, the increase in the width of cracks under cyclic actions was shown to result in a substantial decrease of concrete-toconcrete friction along the tensioned zone and dowel action becomes the main contributor to the shear force transfer.

Vintzeleou and Tassios (1987) investigated the dowel action through experiments on three concrete blocks and concluded that under fully reversed deformations, stiffness degradation becomes significant and response degradation is important during the early loading cycles. An analytical model was also presented using the experimental data. In the model, the bar is assumed to behave like a horizontally loaded free-headed pile embedded in cohesive soil, and dowel yields simultaneously as the concrete crushes. The model uses the slip to calculate the dowel force.

Soroushian *et al.*, (1988) conducted cyclic tests to simulate dowel action of beam reinforcement at a cracked beam-column interface in reinforced concrete frames under earthquake excitation. The results showed that repeated inelastic load cycles severely decreases dowel bar stiffness and energy dissipation capacity. Additionally, the interface crack width increases with the repetition of inelastic load cycles.

Vintzeleou and Tassios (1990) introduced an analytical model to predict the reinforcing bars placed eccentrically in concrete cross section and loaded against the core of the section. Using two parameters, the top cover and the smaller side cover, the model was compared with experimental work done by the researchers. The shear displacement at failure was shown to increase with increase in the side cover of a reinforcing bar.

A micro scale model was proposed by Maekawa and Qureshi (1996b) to predict reinforcing bar response to axial pullout and transverse displacement. Axial pullout and dowel action were combined in the formulation. The monotonic model was extended to path-dependent cyclic model by Soltani and Maekawa (2008) which solves the nonlinear equilibrium and compatibility equations numerically to determine the deformational behavior of deformed bars with respect to the loading path and history.

The shortcoming of this model is that it is time consuming as it considers the deformed bar as three-dimensional member capable of developing coupled shears and moments as well as axial force.

In the dowel action model by He and Kwan (2001), the dowel effects on the reinforcing steel bars crossing cracks in concrete is represented in a smeared form in order to be compatible with the smeared crack model and smeared reinforcement model used in finite element analysis.

Ince *et al.*, (2006) studied the size effect of shear plane depth through experiments with push-off elements. The elements consisted of two concrete blocks connected by two parallel dowel bars which crossed shear plane at an angle. The results of the experimental work indicated that nominal strength at failure decreases as the specimen size increases. Using fracture mechanics, the contribution of the dowel action to the bearing capacity of cracked reinforced concrete elements was calculated. Additionally, the shear capacity of the dowel specimen was reported to increase with an increase in maximum aggregate size.

Husain *et al.*, (2009) tested eight specimens with initially cracked form to investigate the dowel resistance. It was reported that as the area or the number of dowel bars are increased, the slip tends to decrease due to the fact that the contribution of the bar stiffness to the overall section stiffness increases.

In a more recent study, Moradi *et al.*, (2012) proposed a macro scale model to simulate the behavior of deformed bars across RC cracks. The model is computationally efficient in attempt to be implemented in a smeared crack approach to analyze large-scale structures. The test results showed that significant stiffness degradation takes place during load reversals and it is more pronounced under fully reversed cyclic loading than repeated loading. The plastic displacement was reported to depend on the maximum applied shear and to have nonlinear relation under reversed cyclic loading.

1.3. Objectives and Scope

The lateral load behavior of structural walls has been an area of research both experimentally and analytically by many researchers, and there are numerous modeling approaches available in the literature that use various techniques for simulating their seismic response. However, most of the available modeling approaches focus on characterization of the nonlinear flexural response of walls, or coupling of nonlinear flexural deformations with moderate levels of shear deformation. Existing approaches to model coupled shear and flexural responses typically incorporate ad-hoc modeling assumptions, some of which have not been experimentally validated against experimental data obtained for squat walls with shear-controlled responses. There is still a need for a robust modeling approach to simulate the nonlinear hysteretic behavior of such walls.

Accordingly, the objective of this study is to experimentally-validate and improve a recently-developed finite element modeling methodology for simulating the in-plane hysteretic lateral load behavior of squat walls (with aspect ratios smaller or equal to 1.0), the response of which are governed by nonlinear shear deformations. The behavior of the constitutive panel (membrane) elements in the finite element model is described by a previously-developed constitutive panel model (i.e., the Fixed-Strut-Angle Model by Ulugtekin, 2010). Improvements were made on the constitutive panel model formulation for better representation of the shear-aggregate-interlock effects in concrete and dowel action in reinforcing bars, constituting the shear stress transfer mechanism across the cracks of the constitutive panel elements. The model was extensively calibrated for ten squat RC wall specimens tested by Massone (2006), four squat RC wall specimens tested by Orakcal *et al.*, (2009), and eleven wall specimens tested by Terzioglu (2011), and model predictions were compared with the experimentally-observed responses for fifteen squat wall specimens.

1.4. Thesis Outline

This thesis presents the modeling approach used, constitutive relationships incorporated in the model formulation, calibration of the model parameters, and comparison of the experimental and analytical results for low-rise RC walls. In Chapter 1, an introduction and a literature review, as well as the objectives and scope of this study are provided. Descriptions of constitutive panel model, the finite element modeling approach, and the shear transfer mechanisms across the cracks are presented in Chapter 2. Chapter 3 summarizes the test programs used for experimental validation of the model, as well as calibration of the model parameters. Chapter 4 focuses on comparison of model predictions and test results for the lateral load-displacement response of the squat wall specimens investigated. Finally, concluding remarks and recommendations for model improvements are presented in Chapter 5.

2. MODEL DESCRIPTION

2.1. Overview

This chapter describes the constitutive panel (membrane) model formulation used in this study, the constitutive material relationships implemented in the panel model, the macroscopic finite element modeling methodology used, and the constitutive relationships implemented to better represent transfer of shear stresses across cracks. Finite element modeling of RC structural walls involves assembling of constitutive panel elements for obtaining the overall model of a wall. To represent the behavior of the wall model, the combination of hysteretic nonlinear material relationships along crack directions of the constitutive panel, together with behavioral response characteristics including compression softening, tension stiffening, hysteretic biaxial damage, and shear stress transfer across cracks are used in combination.

The so-called Fixed Strut Angle Model (FSAM) proposed by Ulugtekin (2010) was selected as the constitutive panel model in the finite element model assembly. Its simple formulation and adequate accuracy makes it a feasible candidate for implementation. A summary of the FSAM formulation is provided in the next section, whereas detailed information on the FSAM is available in M.Sc. thesis by Ulugtekin (2010).

The present study adopts the formulation of the original FSAM with modifications. The effects of shear aggregate interlock and dowel action across cracks were neglected in the original FSAM. No dowel action assumption implies zero shear stresses developing along crack surfaces, through which significant overestimation of sliding shear strains along crack directions can take place. Formulations modified by Orakcal *et al.*, (2012), and later adopted by Gullu (2013), include a simple friction-based constitutive model to be implemented into the panel model to simulate the shear aggregate interlock effects in concrete. The shear aggregate interlock and nonlinear hysteretic constitutive relationship were adopted to represent the contribution of reinforcing bars (dowel action) to shear stresses developing along crack surfaces. Constitutive modeling

of shear aggregate interlock behavior in concrete and dowel effects on reinforcement in the present model formulation are presented in subsequent sections in detail.

2.2. Constitutive Panel Model

The original FSAM model incorporates perfect bond assumption between concrete and reinforcing steel bars, which is reasonable under favorable anchorage conditions. However, and importantly, it neglects shear aggregate interlock effects in concrete along crack surfaces, and dowel action on reinforcing bars. As the perfect bond assumption implies, the strain fields action on concrete component of a RC panel are assumed to be equal to that acting on reinforcing steel component. To construct the hysteretic constitutive modeling of reinforcing steel bars, uniaxial directions along the rebar directions are used whereas for the concrete stress-strain behavior, biaxial relations along the fixed strut (crack) directions are integrated. The biaxial stress-strain behavior of uncracked concrete is simulated in a similar fashion to the Modified Compression Field Theory (Vecchio and Collins, 1986) and the Rotating Angle Strut and Tie Model (Pang and Hsu, 1995) through utilization of a rotating strut approach. For the uncracked loading stages, a monotonic hysteretic behavior is assumed for concrete for small strains prior to cracking. The principal strains directions acquired from the applied strain field are assumed to coincide with principal stress directions in concrete. Consequently, the principal strain directions are used to apply the constitutive material model for concrete as seen from Figure 2.1.

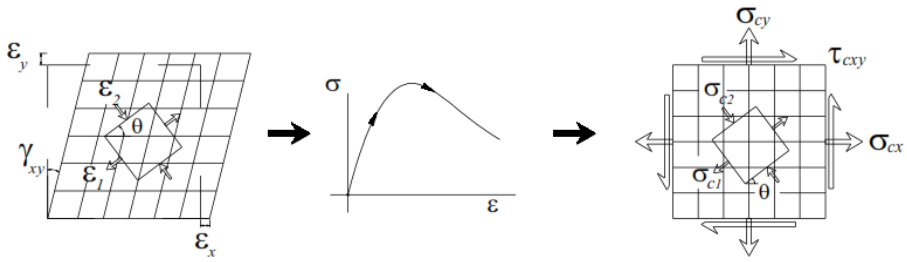

Figure 2.1. Uncracked Behavior of Concrete in the FSAM (Orakcal *et al.*, 2012).

When the cracking strain of concrete is exceeded by the principal tensile strain, the first crack forms in the RC panel in perpendicular direction to the principal tensile

strain. For subsequent loading, this implies that the first "Fixed Strut" direction is assigned, and it is parallel to the first crack. For subsequent loading stages, principle strain directions continue to rotate with the applied strain field whereas principal stress directions in concrete coincide with the first crack direction (parallel and perpendicular). As crack and principal stress directions coincide, zero shear stress develops along the crack directions, implying zero shear aggregate interlock and zero dowel action, which is the underlying assumption in the original FSAM formulation.

Following the formation of the first crack, the hysteretic stress-strain relationship for concrete is used in parallel and perpendicular directions to the fixed strut. Calculation of the principal stresses in concrete is only achievable through the transformation of the strain field into direction perpendicular and parallel to the fixed strut. The uniaxial model for concrete adopted enables the calculation of concrete stress values after the calculation of the strains that are perpendicular and parallel to the fixed strut direction. Biaxial compression softening and biaxial damage parameters reduce the calculated stresses. These parameters are described in the following section. The calculation of the stresses in reinforcing steel is acquired by the application of the hysteric uniaxial constitutive material model for reinforcing steel along the orthogonal rebar directions. The stresses developing in the concrete and reinforcing steel are superimposed to obtain the average stresses on the panel element. In Figure 2.2, concrete behavior after the formation of the first crack in FSAM is illustrated.

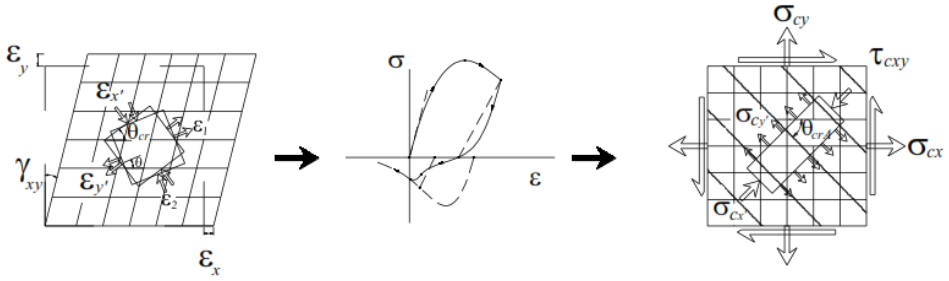

Figure 2.2. Behavior of Concrete after the First Crack Formation in the FSAM (Orakcal *et al.*, 2012).

The zero shear stress assumption (no dowel action) along the crack directions

dictates the second crack to form perpendicular to the first crack. The second crack forms as the tensile strain exceeds the cracking strain of concrete, upon unloading from compression. The constitutive behavior proceeds in the form of a single fixed strut mechanism until that stage. The perpendicularity of the first and second cracks is a modeling approach adopted in other constitutive panel model formulations and is referred as "orthogonal crack". The second "fixed strut" forms as the first and seconds cracks are perpendicular to each other. The loading direction dictates the fixed struts to work under tension or compression. For subsequent loading stages, principle stress directions are fixed along the fixed strut directions while principle strain values are able to rotate freely. The fixed strut directions are used to calculate the principle stresses in concrete rather than the principle strain directions. The applied strain field is transformed into these fixed strut directions and the calculated strain values are utilized to obtain the principle stresses in concrete through the uniaxial constitutive model for concrete. The compression softening and biaxial damage parameters are used to reduce the obtained stresses. The constitutive material model for reinforcing steel is applied along the orthogonal rebar directions and superposition of stresses developing in concrete and reinforcing steel gives the resultant average stresses on the panel element. In Figure 2.3, concrete behavior after the formation of the second crack in FSAM is illustrated.

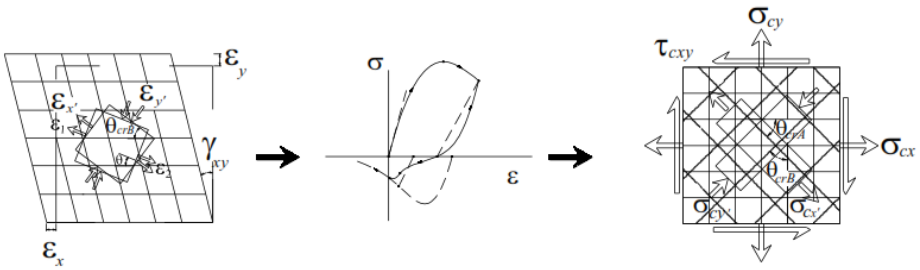

Figure 2.3. Behavior of Concrete after the Second Crack Formation in the FSAM (Orakcal *et al.*, 2012).

2.3. Constitutive Material Models

2.3.1. Constitutive Model for Reinforcement

In the constitutive panel model (FSAM), the behavior of reinforcing steel is represented by the well-known nonlinear hysteretic relationship of Menegotto and Pinto (1973), as extended by Filippou *et al.*, (1983) to incorporate isotropic strain hardening effects. Bauschinger's effect is also incorporated into the model through cyclic degradation of tangent stiffness in the unloading and reloading curves. A description of the constitutive model is shown in Figure 2.4. In the cyclic case, σ_r and ϵ_r are the stress and strain at the point of strain reversal, which also forms the origin of the asymptote with slope E_0, and parameters σ_0 and ϵ_0 form the stress and strain at the intersection point of two asymptotes.

In the model, the tension stiffening relationship proposed by Belarbi and Hsu (1994) is implemented. The uniaxial stress-strain relationship of bare reinforcing bar was replaced with an average stress-strain curve of defined for bars stiffened by concrete between cracks.

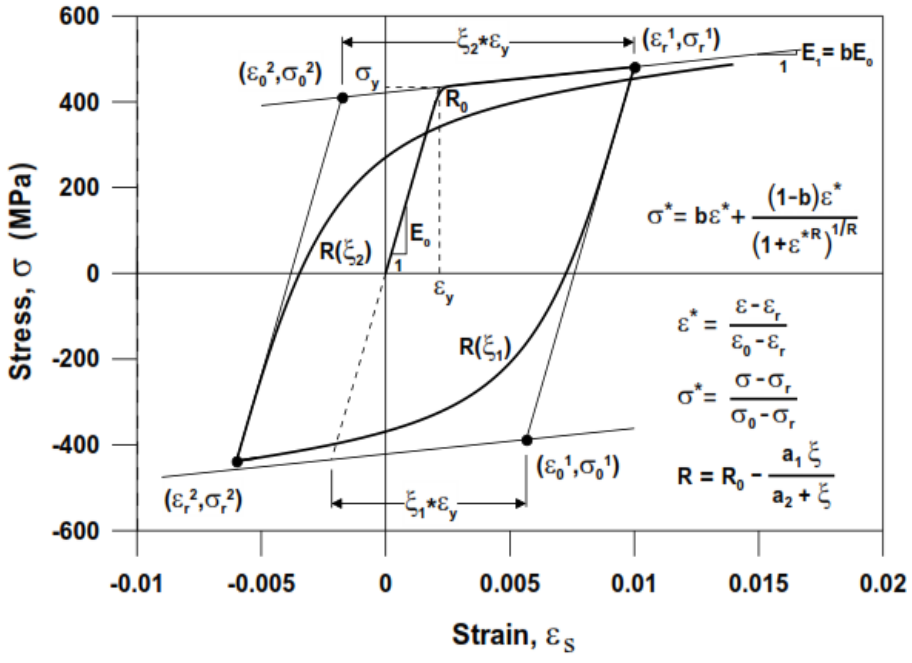

Figure 2.4. Constitutive Model for Reinforcing Steel (Menegotto and Pinto, 1973).

2.3.2. Constitutive Model for Concrete

The uniaxial hysteretic constitutive model proposed by Chang and Mander (1994) is implemented as stress-strain behavior for concrete (Figure 2.5). The Chang and Mander model has been shown to provide accurate representation of the experimental results presented by various researchers. The model is a rule-based, generalized, and non-dimensional model that can simulate the hysteretic behavior of both confined and unconfined concrete, under continuous compression and tension loading. Mander *et al.*, (1988) calibrated the model for unconfined and confined concrete in cyclic compression.

This constitutive model implemented for concrete was modified by adding compression softening (defined by Vechio and Collins, 1993), hysteretic biaxial damage (defined by Mansour *et al.*, 2002) and tension stiffening effects (defined by Belarbi and Hsu, 1994) into the formulation. The aim of these modifications was to simulate the behavioral features of concrete under biaxial loading conditions. The effects of these parameters are described in the following sections.

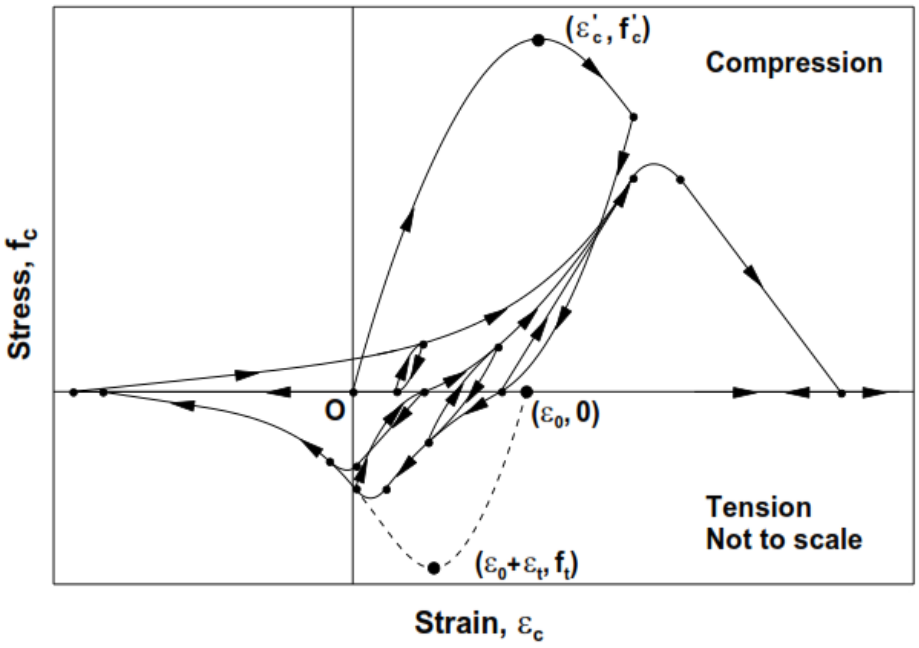

Figure 2.5. Constitutive Model for Concrete (Chang and Mander, 1994).

The compression softening effect on concrete, stemming from the tensile strains

perpendicular to crack directions, is typically simulated by reduction in the compressive stresses in concrete in the principal directions (Figure 2.6). The effects of the compression softening have been experimentally validated by many researchers (e.g., Vecchio and Collins, 1986). The compression softening relationship proposed by Vecchio and Collins (1993) was implemented into Fixed Strut Angle constitutive panel model formulation. Although more complicated models are available to represent compression softening effects, this relationship provides simplicity while achieving reasonably accurate predictions of experimentally-observed behavior.

In addition to above factors, the biaxial loading which affects the cyclic damage on concrete which is another considerable aspect in the modeling of an RC panel element. A damage coefficient is used to represent the cyclic damage on concrete. This coefficient differentiates from tension stiffening and compression softening parameters such that it is a cyclic-strain-history dependent parameter. Depending on the maximum value of the previously-applied compressive strain in the perpendicular direction, the biaxial damage effect physically reflects as softening in the compressive stress-strain behavior of concrete along one direction. Due to its dependence on previous loading steps, this behavior is not observed under monotonic loading. This coefficient is implemented in the model as a reducing multiplier to compressive stresses in the concrete as in the case of compressive softening. There are two models for the damage coefficient in the literature; Stevens (1987), Mansour and Hsu (2002). The biaxial damage formulation proposed by Mansour and Hsu (2002) was used in the formulation of constitutive Fixed Strut Angle Panel Model.

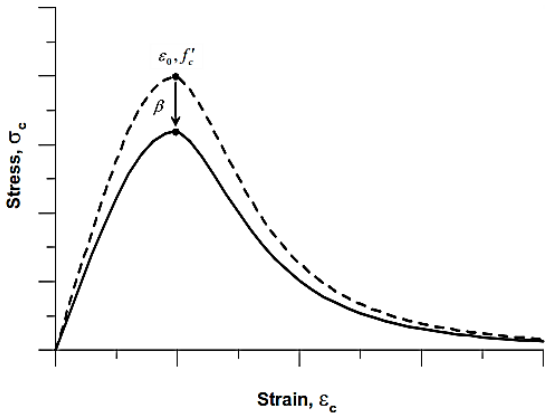

Figure 2.6. Compression Softening Effects Implemented in the Panel Model (Ulugtekin, 2010).

2.3.3. Constitutive Modeling of the Shear Aggregate Interlock Effect in Concrete

In the original formulation of the Fixed-Strut-Angle constitutive panel model developed by Ulugtekin (2010), the shear aggregate interlock effect along crack surfaces in concrete were neglected. To remedy this shortcoming of the original FSAM, the cyclic shear aggregate interlock model proposed by Orakcal *et al.*, (2012) starts with linear loading/unloading behavior, relating the sliding shear strain along a crack to the shear stress, via a simple linear elastic relationship between the sliding shear strain and the resultant shear stress along the crack surface. When the concrete normal stress perpendicular to the crack is tensile (crack open), the shear stress is restrained to zero value and when the concrete normal stress is compressive (crack closed), is bounded via the product of a friction coefficient and the concrete normal stress perpendicular to the crack. The linear unloading/reloading slope of the shear stress vs. sliding strain relationship was taken as a fraction of the concrete elastic modulus (a value $0.4E_c$ was adopted, representing the elastic shear modulus of concrete), and a value of 1.0 was assumed for the friction coefficient, which needs to be multiplied by the compressive stress in concrete in perpendicular direction to the crack, in order to obtain the shear stress capacity along the crack surface (Figure 2.7a). Under constant compressive stress in concrete perpendicular to the crack, this model yields an elasto-plastic aggregate

interlock behavior under cyclic loading, similar to the cyclic stress-strain behavior of reinforcing steel. Gullu and Orakcal (2014) also considered the clamping effect of reinforcing steel bars straddling the crack surface to the sliding shear stress (shear friction) capacity of the aggregate interlock model, similarly to the approach presented in ACI-318-11 (Figure 2.7b).

As mentioned in the paper by Kappos *et al.*, (2011), the mechanisms mobilized along interfaces due to slip and their interaction is a rather complex mechanical issue, especially under cyclic loading conditions where degradation should also be accounted for. In addition, Kappos *et al.*, (2011) recommends the shear aggregate interlock friction coefficient μ to be taken equal to a value of 0.44 regardless of whether the interlock affects are induced by compressive stresses in concrete or clamping effect on reinforcing bars. In this study, contribution of the clamping force created by the reinforcing steel bars to the shear friction capacity is represented by a friction coefficient of $\mu_s = 0.35$ and $\mu_s = 0.70$ for specimens tested at Boğaziçi University and at UCLA, respectively, based on preliminary analysis results obtained using the model. Contribution of the compressive stress in concrete perpendicular the crack surface is considered using a friction coefficient $\mu = 1$, based on sensitivity studies conducted using the model on previously-conducted tests on squat RC walls experiencing sliding shear failure (Orakcal *et al.*, 2009). In addition, while sliding shear stresses on the crack surface resulting from the compressive stress in concrete follows elasto-plastic hysteretic behavior (Figure 2.7a), those resulting from the clamping force of the reinforcing steel bars are assumed to follow an origin-oriented hysteretic behavior (Figure 2.7b).

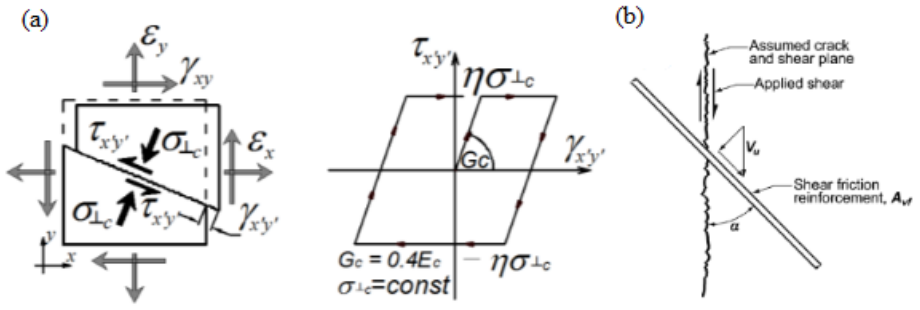

Figure 2.7. (a) Friction Based Constitutive Model for Shear Aggregate Interlock (Orakcal *et al.*, 2012), (b) Shear Friction Mechanism along a Crack in ACI-318.

2.3.4. Constitutive Modeling of Dowel Action on Reinforcing Bars

Accurate prediction of the nonlinear shear behavior of RC walls is a formidable task, even with the use of finite element modeling approaches, due to complexity of the shear transfer mechanism along cracks in concrete, and the lack of suitable models for the various actions that contribute to the shear transfer. A constitutive model representing dowel action on reinforcing bars was developed by He and Kwan (2001), for incorporation in finite element analysis of reinforced concrete structures. This constitutive dowel action model was implemented in the present study into the FSAM formulation, due to its relative simplicity. An overview of the dowel action model by He and Kwan (2001) is presented in this section.

In the dowel action model by He and Kwan (2001), the dowel effects on the reinforcing steel bars crossing cracks in concrete is represented in a smeared form in order to be compatible with the smeared crack model and smeared reinforcement model used in finite element analysis. A representative cracked concrete element containing a reinforcing steel bar crossing the crack perpendicularly is depicted in Figure 2.8.

When the concrete blocks at the two sides of the crack slide against each other, the reinforcing bar embedded inside the concrete is subjected to dowel displacement, which is defined as the relative transverse displacement of the two ends of the reinforcing bar. Due to the dowel deformation so caused, transverse shear force and contraflexural bending moment are developed in the reinforcing bar. However, only a certain length of the bar in the vicinity of the crack is subjected to significant dowel deformation. Denoting the length of the bar subjected to significant dowel deformation by l, the dowel displacement Δ may be calculated from the shear strain across the crack γ_{12} using Equation 2.1. The dowel force V_d developed in the bar varies with the dowel displacement Δ according to a certain dowel force displacement relationship. Using the secant stiffness formulation, the dowel force and the dowel displacement can be related by Equation 2.2 where K_d is the secant dowel stiffness of the reinforcement bar. The dowel force V_d acts against the concrete and may be smeared over the crack surface as a dowel stress acting across the crack. The dowel stress may be calculated

from the dowel force from Equation 2.3 in which ρ_s is the reinforcement ratio in the crack direction and A_s is the sectional area of the reinforcement. Equation 2.4 is derived by combining Equation 2.1 to Equation 2.3.

The case of a reinforcing bar crossing a crack at an acute angle is more complicated because apart from the shear strain, the tensile strain across the crack can also cause dowel displacement of the reinforcement bar. Consider the cracked concrete element containing a reinforcement bar running in the x-direction in Figure 2.9a and the cracked concrete element containing a reinforcement bar running in the y-direction in Figure 2.9b. The dowel displacements Δ_x of the bar running in the x-direction and Δ_y of the bar running in the y-direction are given in Equation 2.5 and Equation 2.6. In the present model formulation, dowel displacements Δ_x and Δ_y are defined as an equal values that are calculated by using the half of the shear strain acting on the panel element, γ_{xy}. The dowel forces are identified as V_{dx} and V_{dy} develop in the two reinforcing bars running in the x and y directions, respectively. The corresponding dowel stresses (τ_x, τ_y) developing in the reinforcing bars are expressed as Equation 2.7 and Equation 2.8. In this study, only the contribution of reinforcing bars running in y direction is considered and incorporated in the formulation of the FSAM.

$$\Delta = \ell \times \gamma_{12} \tag{2.1}$$

$$V_d = K_d \times \Delta \tag{2.2}$$

$$\tau_{12}^d = \frac{\rho_s}{A_s} \times V_d \tag{2.3}$$

$$\tau_{12}^d = \frac{\rho_s}{A_s} \times K_d \times \ell \times \gamma_{12} \tag{2.4}$$

$$\Delta_x = \ell_x(\varepsilon_1 cos\theta \sin\theta + \gamma_{12}\cos^2\theta) \tag{2.5}$$

$$\Delta_y = \ell_y(\varepsilon_1 cos\theta \sin\theta - \gamma_{12}\sin^2\theta) \tag{2.6}$$

$$\tau_x^d = \frac{\rho_x}{A_{sx}} \times V_{dx} \tag{2.7}$$

$$\tau_y^d = \frac{\rho_y}{A_{sy}} \times V_{dy} \tag{2.8}$$

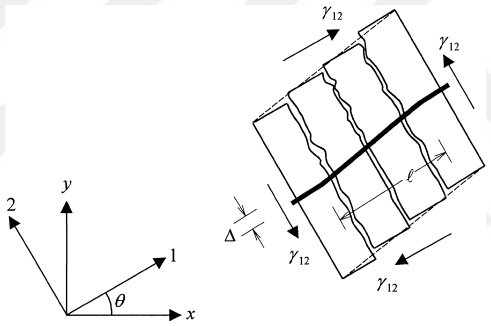

Figure 2.8. Dowel Action of a Reinforcement Bar Crossing a Crack (He and Kwan, 2001).

In this dowel action model, the dowel force at ultimate limit state Vdu is expressed as in Equation 2.1. In this equation, f_c represents the compressive strength of the concrete in MPa, d_b is the diameter of the bar in mm and f_y is the yield strength of reinforcing steel bar. This equation is based on experimental results conducted by Dulacska (1972). A similar empirical equation has also been proposed by Vintzeleou and Tassios (1987). Detailed information on derivation of this empirical equation is presented in the paper proposed by He and Kwan (2001).

$$V_{du} = 1.27 \times d_b^2 \times \sqrt{|f_c| \times |f_y|} \tag{2.9}$$

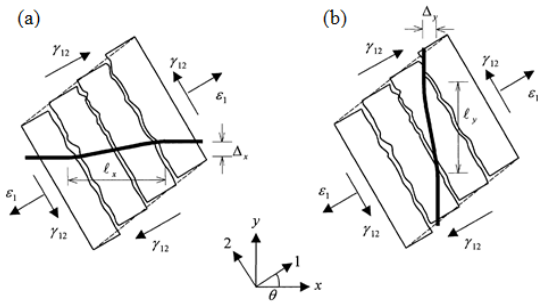

Figure 2.9. Cracked Concrete Elements Containing a Reinforcement Bar Running (a) in the x-direction and (b) in the y-direction Crossing the Cracks at Acute Angle (He and Kwan, 2001).

In the present study, the elasto-plastic dowel action model presented by He and Kwan (2001) is implemented as the monotonic envelope of the dowel force vs. shear strain constitutive relationship, and origin-oriented unloading and reloading paths previously adopted by Horoz (2015) are improved and used to represent hysteretic behavior.

2.3.5. Constitutive Modeling of Cyclic Degradation in Shear Aggregate Interlock and Dowel Action

Under loading and unloading reversals, the shear aggregate interlock and dowel mechanisms tend to degrade and this phenomenon is very common in squat structural walls. Kappos *et al.*, (2011) proposed Equation 2.10 and Equation 2.11 to incorporate cyclic degradation in terms of number of cycles, concrete strength, steel yield strength, and slip parameters.

$$\tau_{f,n} = \tau_{f,1} \times \tau_{deg} = \tau_{f,1} \left\{ 1 - \left[0.002\,(n-1) \left(\frac{f_c}{\sigma_N} \right) \left(\frac{|s_f|}{s_{f,u}} \right) \right]^{1/3} \right\} \tag{2.10}$$

$$F_{D,n} = F_{D,1} \times F_{deg} = F_{D,1} \left[1 - \frac{1}{7}\sqrt{n-1} \right] \tag{2.11}$$

In Equation 2.10 and Equation 2.11, coefficient n is the number of cycles after the capacity is reached, f_c and σ_N are the concrete strength and clamping stress, respectively. s_f and $s_{f,u}$ represent slip at current step and the maximum slip due to friction, respectively. $\tau_{f,1}$ and $F_{D,1}$ are the friction and dowel forces at each cycle, respectively, calculated at initial step. Figure 2.10 illustrates degradation with increasing cycles for both shear aggregate interlock and dowel mechanisms. Degradation of dowel force as the cyclic load path is updated is displayed in Figure 2.11. Details of the degradation parameters are presented in the paper proposed by Kappos *et al.*, (2011).

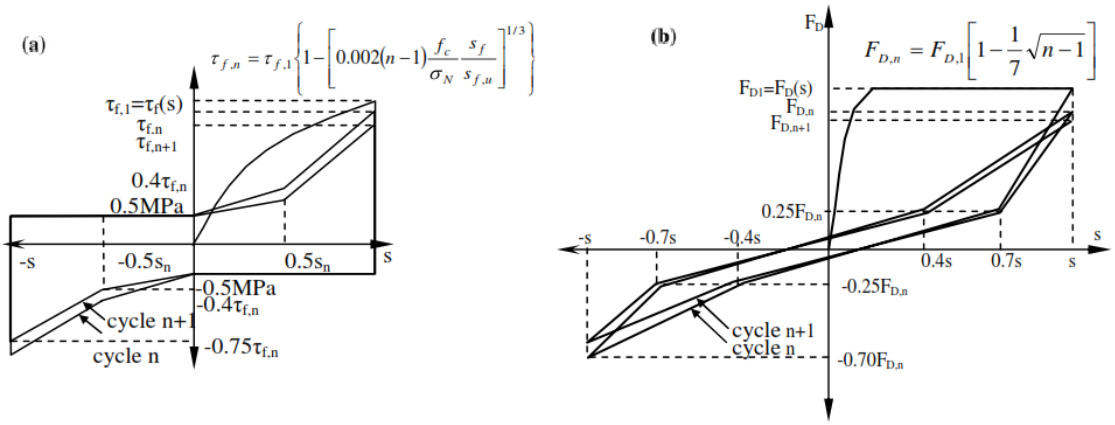

Figure 2.10. Response to Cyclic Loading, (a) Friction (b) Dowel (Kappos *et al.*, 2011).

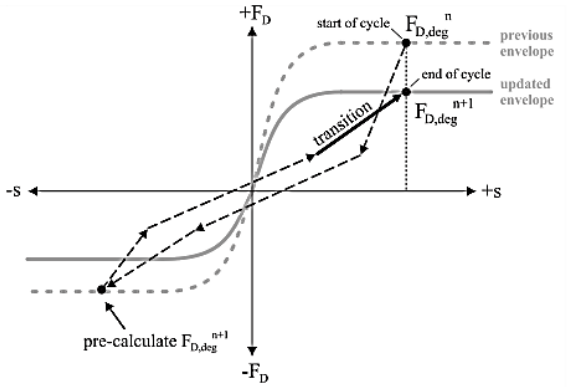

Figure 2.11. Calculation and Update of the Degradation Factor and Envelopes for Dowel Action (Kappos *et al.*, 2014).

Preliminary analysis results showed that consideration of degradation parameters significantly improved the model predictions for the squat walls investigated. The

degradation was implemented in the hysteresis loops beyond the elastic response region (i.e., after capacity is reached). For degradation of dowel action, the equation proposed by Kappos *et al.*, (2011) was implemented. For shear aggregate interlock, extensive calibration was conducted for contribution of the clamping force created by the reinforcing steel bars to the shear friction capacity. Through this calibration, the degradation was introduced in the model in terms of number of hysteresis loops only and no degradation was implemented for the contribution of concrete in the shear aggregate interlock. The representation of the origin-oriented hysteretic dowel action with cyclic strength degradation implemented in this study is illustrated in Figure 2.12.

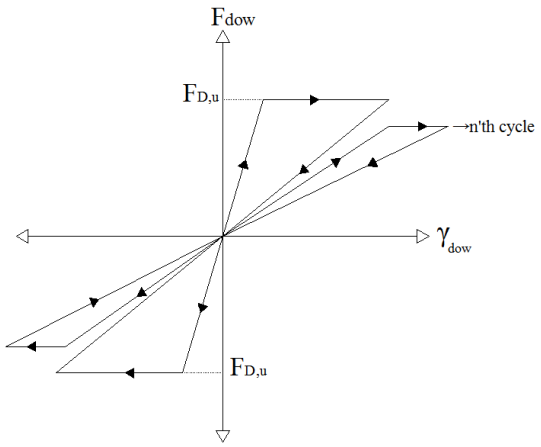

Figure 2.12. Origin-Oriented Model for Dowel Action.

2.3.6. Consideration of the Strain Penetration Effect

When a wall experiences large bending moments at the base, as in the case for early drift levels of the squat wall tests investigated in this study, large tensile stresses (and therefore strains) develop in the longitudinal reinforcement at the base of the wall. These strains gradually penetrate into foundation, which produces an accumulated elongation (commonly referred to extension/slip) on the reinforcement at the wall-foundation interface. The rotations stemming from the strain penetration effect introduce additional top displacement on the wall, which may be a significant portion of the total top displacement if the lateral stiffness of the wall is large (which is the case for a squat wall). When strain penetration is neglected, analytical models may overestimate the lateral stiffness of a RC member especially that of a squat wall

(Zhao and Sritharan, 2007).

To consider the effects of strain penetration on the response of the wall specimens investigated in this study, an initial moment curvature analysis was performed for each specimen. Yield moment and yield strain values were obtained from this analysis along with neutral axis depth of each specimen. With the assumption of a crack along the wall-foundation interface, the strains were integrated over the embedment length of reinforcing bars, which was close to the development length, in the specimen pedestals (foundations) to acquire the vertical elongation of the wall boundary reinforcement at the interface, associated with strain penetration. A linear distribution of strains within the pedestal was assumed in which strains are zero at a distance equal to the development length of the bar from the interface (Figure 2.13). The rotations were calculated as dividing the displacement by the neutral axis depth. The yield moment was then divided by yield rotation to obtain an elastic rotational spring stiffness.

Using the rotational spring stiffness, any force accompanied by an incremental displacement then was converted to moment at the top of the wall. Following the rotations obtained from the moments, the additional top displacement resulting from slip was calculated by multiplying the rotations with the height of the wall. Initial cycles were affected by the contribution of slip more significantly which altered the initial stiffness of the walls.

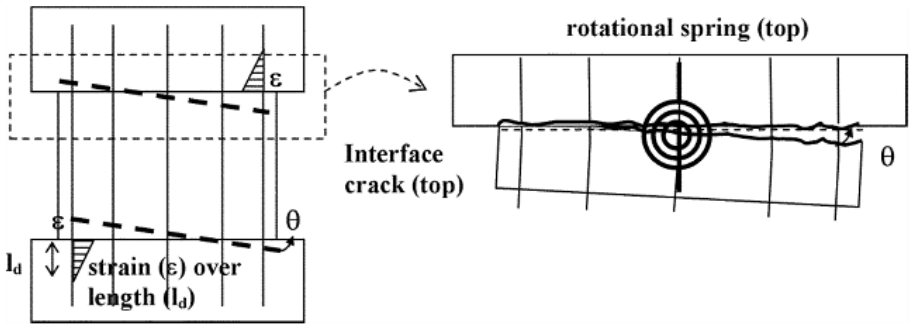

Figure 2.13. Strain Penetration Model (Massone *et al.*, 2009).

In this study, the calculated displacements due to the strain penetration and

elongation of the reinforcement were discarded from the test results and drift histories were implemented into model with lower displacement values, especially at early loading stages. The results, in accordance with the calculations, give higher stiffness for both analytical model and experimental outcomes due to this effect. As seen from Figure 2.14, for specimens tested under double curvature or single curvature, at early loading levels, neglecting strain penetration and additional displacement associated with it leads to the overestimation of initial stiffness. The discrepancy between two incidents tends to decrease at high drift levels and both models, with or without considering strain penetration effects, yield similar results.

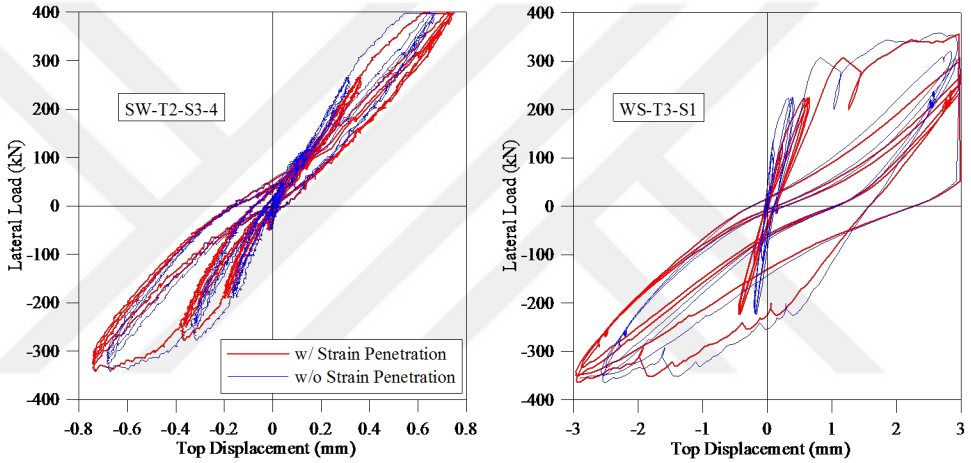

Figure 2.14. Effect of Strain Penetration.

2.4. Finite Element Modeling Methodology

In this section, the two-dimensional finite element modeling methodology is described. The methodology is used for assembling the constitutive panel elements described in the previous section into a wall model, as developed by Gullu (2013) for modeling of slender walls. In the following subsections, assembly of local stiffness matrices and the internal force vector of mesh elements (local elements) are described. Moreover, formulation of support conditions and constraints for modeling of walls are summarized and the nonlinear analysis solution strategy is outlined. Further details on the finite element model procedure are available in the M.S. Thesis by Gullu (2013).

2.4.1. 4 Nodes, 8 Degree of Freedom Rectangular Element

In the finite element modeling approach, rectangular two-dimensional membrane elements are adopted. The rectangular element is formulated as a membrane element in order to validate it for in-plane loading conditions. The rectangular membrane element has four nodes with two degrees of freedom (DOFs) in each node, in vertical and horizontal directions. No rotational DOFs are implemented in the model. Equilibrium equations are utilized at the four nodes of the rectangular element to calculate the known displacements along the DOFs. For the sake of simplicity, stress and strain values are only calculated at the center of each rectangular element corresponding to $\xi = \eta = 0$.

Each load step starts with the transformation of initial displacement values at each node of the wall model into nodal displacement values defined for each model element. Using a transformation matrix, the deformations of each element are calculated through known displacement values. This process is followed by the calculation of average strain values in each model element after which the tangent stiffness matrix is assembled for each element using the scheme depicted in Figure 2.15.

The next step is the generation of global tangent stiffness matrix for the structural wall model by obtaining the local stiffness matrices for the model elements. Each local stiffness matrix can be obtained using the tangent stiffness matrix and the geometric properties of each element. To perform this operation, as described in the definition of the FEM, the product of transpose of strain matrix $[\mathrm{G}]^T$, the elasticity matrix [E], and the strain matrix [G] is integrated. The volume integration shown in Equation 2.12 requires normalized coordinates $\xi = \frac{x}{w}, \eta = \frac{y}{h}$ not to be considered constant as they are dependent on x and y, respectively.

$$N_1 = \frac{1}{4}(1+\xi)(1+\eta) \tag{2.12}$$



Figure 2.15. Tangent Stiffness (Elasticity) Matrix Calculation Path.

After the calculation of the local stiffness matrix [k] of each model element, the assembly of these local stiffness matrices in modeling is constituted, which is described in the following section.

2.4.2. Finite Element Model Stiffness Assembly

For the assembly operation, the rectangular wall model is divided into model elements that are numbered as in advance. Next step is to superimpose the overlapping terms of the 8x8 local stiffness matrices with each other to generate the global stiffness matrix.

Local DOF numbers are displayed inside the model elements whereas global DOF numbers outside the elements (Figure 2.16). Global stiffness matrix of this sample model is calculated by superimposing the local stiffness terms at overlapping locations within the global stiffness matrix. Equation 2.13 is an example for calculation of one of the terms in the global stiffness matrix. Superscripts in Equation 2.13 indicate the model element numbers while subscripts indicate the local stiffness term index for each model element.

$$[K]_{99} = [k]^1_{11} + [k]^2_{33} + [k]^3_{22} + [k]^4_{44} \tag{2.13}$$

Same procedure is applied to calculate each term in the global stiffness matrix of the wall model as in Equation 2.13. As 18 global DOFs exist in this sample, the global stiffness matrix will be an 18x18 matrix, with 324 terms.

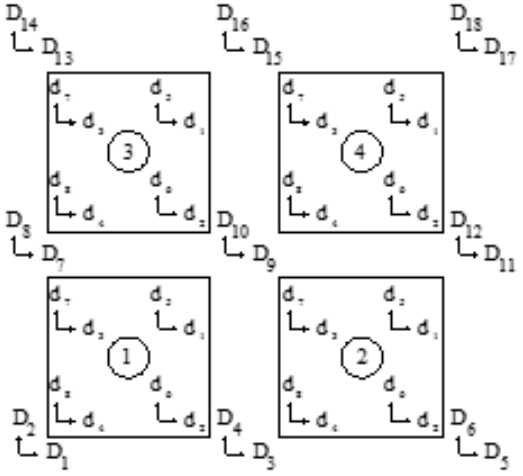

Figure 2.16. Global and Local DOFs for a Wall Model.

2.4.3. Internal Force Vector Assembly

This section provides information about how the assembly of the global internal force vector takes place using the local internal force vectors. Average strain values for each model element are utilized to calculate the average stress values for each model element using constitutive FSAM (Figure 2.17).

$$\begin{Bmatrix} \varepsilon_x \\ \varepsilon_y \\ \gamma_{xy} \end{Bmatrix} \rightarrow \text{Fixed Strut Angle Panel Model (FSAM)} \rightarrow \begin{Bmatrix} \sigma_x \\ \sigma_y \\ \tau_{xy} \end{Bmatrix}$$

Figure 2.17. Stress Vector Calculation Path.

Stress values are multiplied with thickness and half of vertical or horizontal width and superimposed to obtain the internal force vector for each element. Numbering of the internal force vector components, which is similar to the local displacement numbering scheme is illustrated in Figure 2.18.

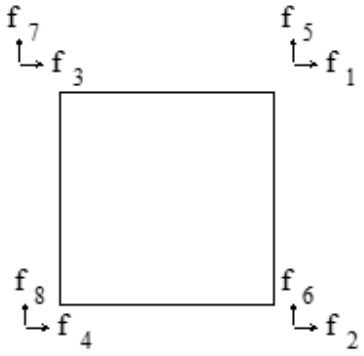

Figure 2.18. Numeration of Internal Forces for a Mesh.

The order of the terms in the global force vector for the wall model is defined by the global DOFs of the wall model. Local and global DOF numbers are displayed inside and outside the model elements respectively. Equation 2.14 is an example for calculation of one of the terms in the global internal force vector where superscripts indicate the model element numbers while subscripts illustrate the local internal force vector index for each model element.

$$\{F\}_{91} = \{f\}^{1}_{11} + \{f\}^{2}_{31} + \{f\}^{3}_{21} + \{f\}^{4}_{41} \tag{2.14}$$

Same procedure is applied to calculate each term in the global internal force vector as in Equation 2.14.

2.4.4. Support Conditions and Constraints

Displacement values are assigned as zero at the supports of a wall. This condition depicts zero displacement along the DOFs of the model at the supports. The reaction forces at the supports are calculated from the equilibrium equation, using the known (zero) displacement values along the DOFs at the supports.

Moreover, to simulate the test conditions, constraint conditions along selected DOFs have to be implemented to validate the wall model experimentally. The wall specimens used for experimental validation of the model were cast monolithically with

stiff RC load-transfer-beams, which behaved like rigid bodies during testing. Therefore, a body constraint was defined along the top DOFs of the FEM of the wall (Figure 2.19).

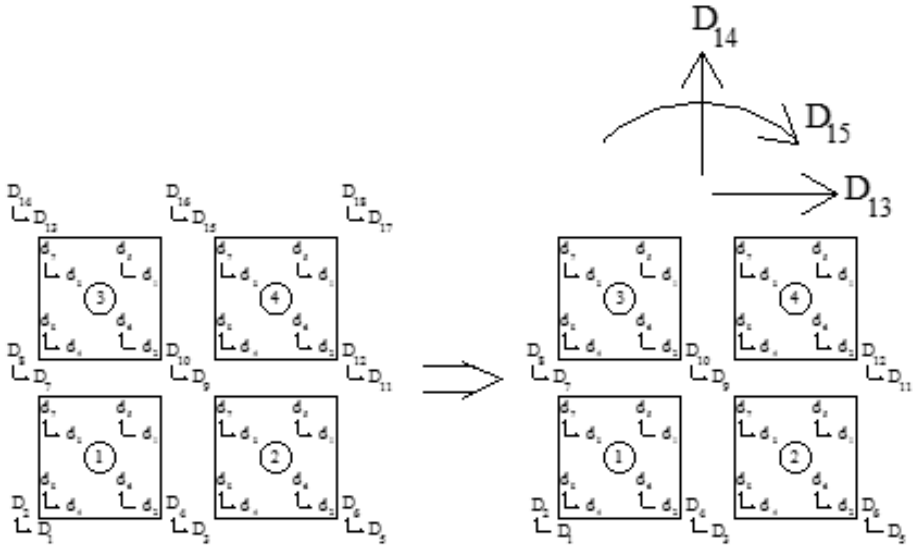

Figure 2.19. Conversion of DOFs after the Assignment of Body Constraint (Gullu, 2013).

The body constraint in the model represent the rigid load-transfer-beams located at the top of RC wall specimens. A displacement transformation matrix [T] is used to implement body constraint in the model formulation. The body constraint condition enforces equal horizontal displacement in the horizontal direction while relating vertical displacements to a global rotational displacement at the top of the wall through the plane-sections-remain-plane condition. The transformation matrix, [T], is a matrix that transforms an 18x18 stiffness matrix to a 15x15 stiffness matrix.

2.4.5. Nonlinear Analysis Solution Strategy

As described in the previous sections, through integration and stiffness assembly of the model elements, the global stiffness matrix and the internal force vector for the wall model were derived. Moreover, support conditions and constraints were implemented in the model formulation. Then, a displacement-controlled nonlinear analysis solution strategy (Clarke and Hancock, 1990; Simons and Powell, 1982) was adopted for conducting displacement-controlled hysteretic lateral load analysis of RC walls so

that model results could be correlated with results of drift-controlled lateral load tests conducted on wall specimens.

Two main stages constitute the applied strategy which are load incrementation and equilibrium stages. The increment stage (denoted by "*i*") includes the incrementation of the target displacements imposed on the model, whereas during the equilibrium stage (denoted by "*j*"), iterations are performed on the model displacements, in order to reach equilibrium. The load incrementation stage includes the incrementation of the target displacements imposed on the model, whereas during the equilibrium stage, iterations are performed on the model displacements, in order to reach equilibrium between the internal and external forces, within a specified tolerance. The adopted nonlinear analysis solution strategy, details of which are presented by Gullu (2013), is graphically illustrated in Figure 2.20 and Figure 2.21.

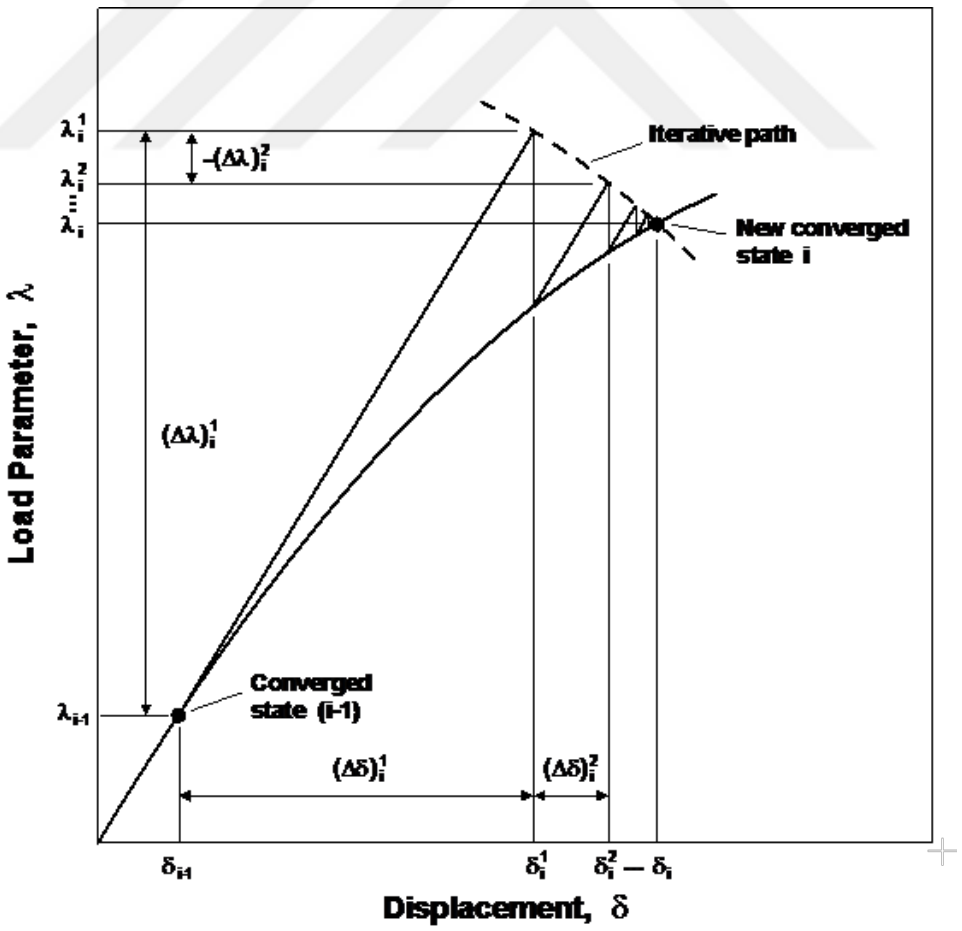

Figure 2.20. Representation of the Nonlinear Analysis Solution Strategy for a Single Degree of Freedom System (Clarke and Hancock, 1990).

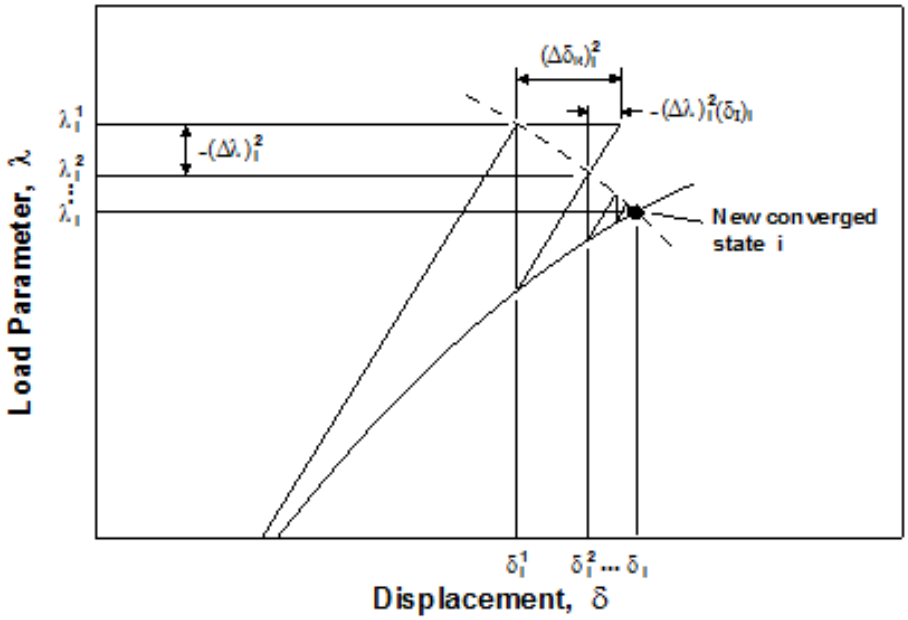

Figure 2.21. Iterative Strategy and Residual Displacements (Clarke and Hancock, 1990).

3. EXPERIMENTAL CALIBRATION OF THE MODEL

The finite element model formulation, together with the constitutive material and behavioral models described in the previous Chapter, were implemented in Matlab for conducting nonlinear analysis to simulate the hysteretic lateral load behavior of squat wall specimens. The calibrated and analytically compared tests include eleven squat wall specimens tested by Terzioglu (2011) at Boğaziçi University Structural Engineering Laboratory, ten squat wall specimens tested by Massone (2006) at University of California Los Angeles, and four squat wall specimens tested by Orakcal *et al.*, (2009) at University of California Los Angeles. This chapter provides a description of the experimental program and presents information on experimental calibration of the wall model to represent the characteristics of wall specimens and the loading conditions.

3.1. Description of the Wall Specimens

In this study, fifteen specimens were selected to validate the proposed analytical model. In the subsequent sections, description of the wall specimens tested at University of California Los Angeles and Boğaziçi University is illustrated. The selected wall specimens all had relatively low aspect ratio and were expected to experience shear-controlled responses. Detailed information about the tests conducted can be found in Ph.D. Thesis by Massone (2006), the paper by Orakcal *et al.*, (2009), and in M.S. Thesis by Terzioglu (2011).

3.1.1. Wall Specimens Tested at University of California Los Angeles

Tests conducted at UCLA were spandrel and pier walls representative of wall segments in existing perforated perimeter wall buildings (from 1940 to 1970) in California. The walls were 3/4-scale, spandrel walls included weakened plane joints (reduced concrete cross-section and cut longitudinal bars as crack initiator) while pier walls had straight steel transverse (not hooked) reinforcement. Two types of spandrel walls were tested by Massone (2006) and differentiated by boundary reinforcement ratio while

three types of pier walls tested by Massone (2006) were differentiated by the amount of axial load. Two types of spandrel walls were tested by Orakcal *et al.*, (2009) and differentiated by concrete strength and loading history. For every type, two wall specimens were tested. The specimens having the same aspect ratio, same horizontal and vertical web reinforcement ratios, same boundary reinforcement ratio and location of the weakened joint plate, if present, were considered as being of the same type. If any of these properties would change, the type of the specimen would change. The naming scheme used for the wall specimens is shown in Figure 3.1.

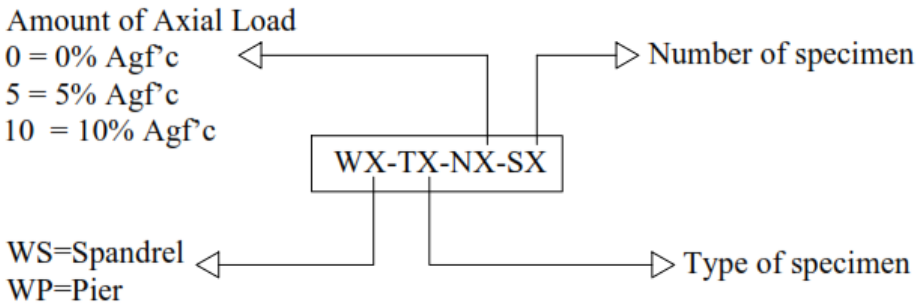

Figure 3.1. Specimen Name Description for Tests Conducted at UCLA.

A summary of the geometric and reinforcement properties of the wall specimens are provided in Table 3.1. The steel reinforcement ratios were calculated as the total steel area divided by the tributary area of concrete. For the boundary reinforcement, the tributary area was defined as the full thickness of the wall multiplied by the length of the boundary region, defined as the center-to-center distance between the boundary reinforcing bars plus two clear covers (one per side). In Table 3.1, l_w is length of the wall, h_w is height of the wall, ρ_t is transverse reinforcement ratio, ρ_l is transverse reinforcement ratio, and ρ_b is boundary reinforcement ratio. The thickness for all specimens was 15.2 cm.

Table 3.1. Test Specimen Details for Tests Conducted at UCLA.

Specimen	I_w (cm)	h_w (cm)	Horizontal		Vertical		Boundary	
			Reinf. Bars	ρ_t (%)	Reinf. Bars	ρ_l (%)	Reinf. Bars	ρ_b (%)
WS-T1-S1	152	152	ϕ13@33 cm	0.278	ϕ13@23 cm	0.428	4ϕ16	3.12
WS-T1-S2	152	152	ϕ13@33 cm	0.278	ϕ13@23 cm	0.428	4ϕ16	3.12
WS-T2-S1	152	152	ϕ13@33 cm	0.278	ϕ13@23 cm	0.4	1ϕ13 +1ϕ16	1.7
WS-T2-S2	152	152	ϕ13@33 cm	0.278	ϕ13@23 cm	0.4	1ϕ13 +1ϕ16	1.7
WS-T3-S1	152	152	ϕ13@28 cm	0.278	ϕ13@28 cm	0.256	2ϕ13	1.33
WS-T3-S2	152	152	ϕ13@28 cm	0.278	ϕ13@28 cm	0.256	2ϕ13	1.33
WS-T4-S1	152	152	ϕ13@28 cm	0.278	ϕ13@28 cm	0.256	2ϕ13	1.33
WS-T4-S2	152	152	ϕ13@28 cm	0.278	ϕ13@28 cm	0.256	2ϕ13	1.33
WP-T5-N0-S1	137	122	ϕ13@30.5 cm	0.278	ϕ13@33 cm	0.227	2ϕ13	1.33
WP-T5-N0-S2	137	122	ϕ13@30.5 cm	0.278	ϕ13@33 cm	0.227	2ϕ13	1.33
WP-T5-N5-S1	137	122	ϕ13@30.5 cm	0.278	ϕ13@33 cm	0.227	2ϕ13	1.33
WP-T5-N5-S2	137	122	ϕ13@30.5 cm	0.278	ϕ13@33 cm	0.227	2ϕ13	1.33
WP-T5-N10-S1	137	122	ϕ13@30.5 cm	0.278	ϕ13@33 cm	0.227	2ϕ13	1.33
WP-T5-N10-S2	137	122	ϕ13@30.5 cm	0.278	ϕ13@33 cm	0.227	2ϕ13	1.33

Both spandrel and pier specimens were secured to a loading frame and strong floor by means of reinforced concrete pedestals at the top and bottom. The top and bottom pedestals of the specimens were designed to resist shear forces and bending moments generated by applied lateral loads. The weakened plane joints were attained by reducing concrete cross section through introducing wood edges in the specimens form and by reducing the effective longitudinal distributed steel reinforcement by cutting four out of six bars (Figure 3.2). The wood wedges were placed along the whole length of the specimen.

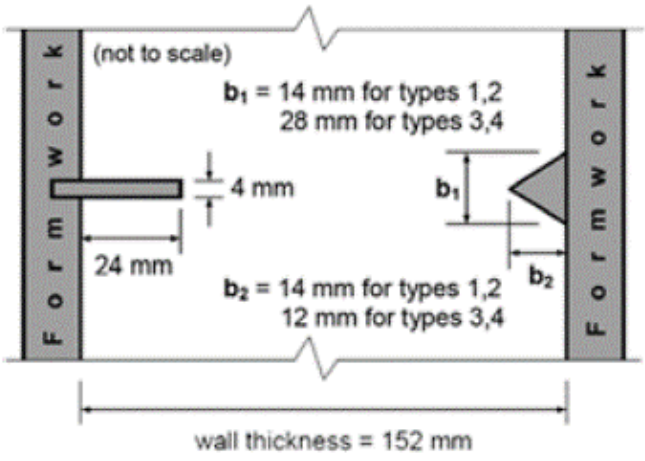

Figure 3.2. Weakened Plate Joint on Wall Spandrels (Massone *et al.*, 2009).

Spandrel specimens were 152 cm in tall, 152 cm in long and 15.2 cm in thick. The

geometry and distribution of reinforcing steel of wall section are displayed in Figure 3.3. Distributed vertical and horizontal reinforcement were placed in one curtain only. For Type 1 and 2 spandrels, the vertical distributed reinforcement was ϕ13@23 cm while the horizontal distributed reinforcement was ϕ13@33 cm. For Type 3 and 4 spandrels, both the vertical and horizontal distributed reinforcement were ϕ13@28 cm. As boundary reinforcement, 4ϕ16 were used for Type 1 walls, 1ϕ16 + 1ϕ13 were used for Type 2 walls, and 2ϕ13 were used for Type 3 and Type 4 walls. At boundaries, the horizontal bars were terminated with a 180° hook. The boundary bars were not cut at the weakened plate joint.

Wall pier specimens were 122 cm in tall, 137 cm in long and 15.2 cm in thick. The geometry and distribution of reinforcing steel of the wall specimen are shown in Figure 3.4. Distributed vertical and horizontal reinforcement were placed in one curtain only. The vertical distributed reinforcement was ϕ13@30.5 cm while the horizontal distributed reinforcement was ϕ13@33 cm. As boundary reinforcement, 2ϕ13 were used for all piers. The horizontal bars did not incorporate hooks at the ends. Some of the wall pier specimens were also subjected to axial loads; the axial load levels applied on the wall piers corresponded to 0%, 5%, and 10% of their axial compression capacity.

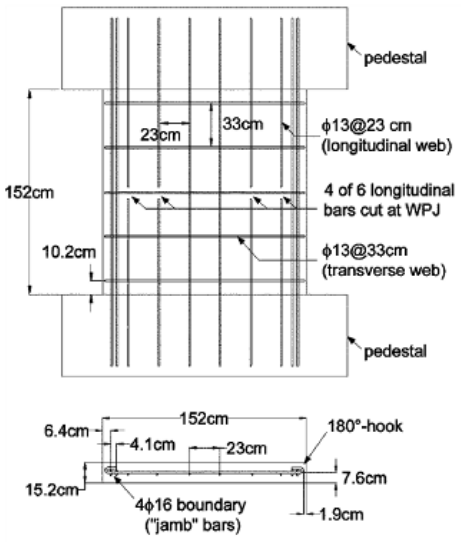

Figure 3.3. Wall Spandrel Geometry and Reinforcement (Massone *et al.*, 2009).

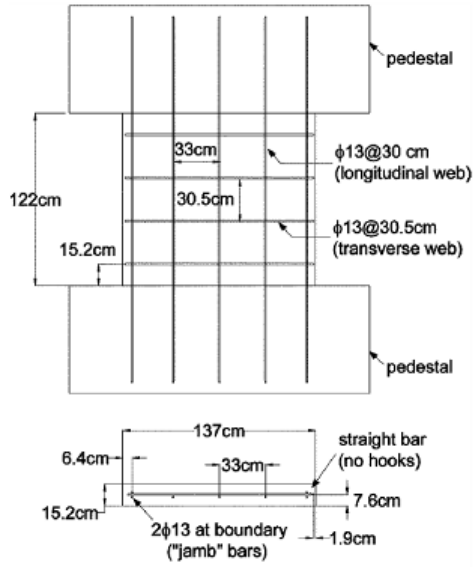

Figure 3.4. Geometry and Steel Reinforcement for Wall Piers (Massone *et al.*, 2009).

3.1.2. Wall Specimens Tested at Boğaziçi University

Wall tests conducted at Boğaziçi University included eleven squat wall specimens with low aspect ratio. Three sets of specimens were tested. The first set of specimens included three squat walls with aspect ratios of 0.5. The second set consisted of four structural walls, one having 0.33 aspect ratio, one having 1.0 aspect ratio and two having 0.5 aspect ratio. The third set included one 1.0 aspect ratio specimen and three 0.5 aspect ratio specimens. Two of the specimens were tested under different level constant axial loads. The specimens having the same aspect ratio, reinforcement ratio, and testing sequence were considered as being of the same type. If any of these properties changed, the type of the specimen would change. The naming scheme used for the wall specimens is shown in Figure 3.5.

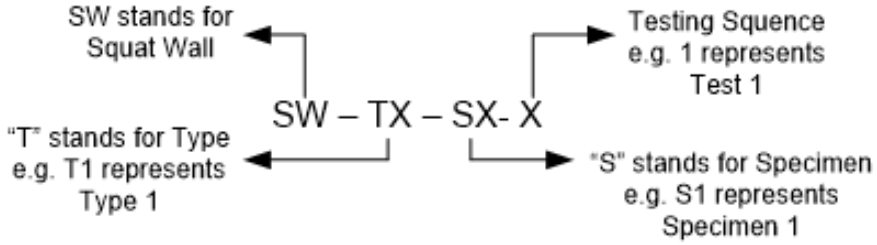

Figure 3.5. Specimen Name Description for Tests Conducted at Boğaziçi University.

A summary of the geometric and reinforcement characteristics of the walls is provided in Table 3.2. Reinforcement ratios were calculated as the total steel area divided by the tributary area of concrete. For the boundary reinforcement, the tributary area was defined as the full thickness of the wall multiplied by the length of the boundary region, defined as the center-to-center distance between the boundary reinforcing bars plus two clear covers (one per side). In Table 3.2, l_w is length of the wall, h_w is height of the wall, ρ_t is transverse reinforcement ratio, ρ_l is transverse reinforcement ratio, and ρ_b is boundary reinforcement ratio. The thickness for all specimens was 12 cm. The specimen SW-T2-S1-1 and the specimen SW-T2-S2-3 differed only in terms of their horizontal reinforcement anchorage conditions. Specimen SW-T2-S1-1 had U-cap hooks at the ends of the horizontal reinforcement bars, for anchorage. On the other hand specimen SW-T2-S2-3, as well as all other specimens, had 180° hooks on the horizontal bars. Figure 3.6 shows the details of the hooks used. Another variation existed in the Type1 specimens. The longitudinal boundary reinforcement of specimen Type1-S2 was confined with ties, whereas no confinement was provided for specimen Type1-S1, in order to observe the difference between these two specimens in terms of strength and ductility.

Table 3.2. Test Specimen Details for Tests Conducted at Boğaziçi University.

Specimen	I_w (cm)	h_w (cm)	Horizontal		Vertical		Boundary	
			Reinf. Bars	ρ_t (%)	Reinf. Bars	ρ_l (%)	Reinf. Bars	ρ_b (%)
SW-T2-S1-1	150	75	ϕ8@12.5 cm	0.68	ϕ8@12.5 cm	0.68	4ϕ16	5.15
SW-T1-S1-2	150	75	ϕ8@12.5 cm	0.34	ϕ8@25 cm	0.34	4ϕ16	5.15
SW-T2-S2-3	150	75	ϕ8@12.5 cm	0.68	ϕ8@12.5 cm	0.68	4ϕ16	5.15
SW-T2-S3-4	150	75	ϕ8@12.5 cm	0.68	ϕ8@12.5 cm	0.68	4ϕ16	5.15
SW-T3-S1-5	150	75	ϕ8@12.5 cm	0.68	ϕ8@12.5 cm	0.68	2ϕ8	0.65
SW-T4-S1-6	150	50	ϕ8@12.5 cm	0.68	ϕ8@12.5 cm	0.68	4ϕ14	3.95
SW-T5-S1-7	150	150	ϕ8@12.5 cm	0.68	ϕ8@25 cm	0.34	4ϕ22	9.75
SW-T6-S1-8	150	150	ϕ8@25 cm	0.34	ϕ8@25 cm	0.68	4ϕ22	9.75
SW-T1-S2-9	150	75	ϕ8@25 cm	0.34	ϕ8@25 cm	0.34	4ϕ16	5.15
SW-T1-N5-S1-10	150	75	ϕ8@25 cm	0.34	ϕ8@25 cm	0.34	4ϕ16	5.15
SW-T1-N10-S1-11	150	75	ϕ8@25 cm	0.34	ϕ8@25 cm	0.34	4ϕ16	5.15

The specimens were connected to the strong floor by means of a bottom pedestal. The top pedestal (load transfer beam) was connected to the horizontal actuator. The beam and pedestal of the specimens were designed to resist shear forces and bending moments generated by applied lateral loads. The bottom pedestal had dimensions of 1.0 m width and 2.1 m length. The dimensions of the bottom pedestal were also

designed to create enough frictional area so that the specimen does not slide under high lateral loads.

For the specimens, clear cover was 40 mm and the distance between boundary bars along the length was 50 mm. Hence, the boundary tributary area width corresponded to 130 mm. Specimens with three different aspect-ratio were constructed. There were a total of eight 0.5 aspect ratio wall specimens, one 0.33 aspect ratio wall specimen, and two 1.0 aspect ratio wall specimens.

The specimens with 0.5 aspect ratio had length of 1500 mm, height of 750 mm and thickness of 120 mm. They differed by their web reinforcement ratio or boundary reinforcement amount. Four of the Type-1 specimens had same transverse (horizontal) and vertical (longitudinal) web reinforcement ratios of $\rho_t = \rho_l = 0.34\%$. To differentiate, two of these Type-1 specimens were tested under different axial load levels. These two specimens were named as SW-T1-N5-S1-10 and SW-T1-N10-S1-11. The abbreviations N5 and N10 represent the axial load level applied (e.g. N5 refers to 5% of wall axial load capacity). Another Type-1 specimen was Type1-S2, which had confined boundaries at the ends. This specimen was constructed in order to see the effect of confined boundaries on the behavior. Specimen type T2-S1, which had horizontal (transverse) and vertical longitudinal web reinforcement ratios of $\rho_t = \rho_l = 0.68\%$ and U-caps at the end of the horizontal reinforcing bars. The parameters used for the construction of the third Type 2 specimen (T2-S3) were the same as the T2-S2 specimens. All the parameters were kept identical. The only parameter that differentiated these specimens was the concrete compressive strength, which was higher for the T2-S3 specimen, due to time of testing after concrete was poured. Details of specimen T1-S1 is illustrated in Figure 3.6.

Uniformly distributed vertical and horizontal web reinforcement of $\phi 8$ reinforcing steel bars were used in the wall specimens. Vertical reinforcement was placed uniformly along the wall section. Since there was enough space for development length in top and bottom pedestals, vertical reinforcing bars were not hooked at the ends. For all specimens, the distance between the two curtains of vertical web reinforcement was 62

mm. The horizontal web reinforcement was distributed along the height of the wall with equal spacing. The horizontal web bars were anchored with 180° hooks at the ends. Only for the T2-S1 specimen, horizontal reinforcing bars were terminated at the edges without hooks, and U-cap reinforcing bars were used for anchorage.

The longitudinal boundary bars were placed at both edges of the wall, inside the hooks of the horizontal bars. However, the boundary regions were not confined with ties, except for specimen T1-S2. Two different types of boundary reinforcement were used for the 0.5 aspect ratio structural walls. Seven of the structural walls had $4\phi16$ reinforcing bars at their boundaries. T3-S1, which had similar web reinforcement with Type 2 walls, had $2\phi8$ boundary reinforcement at both edges. The flexural yielding of the boundary reinforcement was targeted in design of specimen T3-S1.

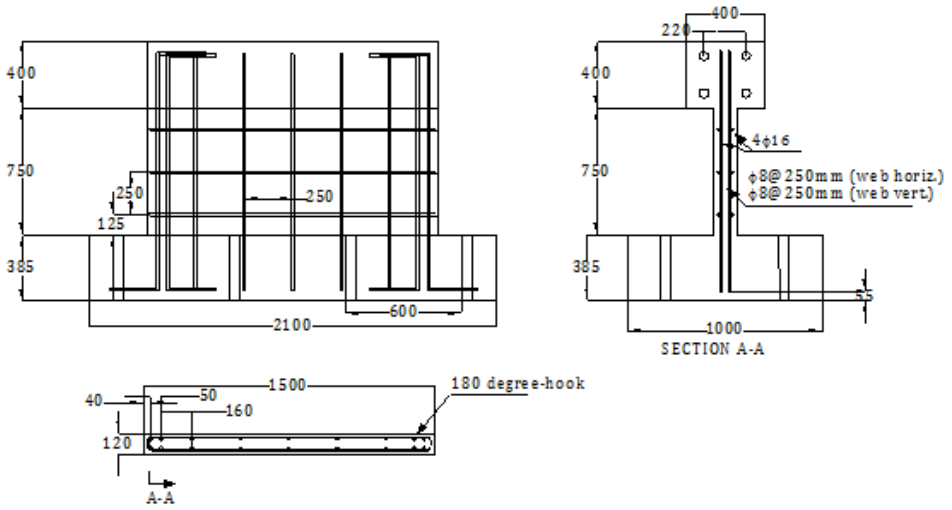

Figure 3.6. Geometry and Wall Reinforcement of Specimen T1-S1 (Terzioglu, 2011).

The specimen having a 0.33 aspect ratio was 1500 mm long, 500 mm tall and 120 mm thick. It had web reinforcement ratios of $\rho_t = \rho_l = 0.68\%$. The geometry and reinforcement details of specimen T4-S1 were displayed in Figure 3.7. The longitudinal boundary bars were placed at both edges of the wall. They were placed inside the hooks of the horizontal web bars. The boundary regions were not confined with ties. For this specimen, $4\phi14$ boundary bars were provided at both ends of the wall. The amounts of boundary bars provided targeted simultaneous reaching of flexural and shear capacities

of the wall.

Two structural walls having 1.0 aspect ratio were constructed, The Type 5 and Type 6, with identical horizontal web reinforcement amounts. Both of the walls had 0.68% horizontal reinforcement ratios, whereas the Type 5 specimen had 0.34% vertical web reinforcement ratio, and the Type 6 specimen has 0.68% vertical web reinforcement ratio. Figure 3.8 shows the geometry and reinforcement details of specimen T5-S1.

The height of the wall specimens was 1500 mm, the length was 1500 mm, and the thickness was 120 mm. For specimen T5-S1, $\phi 8$ vertical bars were placed with 250 mm spacing, and for specimen T6-S1, they were placed with 125 mm spacing. The vertical bars did not incorporate hooks at the ends, since there was enough embedment length in the top and bottom pedestals for the bars to develop. $\phi 8$ horizontal web bars were distributed along the height, with 125 mm spacing and terminated at the edges of the wall with 180° hooks.

The boundary reinforcement was placed inside the horizontal bars at both edges. Boundary regions were not confined with ties. $4\phi 22$ bars were used at both edges as boundary reinforcement. The boundary bars were anchored with 90° hooks inside the top and bottom pedestals.

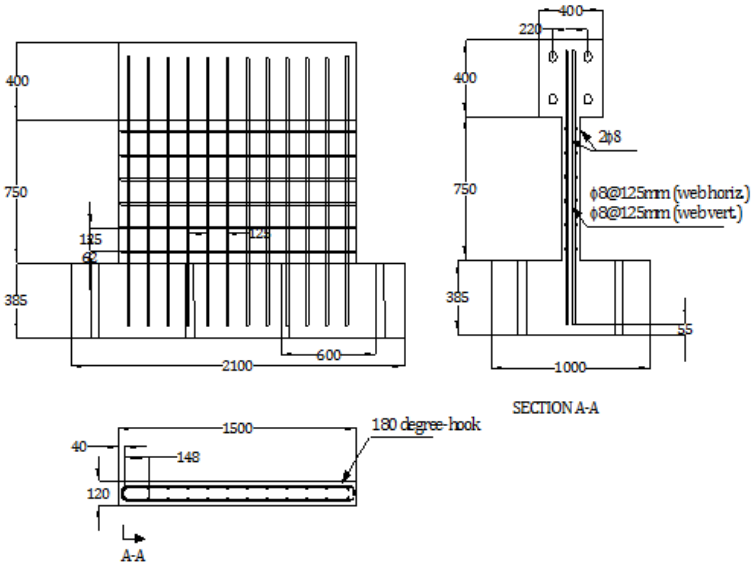

Figure 3.7. Geometry and Wall Reinforcement of Specimen T3-S1 (Terzioglu, 2011).

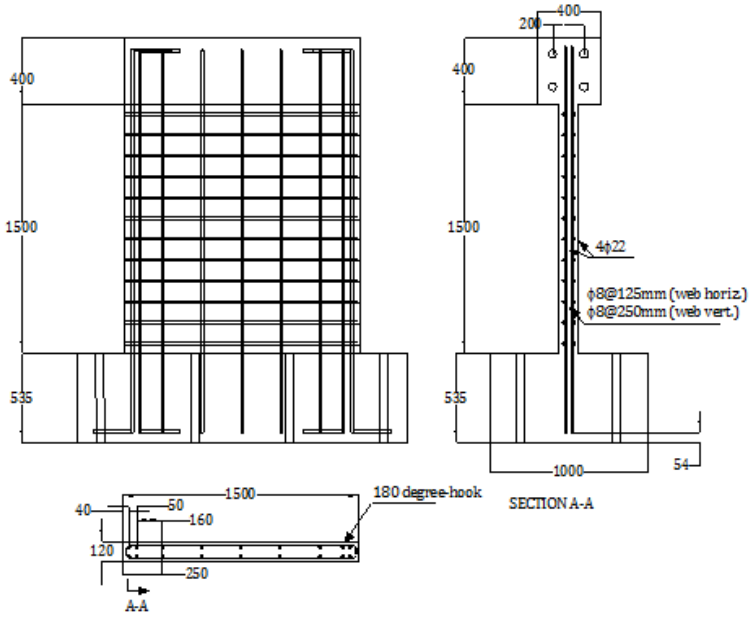

Figure 3.8. Geometry and Wall Reinforcement of Specimen T5-S1 (Terzioglu, 2011).

3.2. Test Setup

The UCLA specimens were tested in upright position. The general view of the setup is shown in Figure 3.9. The specimens were designed to be tested under a zero rotation at both ends (beam and pedestal), providing a constant axial load and a variable cyclic lateral load applied at mid-height of the specimens, creating a double-curvature loading condition, where the bending moment on each wall is zero at wall midheight and maximum (with reverse signs) at the top and bottom cross-sections of the wall, representing the actual loading conditions on wall piers and spandrels in a perforated perimeter wall of a building. Two, vertically placed, 1780 kN hydraulic actuators were used to apply the constant axial load and to prevent the top of the wall from rotating. A horizontally placed 890 kN hydraulic actuator was used to apply the lateral load. An out-of-plane frame was used to prevent twisting of each wall.

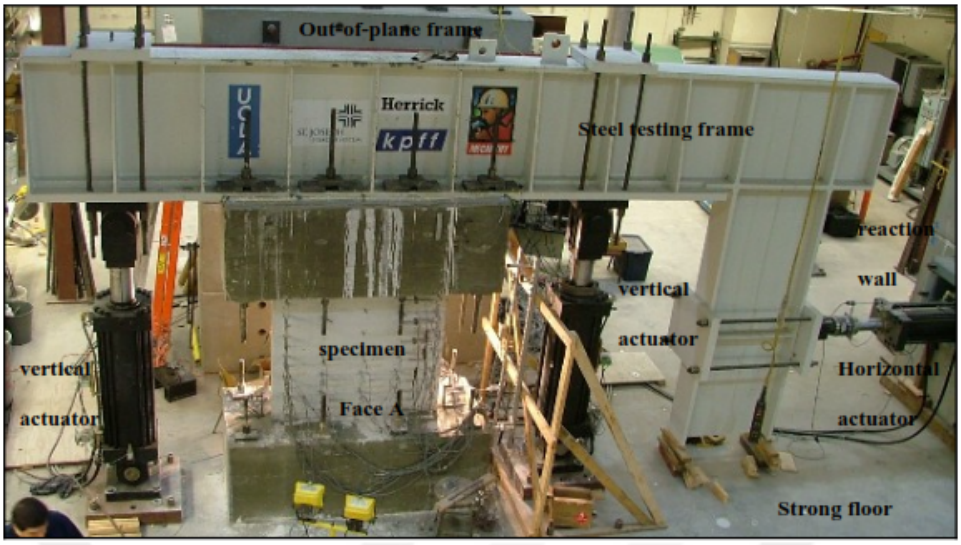

Figure 3.9. Test Setup (Massone, 2006).

Using the horizontal actuators, force-controlled cycles were performed followed by displacement-controlled cycles. Two levels of force-controlled cycles were applied. For two tests, the levels were 66.7 kN and 133.4 kN, whereas for the remainder, the levels were 111.2 kN and 222.4 kN. Three full cycles (push and pull) for each force level were applied. The forces were applied at rates from4.448 kN/s to 8.896 kN/s. This procedure was followed by three complete cycles (push and pull) of the following drift levels: 0.2%, 0.3%, 0.4%, 0.6%, 0.8%, 1.2%, 1.6%, 2.0%, 2.4%, and 3.2%. The displacements were applied at rates from 0.0127 cm/s to 0.0762 cm/s. The applied process is described in Figure 3.10.

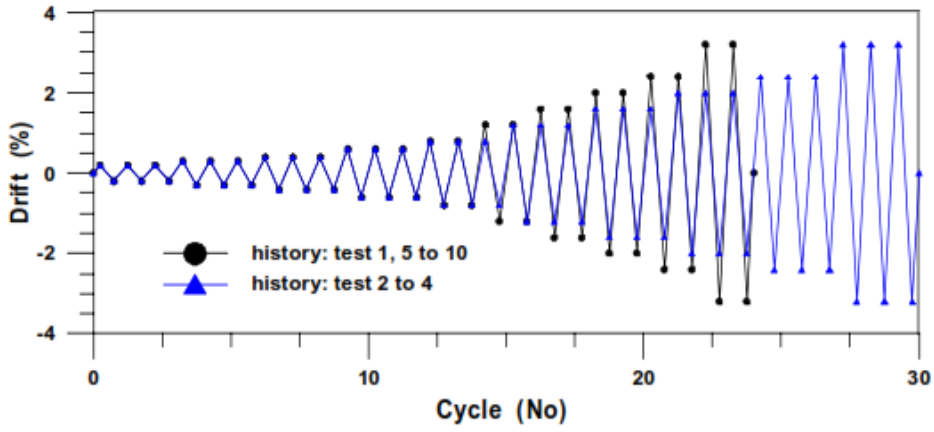

Figure 3.10. Displacement History (Massone, 2006).

The first set of wall specimens tested at Boğaziçi University included specimens T1-S1and T2-S1 and T2-S2. The second group consisted of specimens T2-S3, T3-S1, T4-S1, and T5-S1. Remaining four specimens constituted the third group, three of which were identical to Type1 specimen, and were tested under axial load. Lateral load on the specimens was applied using an actuator with a capacity of 1000 kN. One end of the actuator was fixed to a steel reaction wall. Figure 3.11 shows a photo of the test setup. Two specimens were tested under 5% A_{gfc} and 10% A_{gfc} axial load levels. The axial load was applied using four pre-stressed steel cables each having 250 kN axial tension capacities. The axial load was applied through a hydraulic cylinder placed between the steel beams and the top pedestal (load transfer beam) of each specimen. An out-of-plane frame was designed to prevent twisting of the wall specimens.



Figure 3.11. Test Setup (Terzioglu, 2011).

Reversed cyclic lateral loading was applied at the top of each specimen, resulting in a single curvature (cantilever) loading condition. Three full cycles were applied at each drift level of 0.05%, 0.1%, 0.15%, 0.2%, 0.3%, 0.4%, 0.6%, 0.8%, 1.0%, 1.2%, 1.4%, 1.6%, 1.8%, 2.0%, 2.4%, and 3.2%. Depending on their residual lateral load capacity, one or two more drift levels were imposed on selected specimens.

3.3. Material Properties

For the wall pier and spandrel specimens tested at UCLA, the reinforcing steel was classified as Grade 280 (minimum yield strength of 280 MPa) by the manufacturer. Tensile tests were performed for the reinforcing bars through tensile coupon samples with a 203.2 mm (8 in) long reduced section (removed ribs). ϕ13 ($\neq$4) and ϕ 16 ($\neq$5) bars were tested in tension. Test data revealed that for Type 1, Type 2, and Type 5 wall specimens, the yield stress capacity for ϕ 13 bars was 424 MPa (61.5 ksi) and for 16 bars was 448.2 MPa (65 ksi). For Type 3 and Type 4 wall specimens, the yield stress capacity for ϕ 13 bars was 351.6 MPa (51 ksi). Steel stress-strain curves for bars used in Type 1 wall specimens are illustrated in Figure 3.12.

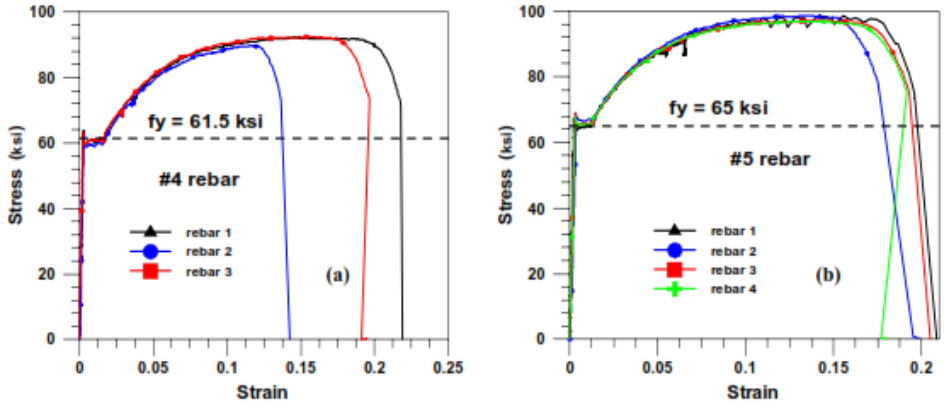

Figure 3.12. Steel Tensile Stress-Strain Curves for ϕ 13 and ϕ 16 bars of Type 1 Wall Specimen (Massone, 2006).

For the UCLA specimens, the targeted compressive strength range for concrete was 25 MPa - 30 MPa. Test-date average compressive strength values of the concrete used in construction of the specimens, are listed in Table 3.3.

Table 3.3. Average Compressive Strength of Concrete (Massone, 2006).

Specimen	f'$_c$ (Mpa)
WS-T1-S1	25.5
WS-T1-S2	43.7
WS-T2-S1	31.4
WS-T2-S2	31.0
WS-T3-S1	31.7
WS-T3-S2	33.6
WS-T4-S1	31.9
WS-T4-S2	33.0
WP-T5-N0-S1	29.9
WP-T5-N0-S2	31.0
WP-T5-N5-S1	31.9
WP-T5-N5-S2	32.0
WP-T5-N10-S1	28.3
WP-T5-N10-S2	31.4

For the wall specimens tested at Boğaziçi University, the targeted tensile strength of reinforcing bars tested was 420 MPa. Tensile tests were performed for the reinforcing bars through tensile coupon samples with 600 mm length. For the first set of specimens, there were two different diameter types, ϕ8 and ϕ16. The tension test results for the first set of specimens are provided in Figure 3.13. For the second and third set of specimens, ϕ14 reinforcing bars were used for the boundary elements of 0.33 aspect ratio specimen and ϕ22 reinforcing bars were used for the boundary bars of the 1.0 aspect ratio specimens. The tensile stress-strain properties of the bars used for the second and third sets are provided in Figure 3.14 and Figure 3.15.

For the Boğaziçi University specimens, the targeted compressive strength of concrete was 25 MPa - 30 MPa. The concrete used in specimen construction exhibited different test-date cylinder compressive strengths, ranging between 20 MPa - 35 MPa, depending on the date of testing. For each wall specimen, 3 standard (150 x 300 mm) cylinders were tested at the test date. Test-day average compressive strength values of concrete used in the construction of the specimens are listed in Table 3.4.

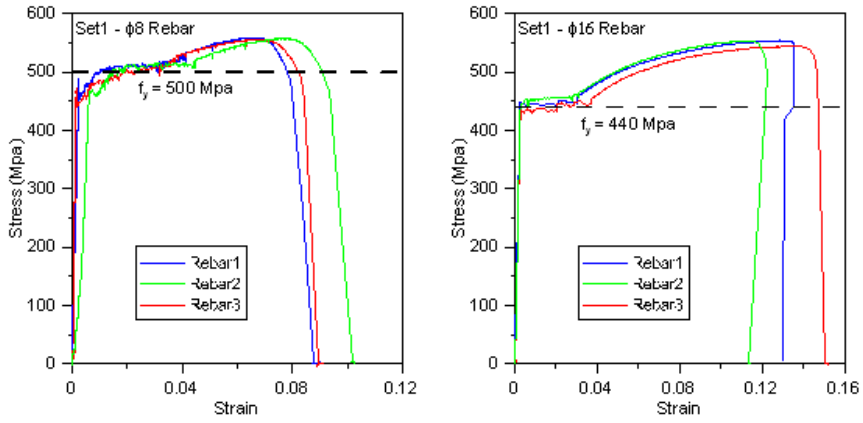

Figure 3.13. Steel Stress-Strain Curves for Specimen Set 1 (Terzioglu, 2011).

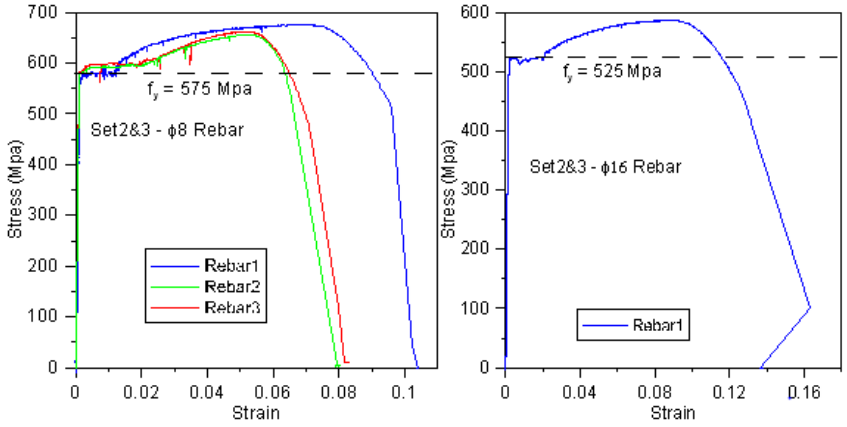

Figure 3.14. Steel Stress-Strain Curves for Web Reinforcement of Specimen Set 2 and Set 3 (Terzioglu, 2011).

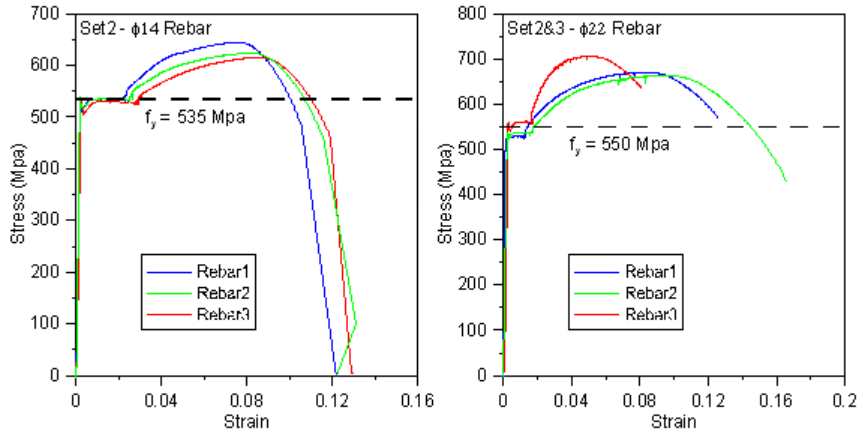

Figure 3.15. Steel Stress-Strain Curves for Boundary Reinforcement of Specimen Set 2 and Set 3 (Terzioglu, 2011).

Table 3.4. Average Compressive Strength of Concrete (Terzioglu, 2011).

Specimen	f'$_c$ (Mpa)
SW-T2-S1-1	19.3
SW-T1-S1-2	23.7
SW-T2-S2-3	25.8
SW-T2-S3-4	29.0
SW-T3-S1-5	32.1
SW-T4-S1-6	34.8
SW-T5-S1-7	35.0
SW-T6-S1-8	22.6
SW-T1-S2-9	24.0
SW-T1-N5-S1-10	26.3
SW-T1-N10-S1-11	27.0

3.4. Failure Modes of the Wall Specimens

Spandrel structural wall specimens tested at University of California Los Angeles experienced diagonal tension failure except for Type 4 specimens for which the failure mode was shear sliding. The important characteristic of the Type 4 specimens was the location of weakened plane joint, as it was located at the wall-pedestal interface. The wall pier specimens also experienced diagonal tension failure, due to their inadequate web reinforcement ratios.

For the walls tested at Boğaziçi University, all three types of shear failure were observed. Type 1 specimens failed under diagonal tension because of their relatively low web reinforcement ratio. Type 2, 4, 5, and 6 walls experienced diagonal compression failure. These walls incorporated relatively high reinforcing ratio in the web. For the special case of the Type 3 specimen, which had relatively low longitudinal reinforcement at wall boundaries, shear cracking at the wall-pedestal interface was observed, leading to sliding failure at the base of the wall.

For all of the wall specimens investigated, shear was the predominant mode of

behavior, while shear flexure interaction also played an important role in the response of the walls with an aspect ratio of 1.0. Degradation of lateral stiffness and lateral load capacity at low drift levels were common in all walls, together with highly-pinched lateral load-displacement behavior, indicating shear-controlled responses.

3.5. Calibration of the Model for the Wall Specimens

The finite element model configurations used for modeling and analysis of the test specimens were calibrated for several aspects of the wall specimens, including the geometric properties, reinforcement attributes, material characteristics, and loading conditions. As-tested properties of the materials employed in the construction of the specimens are used to calibrate the constitutive material parameters used in the model formulation. In calibration of the parameters for concrete and reinforcing steel in tension, tension stiffening effects were also considered. As well, the constitutive material parameters were also calibrated in terms of the expected compressive and the tensile stress-strain curves of concrete. Either as-tested material properties or well-established empirical relationships presented in the literature are implemented for calibrations. The material parameters were not adjusted to fit the model predictions with the experimental results obtained for the wall specimens. Further information on the calibration of the model is provided in this section.

3.5.1. Calibration of Model Element Dimensions and Reinforcement Ratios

Finite element models generated for the wall specimens were divided into an appropriate number of constitutive panel elements (mesh sizes) in order to obtain almost square-shaped constitutive elements. Corresponding dimensions and numbers of the constitutive model elements (mesh dimension and mesh number) for tests conducted at UCLA and Boğaziçi University are shown in Table 3.5 and Table 3.6, respectively. The reinforcement ratios in the boundary and web regions of the walls were calibrated according to the values presented in Table 3.1 and Table 3.2.

Table 3.5. Wall Model Geometry Details for Tests Conducted at UCLA.

Specimen	Model Element Dimension			Model Element Number		
	Horizontal		Vertical	Horizontal		Vertical
	Boundary Region	Web Region		Boundary Region	Web Region	
WS-T1-S1	16.9 cm	16.9 cm	16.9 cm	2	7	9
WS-T1-S2	16.9 cm	16.9 cm	16.9 cm	2	7	9
WS-T2-S1	12.8 cm	12.6 cm	12.7 cm	2	10	12
WS-T2-S2	12.8 cm	12.6 cm	12.7 cm	2	10	12
WS-T3-S1	12.8 cm	12.6 cm	12.7 cm	2	10	12
WS-T3-S2	12.8 cm	12.6 cm	12.7 cm	2	10	12
WS-T4-S1	12.8 cm	12.6 cm	12.7 cm	2	10	12
WS-T4-S2	12.8 cm	12.6 cm	12.7 cm	2	10	12
WP-T5-N0-S1	12.8 cm	12.4 cm	12.2 cm	2	9	10
WP-T5-N0-S2	12.8 cm	12.4 cm	12.2 cm	2	9	10
WP-T5-N5-S1	12.8 cm	12.4 cm	12.2 cm	2	9	10
WP-T5-N5-S2	12.8 cm	12.4 cm	12.2 cm	2	9	10
WP-T5-N10-S1	12.8 cm	12.4 cm	12.2 cm	2	9	10
WP-T5-N10-S2	12.8 cm	12.4 cm	12.2 cm	2	9	10

Table 3.6. Wall Model Geometry Details for Tests Conducted at Boğaziçi University.

Specimen	Model Element Dimension			Model Element Number		
	Horizontal		Vertical	Horizontal		Vertical
	Boundary Region	Web Region		Boundary Region	Web Region	
SW-T2-S1-1	13.0 cm	12.4 cm	12.5 cm	2	10	6
SW-T1-S1-2	13.0 cm	12.4 cm	12.5 cm	2	10	6
SW-T2-S2-3	13.0 cm	12.4 cm	12.5 cm	2	10	6
SW-T2-S3-4	13.0 cm	12.4 cm	12.5 cm	2	10	6
SW-T3-S1-5	11.4 cm	10.4 cm	10.7 cm	4	10	7
SW-T4-S1-6	13.0 cm	12.4 cm	12.5 cm	2	10	4
SW-T5-S1-7	13.0 cm	12.4 cm	12.5 cm	2	10	12
SW-T6-S1-8	13.0 cm	12.4 cm	12.5 cm	2	10	12
SW-T1-S2-9	9.7 cm	9.2 cm	9.4 cm	6	10	8
SW-T1-N5-S1-10	13.0 cm	12.4 cm	12.5 cm	2	10	6
SW-T1-N10-S1-11	13.0 cm	12.4 cm	12.5 cm	2	10	6

3.5.2. Calibration of Constitutive Material Parameters

Parameters of the constitutive material models implemented in the model formulation were calibrated to represent the as-tested properties of the materials used in the construction of the specimens, whenever available. Calibration studies were also conducted on the concrete constitutive model for representation of the shape of the stress-strain curve for concrete in compression. As well, the stress-strain behavior of concrete in tension and reinforcing steel in tension were calibrated to incorporate tension stiffening effects.

3.5.2.1. Calibration of the Constitutive Model for Reinforcing Steel. Belarbi and Hsu (1994) presented the average stress-strain relationship of the reinforcing steel bars covered by concrete and showed that the relationship differs from that of the bare bars, especially when the yield stress is of concern. When embedded in concrete, the yield stress of steel a bar due to the so-called tension stiffening effect. The stress-strain behavior of a bare bar and a bar embedded in concrete is illustrated in Figure 3.16.

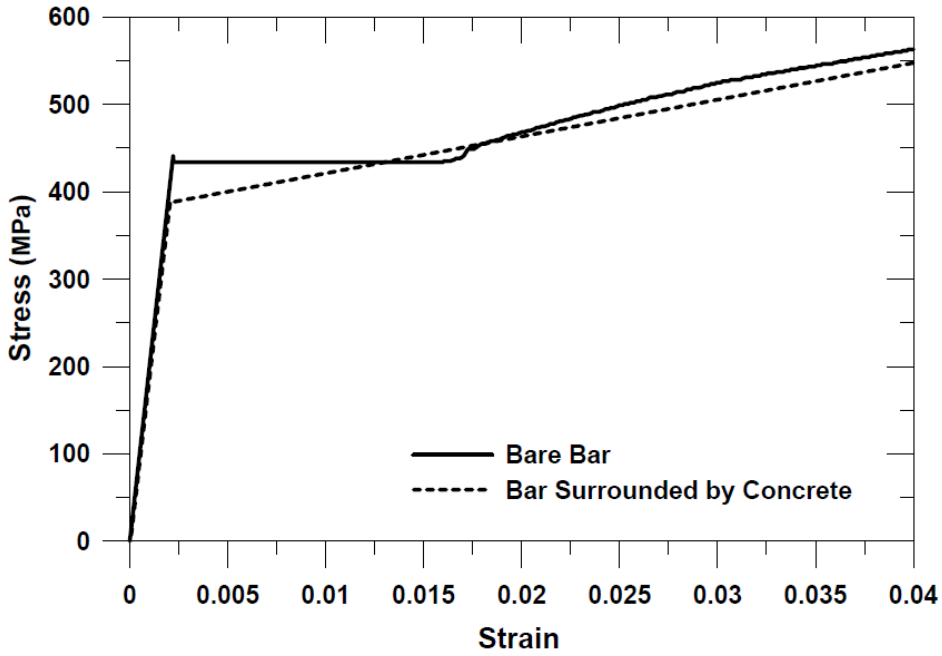

Figure 3.16. The Stress-Strain Behavior of Bare Rebar and Rebar Embedded in Concrete.

Experimental results conducted by Belarbi and Hsu (1994) on uniaxially-loaded column specimens form the basis for the empirical relationships between the behavior of bare bars and bars embedded in concrete is derived based on. The parameters affecting tension stiffening on the average yield stress of reinforcing steel are the cross-sectional area ratio of the longitudinal steel (ρ), and the ratio of concrete tensile strength (f_{cr}) to the yield stress of the bare bar (σ_y). Moreover, the strain hardening ratio of an embedded bar in concrete and the strain hardening ratio of a bare bar are found to be different.

The monotonic stress-strain envelope of bar embedded in concrete is represented

by two regions, the first is the elastic region with a slope equal to the elastic modulus of reinforcing steel (E_s), and the second is the post-yield range with a slope E^*_p(Figure 3.17).

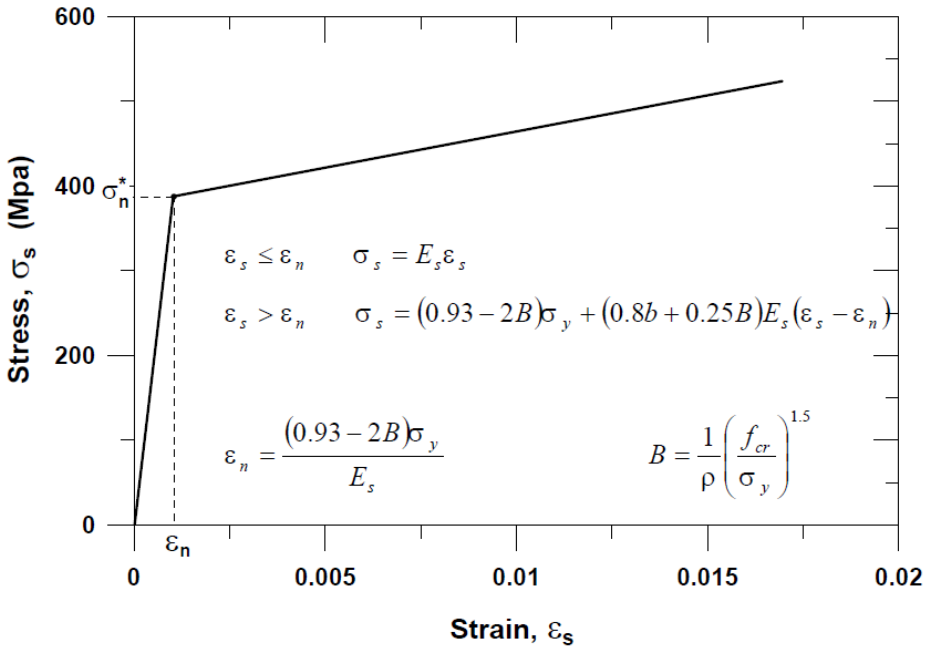

Figure 3.17. Stress-Strain Relationship for a Bar Embedded in Concrete (Belarbi and Hsu, 1994).

The effective yield stress at the intersection of the two regions ($\sigma*_n$) and the plastic slope (E^*_p) are given by the following expressions:

$$\sigma^*_n = (0.93 - 2B)\sigma_y \tag{3.1}$$

$$E^*_p = (0.8b + 0.25B)E_s \tag{3.2}$$

where B is defined as:

$$B = \frac{1}{\rho}\left(\frac{f_{cr}}{\sigma_y}\right)^{1.5} \tag{3.3}$$

and b is the strain hardening ratio (E_p/E_s) defined for the bare bar.

Accordingly, the model of Belarbi and Hsu (1994) for modeling the average stress-strain behavior of bars in concrete (Figure 3.17) is defined as:

$$\text{If} \quad \varepsilon_s \leq \varepsilon_n, \quad \sigma_s = E_s \varepsilon_s \tag{3.4}$$

$$\text{If} \quad \varepsilon_s > \varepsilon_n, \quad \sigma_s = (0.93 - -2B) + (0.8\text{b} + 0.25B)\, E_s(\varepsilon_s - \varepsilon_n) \tag{3.5}$$

where σ_s is the average stress, ε_s is the average strain and ε_n is the average strain defined at the intersection of the two lines as defined in equation below:

$$\varepsilon_n = \frac{\sigma_n^*}{E_s} = \frac{(0.93 - 2B)\,\sigma_y}{E_s} \tag{3.6}$$

In the equations above, E_s,σ_y and b are the modulus of elasticity, yield stress, and strain hardening ratio experimentally-measured for bare bars.

The calibrated parameters for the reinforcing steel bars in the wall specimens are presented in the following tables, which include the reinforcement ratios (ρ), the strain hardening slopes (E^*_p), and the stress (σ_n) and strain (ε_n) values at the intersection of the elastic and post-yield regions. Tension stiffening effects influence the constitutive parameters for reinforcing bars in tension only, whereas the parameters for bars in compression are identical to those obtained from bare bar tests.

Table 3.7, Table 3.8, and Table 3.9 represent the calibrated values for tests conducted at UCLA. There are two different bar diameters, ϕ13 and ϕ16. ϕ13 bars have different yield strength for Type 3 and Type 4 and remaining specimens.

Table 3.7. Calibrated Values of the Constitutive Parameters of Reinforcing Steel Bars for Specimens WS-T1-S1, WS-T1-S2, WS-T2-S1, and WS-T2-S2.

Specimen	Mesh Location	ϕ (mm)	ρ	Compression		Tension	
				f_y (Mpa)	b	$\sigma*_n$ (Mpa)	b'
WS-T1-S1	Boundary Mesh						
	Horizontal	ϕ13	0.278	424	0.00800	394	0.00660
	Vertical	ϕ16	3.12	448	0.00800	417	0.00642
	Web Mesh						
	Horizontal	ϕ13	0.278	424	0.00800	394	0.00660
	Vertical	ϕ13	0.428	424	0.00800	394	0.00653
WS-T1-S2	Boundary Mesh						
	Horizontal	ϕ13	0.278	424	0.00800	393	0.00670
	Vertical	ϕ16	3.12	448	0.00800	417	0.00642
	Inner Mesh						
	Horizontal	ϕ13	0.278	424	0.00800	393	0.00670
	Vertical	ϕ13	0.428	424	0.00800	394	0.00660
WS-T2-S1	Boundary Mesh						
	Horizontal	ϕ13	0.278	424	0.00800	394	0.00664
	Vertical	ϕ13-ϕ16	1.7	436	0.00800	405	0.00644
	Inner Mesh						
	Horizontal	ϕ13	0.278	424	0.00800	394	0.00664
	Vertical	ϕ13	0.4	424	0.00800	394	0.00656
WS-T2-S2	Boundary Mesh						
	Horizontal	ϕ13	0.278	424	0.00800	394	0.00663
	Vertical	ϕ13-ϕ16	1.7	436	0.00800	405	0.00644
	Inner Mesh						
	Horizontal	ϕ13	0.278	424	0.00800	394	0.00663
	Vertical	ϕ13	0.4	424	0.00800	394	0.00656

Table 3.8. Calibrated Values of the Constitutive Parameters of Reinforcing Steel Bars for Specimens WS-T3-S1, WS-T3-S2, WS-T4-S1, and WS-T4-S2.

Specimen	Mesh Location	ϕ (mm)	ρ	Compression		Tension	
				f_y (Mpa)	b	$\sigma*_n$ (Mpa)	b'
WS-T3-S1	Boundary Mesh						
	Horizontal	ϕ13	0.278	351.6	0.00800	326	0.00671
	Vertical	ϕ13	1.33	351.6	0.00800	327	0.00647
	Inner Mesh						
	Horizontal	ϕ13	0.278	351.6	0.00800	326	0.00671
	Vertical	ϕ13	0.256	351.6	0.00800	326	0.00674
WS-T3-S2	Boundary Mesh						
	Horizontal	ϕ13	0.278	351.6	0.00800	326	0.00673
	Vertical	ϕ13	1.33	351.6	0.00800	327	0.00647
	Inner Mesh						
	Horizontal	ϕ13	0.278	351.6	0.00800	326	0.00673
	Vertical	ϕ13	0.256	351.6	0.00800	326	0.00676
WS-T4-S1	Boundary Mesh						
	Horizontal	ϕ13	0.278	351.6	0.00800	326	0.00672
	Vertical	ϕ13	1.33	351.6	0.00800	327	0.00647
	Inner Mesh						
	Horizontal	ϕ13	0.278	351.6	0.00800	326	0.00672
	Vertical	ϕ13	0.256	351.6	0.00800	326	0.00674
WS-T4-S2	Boundary Mesh						
	Horizontal	ϕ13	0.278	351.6	0.00800	326	0.00672
	Vertical	ϕ13	1.33	351.6	0.00800	327	0.00647
	Inner Mesh						
	Horizontal	ϕ13	0.278	351.6	0.00800	326	0.00672
	Vertical	ϕ13	0.256	351.6	0.00800	326	0.00675

Table 3.9. Calibrated Values of the Constitutive Parameters of Reinforcing Steel Bars for Specimens WP-T5-N0-S1, WP-T5-N0-S2, WP-T5-N5-S1, WP-T5-N5-S2, WP-T5-N10-S1, and WP-T5-N10-S2.

Specimen	Mesh Location	ϕ (mm)	ρ	Compression		Tension	
				f_y (Mpa)	b	$\sigma*_n$ (Mpa)	b'
WP-T5-N0-S1	Boundary Mesh						
	Horizontal	ϕ13	0.278	424	0.00800	394	0.00663
	Vertical	ϕ13	1.33	424	0.00800	394	0.00645
	Inner Mesh						
	Horizontal	ϕ13	0.278	424	0.00800	394	0.00663
	Vertical	ϕ13	0.227	424	0.00800	393	0.00668
WP-T5-N0-S2	Boundary Mesh						
	Horizontal	ϕ13	0.278	424	0.00800	394	0.00663
	Vertical	ϕ13	1.33	424	0.00800	394	0.00645
	Inner Mesh						
	Horizontal	ϕ13	0.278	424	0.00800	394	0.00663
	Vertical	ϕ13	0.227	424	0.00800	393	0.00669
WP-T5-N5-S1	Boundary Mesh						
	Horizontal	ϕ13	0.278	424	0.00800	394	0.00664
	Vertical	ϕ13	1.33	424	0.00800	394	0.00645
	Inner Mesh						
	Horizontal	ϕ13	0.278	424	0.00800	394	0.00664
	Vertical	ϕ13	0.227	424	0.00800	393	0.00669
WP-T5-N5-S2	Boundary Mesh						
	Horizontal	ϕ13	0.278	424	0.00800	394	0.00664
	Vertical	ϕ13	1.33	424	0.00800	394	0.00645
	Inner Mesh						
	Horizontal	ϕ13	0.278	424	0.00800	394	0.00664
	Vertical	ϕ13	0.227	424	0.00800	393	0.00669
WP-T5-N10-S1	Boundary Mesh						
	Horizontal	ϕ13	0.278	424	0.00800	394	0.00662
	Vertical	ϕ13	1.33	424	0.00800	394	0.00645
	Inner Mesh						
	Horizontal	ϕ13	0.278	424	0.00800	394	0.00662
	Vertical	ϕ13	0.227	424	0.00800	393	0.00667
WP-T5-N10-S2	Boundary Mesh						
	Horizontal	ϕ13	0.278	424	0.00800	394	0.00664
	Vertical	ϕ13	1.33	424	0.00800	394	0.00645
	Inner Mesh						
	Horizontal	ϕ13	0.278	424	0.00800	394	0.00664
	Vertical	ϕ13	0.227	424	0.00800	393	0.00669

Tables Table 3.10, Table 3.11, and Table 3.12 represent the calibrated values for tests conducted at Boğaziçi University. There are four different bar diameters. ϕ8, ϕ14, ϕ16, and ϕ22 were used for boundary regions while ϕ8 was used to reinforce the web regions in the specimens.

Table 3.10. Calibrated Values of the Constitutive Parameters of Reinforcing Steel Bars for Specimens SW-T2-S1-1, SW-T1-S1-2, and SW-T2-S2-3.

Specimen	Mesh Location	ϕ (mm)	ρ	Compression		Tension	
				f_y (Mpa)	b	$\sigma*_n$ (Mpa)	b'
SW-T2-S1-1	Boundary Mesh						
	Horizontal	ϕ8	0.68	500	0.00323	465	0.00261
	Vertical	ϕ16	5.15	440	0.0043	409	0.00345
	Web Mesh						
	Horizontal	ϕ8	0.68	500	0.00323	465	0.00261
	Vertical	ϕ8	0.68	500	0.00323	465	0.00261
SW-T1-S1-2	Boundary Mesh						
	Horizontal	ϕ8	0.34	500	0.00323	465	0.00266
	Vertical	ϕ16	5.15	440	0.0043	409	0.00345
	Inner Mesh						
	Horizontal	ϕ8	0.34	500	0.00323	465	0.00266
	Vertical	ϕ8	0.34	500	0.00323	465	0.00266
SW-T2-S2-3	Boundary Mesh						
	Horizontal	ϕ8	0.68	500	0.00323	465	0.00262
	Vertical	ϕ16	5.15	440	0.0043	409	0.00345
	Inner Mesh						
	Horizontal	ϕ8	0.68	500	0.00323	465	0.00262
	Vertical	ϕ8	0.68	500	0.00323	465	0.00262

Table 3.11. Calibrated Values of the Constitutive Parameters of Reinforcing Steel Bars for Specimens SW-T2-S3-4, SW-T3-S1-5, SW-T4-S1-6, and SW-T5-S1-7.

Specimen	Mesh Location	ϕ (mm)	ρ	Compression		Tension	
				f_y (Mpa)	b	$\sigma*_n$ (Mpa)	b'
	Boundary Mesh						
SW-T2-S3-4	Horizontal	ϕ8	0.68	575	0.00815	535	0.00656
	Vertical	ϕ16	5.15	525	0.00282	488	0.00227
	Inner Mesh						
	Horizontal	ϕ8	0.68	575	0.00815	535	0.00656
	Vertical	ϕ8	0.68	575	0.00815	535	0.00656
SW-T3-S1-5	Boundary Mesh						
	Horizontal	ϕ8	0.68	575	0.00815	535	0.00657
	Vertical	ϕ8	0.65	575	0.00815	535	0.00657
	Inner Mesh						
	Horizontal	ϕ8	0.68	575	0.00815	535	0.00657
	Vertical	ϕ8	0.68	575	0.00815	535	0.00657
SW-T4-S1-6	Boundary Mesh						
	Horizontal	ϕ8	0.68	575	0.00815	534	0.00658
	Vertical	ϕ14	3.95	535	0.00395	498	0.00317
	Inner Mesh						
	Horizontal	ϕ8	0.68	575	0.00815	534	0.00658
	Vertical	ϕ8	0.68	575	0.00815	534	0.00658
SW-T5-S1-7	Boundary Mesh						
	Horizontal	ϕ8	0.68	575	0.00815	534	0.00658
	Vertical	ϕ22	9.75	550	0.00647	511	0.00518
	Inner Mesh						
	Horizontal	ϕ8	0.68	575	0.00815	534	0.00658
	Vertical	ϕ8	0.34	575	0.00815	534	0.00663

Table 3.12. Calibrated Values of the Constitutive Parameters of Reinforcing Steel Bars for Specimens SW-T6-S1-8, SW-T1-S2-9, SW-T1-N5-S1-10, and SW-T1-N10-S1-11.

Specimen	Mesh Location	ϕ (mm)	ρ	Compression		Tension	
				f_y (Mpa)	b	$\sigma*_n$ (Mpa)	b'
	Boundary Mesh						
SW-T6-S1-8	Horizontal	ϕ8	0.68	575	0.00815	535	0.00655
	Vertical	ϕ22	9.75	550	0.00647	511	0.00518
	Inner Mesh						
	Horizontal	ϕ8	0.68	575	0.00815	535	0.00655
	Vertical	ϕ8	0.68	575	0.00815	535	0.00655
SW-T1-S2-9	Boundary Mesh						
	Horizontal	ϕ8	0.34	575	0.00815	534	0.00659
	Vertical	ϕ16	5.15	525	0.00282	488	0.00226
	Inner Mesh						
	Horizontal	ϕ8	0.34	575	0.00815	534	0.00659
	Vertical	ϕ8	0.34	575	0.00815	534	0.00659
SW-T1-N5-S1-10	Boundary Mesh						
	Horizontal	ϕ8	0.34	575	0.00815	534	0.00659
	Vertical	ϕ16	5.15	525	0.00282	488	0.00226
	Inner Mesh						
	Horizontal	ϕ8	0.34	575	0.00815	534	0.00659
	Vertical	ϕ8	0.34	575	0.00815	534	0.00659
SW-T1-N10-S1-11	Boundary Mesh						
	Horizontal	ϕ8	0.34	575	0.00815	534	0.00660
	Vertical	ϕ16	5.15	525	0.00282	488	0.00226
	Inner Mesh						
	Horizontal	ϕ8	0.34	575	0.00815	534	0.00660
	Vertical	ϕ8	0.34	575	0.00815	534	0.00660

3.5.2.2. Calibration of the Constitutive Model for Concrete. The constitutive material parameters were adjusted through calibration studies to represent the stress-strain curve for concrete in compression and in tension. The compression envelope curve of the model by Chang and Mander (1994) is defined by the initial slope E_c (elastic modulus of concrete), the peak coordinate (ε'_c, f'_c), a parameter r from Tsai's (1988) equation defining the shape of the envelope curve, and the parameter $x'_{cr} > 1$ to define the normalized strain at which the stress-strain curve transforms into a straight line (Figure 3.18).

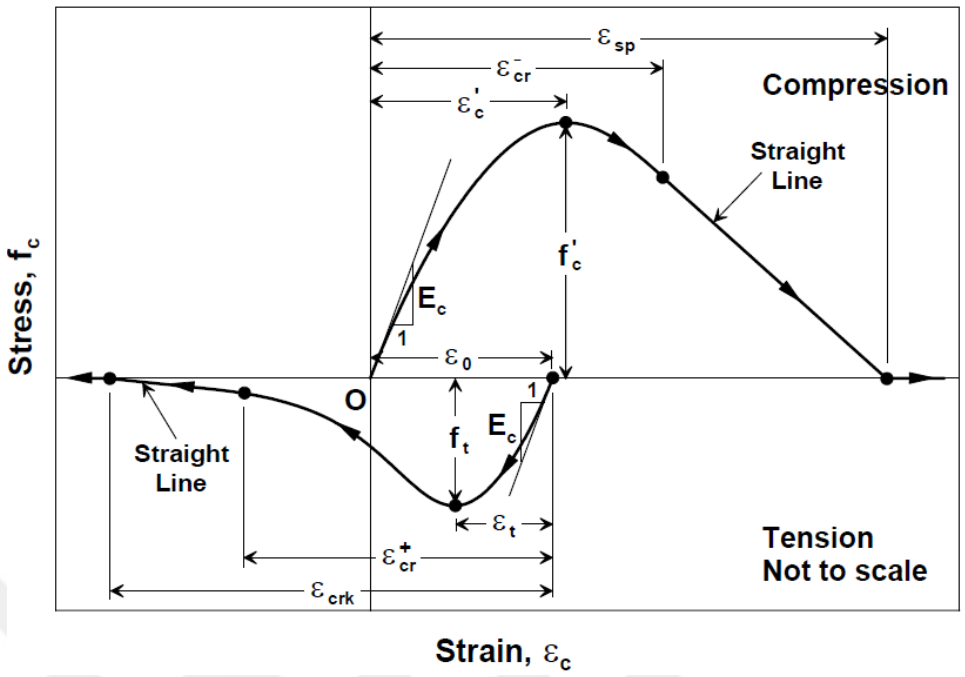

Figure 3.18. Compression and Tension Envelope Curves of the Model by Chang and Mander (1994).

The calibration of the material properties of concrete in compression and in tension was conducted using different criteria. For concrete in compression, the empirical relationships recommended by Chang and Mander were utilized for the constitutive parameters expect for the as-tested compressive strength. In order to calibrate the critical strain parameter which defines the strain value at which the envelope curve transitions into a straight line, the Saatcioglu-Razvi Model (1992) for concrete in compression was also implemented. For concrete in tension, the constitutive parameters of the model were calibrated to represent the empirical relationships suggested by Belarbi and Hsu (1994), represent tension stiffening effects on the tensile stress-strain behavior of concrete.

Concrete in Compression: The parameters constituting the compression envelope curve are the compressive strength of concrete (f'_c), the strain at compressive strength (ε'_c), the initial Young's Modulus (E_c), the parameter r defining the shape of the envelope and the normalized critical strain $\bar{x}_{cr}$(also named x_{cr}) where the curve transitions into a straight line. Chang and Mander (1994) recommend empirical relationships for

the parameters E_c, ε'_c and r as:

$$Initial\ modulus\ of\ elasticity: \quad E_c = 8200(f'_c)^{(3/8)} \tag{3.7}$$

$$Strain\ at\ compressive\ strength: \quad \varepsilon'_c = \frac{(f'_c)^{0.25}}{28} \tag{3.8}$$

$$Shape\ parameter: \quad r = \frac{f'_c}{5.2} - 1.9 \tag{3.9}$$

The unit of f'$_c$ in the empirical formulas above is MPa.

For the normalized critical strain parameter x_{crn}, the parameter was calibrated graphically by comparing the shape of the stress-strain envelope of the Chang and Mander (1994) model with the Saatcioglu and Razvi (1992) model for unconfined concrete due to the absence of an empirical relationship. The calibration criterion was to attain parallel straight lines in the descending region of the two stress-strain relationships, as shown in Figure 3.19. In order to obtain the calibrated x_{crn} values, numerous trials were conducted for each individual specimen. Calibrated constitutive parameters for concrete in compression are presented in Table 3.13 and Table 3.14 for all wall specimens.

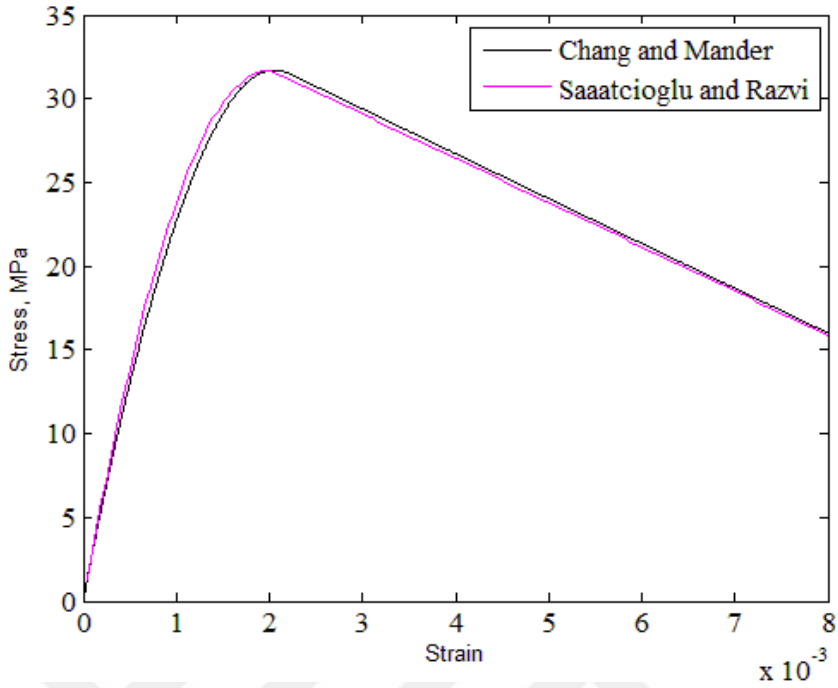

Figure 3.19. Stress-Strain Diagrams for Concrete in Compression for WS-T3-S2.

Table 3.13. Calibrated Values of the Constitutive Parameters for Concrete in Compression for the UCLA Specimens.

Specimen	f'$_c$ (Mpa)	E$_c$ (Mpa)	ε'_c	r	X$_{crn}$
WS-T1-S1	25.5	27778	0.00183	3.031	1.110
WS-T1-S2	43.7	33996	0.00236	6.551	1.054
WS-T2-S1	31.4	30033	0.00217	4.172	1.095
WS-T2-S2	31.0	29889	0.00204	4.095	1.086
WS-T3-S1	31.7	30140	0.00206	4.230	1.084
WS-T3-S2	33.6	30805	0.00209	4.598	1.075
WS-T4-S1	31.9	30211	0.00206	4.269	1.082
WS-T4-S2	33.0	30598	0.00208	4.482	1.078
WP-T5-N0-S1	29.9	29486	0.00248	3.882	1.145
WP-T5-N0-S2	31.0	29889	0.00266	4.095	1.155
WP-T5-N5-S1	31.9	30211	0.00231	4.269	1.105
WP-T5-N5-S2	32.0	30247	0.00246	4.288	1.118
WP-T5-N10-S1	28.3	28885	0.00210	3.573	1.116
WP-T5-N10-S2	31.4	30033	0.00254	4.172	1.130

Table 3.14. Calibrated Values of the Constitutive Parameters for Concrete in Compression for the Boğaziçi University Specimens.

Specimen	f'$_c$ (Mpa)	E$_c$ (Mpa)	ε'_c	r	X$_{crn}$
SW-T2-S1-1	19.3	25022	0.00182	1.832	1.320
SW-T1-S1-2	23.7	27026	0.00191	2.683	1.155
SW-T2-S2-3	25.8	27900	0.00196	3.089	1.127
SW-T2-S3-4	29.0	29150	0.00201	3.708	1.098
SW-T3-S1-5	32.1	30282	0.00207	4.308	1.081
SW-T4-S1-6	34.8	31213	0.00211	4.830	1.070
SW-T5-S1-7	35.0	31280	0.00211	4.868	1.069
SW-T6-S1-8	22.6	26548	0.00189	2.470	1.178
SW-T1-S2-9	24.0	27153	0.00192	2.741	1.152
SW-T1-N5-S1-10	26.3	28101	0.00196	3.186	1.121
SW-T1-N10-S1-11	27.0	28380	0.00198	3.321	1.115

Concrete in Tension: The constitutive parameters to be calibrated for concrete in tension consist of the initial Young's modulus of the average stress-strain relationship (E$_g$), the tensile (cracking) strength of concrete (f$_{cr}$), and the strain at cracking (ε_{cr}), the parameter r representing the shape of the curve, and the normalized critical strain at which the stress-strain curve becomes a straight line (x$_{crp}$). Since material test results were not available for these parameters, and the effects of tension stiffening on concrete in tension needed to be incorporated, these parameters were calibrated so that the tensile stress-strain relationship for concrete in tension is compatible with the empirical relationships suggested by Belarbi and Hsu (1994) for concrete in tension. The average stress-strain relationship proposed by Belarbi and Hsu (1994) for concrete in tension (Figure 3.20) is defined by the following equations:

$$If \quad \varepsilon_c > \varepsilon_{cr} \quad then \quad \sigma_c = E_c \varepsilon_c \tag{3.10}$$

$$If \quad \varepsilon_c > \varepsilon_{cr} \quad then \quad \sigma_c = f_{cr}\left(\frac{\varepsilon_{cr}}{\varepsilon_c}\right)^{0.4} \tag{3.11}$$

where

$$E_c = 3875\sqrt{f'_c(MPa)} \tag{3.12}$$

$$f_{cr} = 0.31\sqrt{f'_c(MPa)} \tag{3.13}$$

$$\varepsilon_{cr} = 0.00008 \tag{3.14}$$

The stress-strain relationship of Belarbi and Hsu (1994) consists of two regions, the first of which is the linear region, and the second of which is the exponentially-descending region, as illustrated in Figure 3.20.

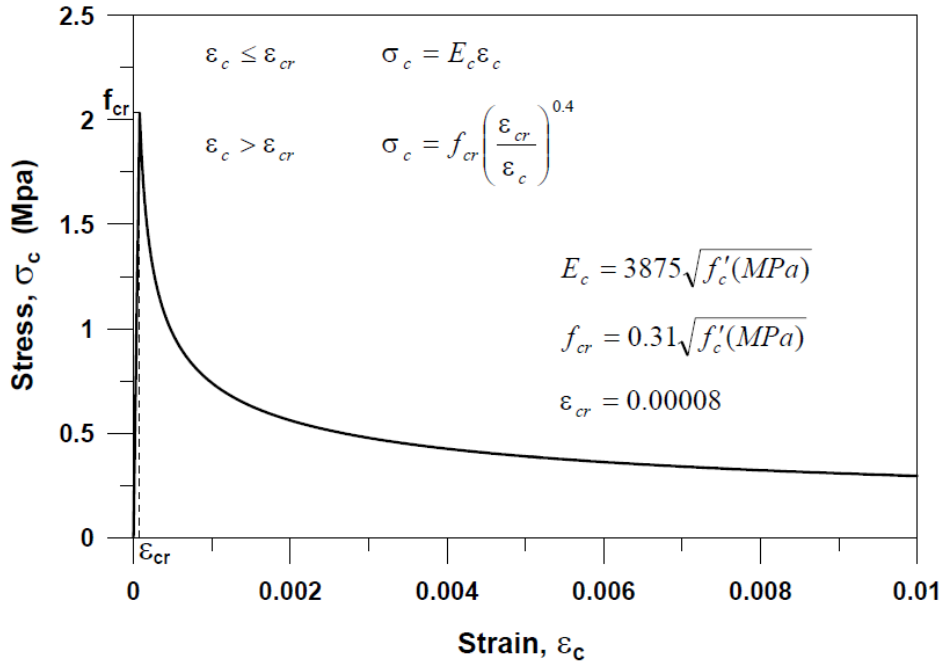

Figure 3.20. Stress-Strain Relationship for Concrete in Tension (Belarbi and Hsu, 1994).

The normalized critical strain value for concrete in tension, at which the stress-strain curve becomes a straight line (x_{crp}), was calibrated for a very large value (e.g., 10000), so that the curve does not transform into a straight line and continues as a

curve, the shape of which resembles the descending region of the relationship by Belarbi and Hsu (1994). The parameter r_r(controlling the shape of the tension envelope) was calibrated graphically by comparing the shape of the stress-strain diagram obtained by the Chang and Mander (1994) model with the Belarbi and Hsu (1994) relationship, so that similar shapes are obtained for the stress-strain curves, as displayed in Figure 3.21. The calibrated parameters of concrete in tension are presented in Table 3.15 and Table 3.16 for all wall specimens.

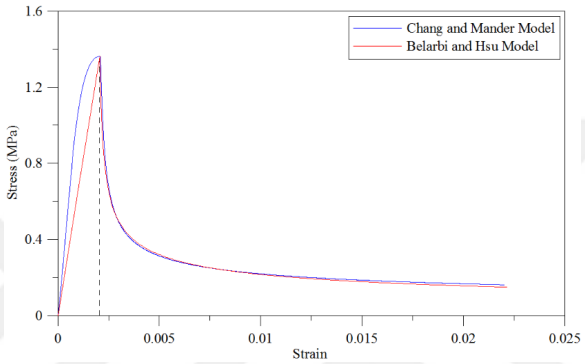

Figure 3.21. Stress-Strain Diagrams for Concrete in Tension for SW-T2-S1-1.

Table 3.15. Calibrated Values of the Constitutive Parameters for Concrete in Tension for the UCLA Specimens.

Specimen	E_c (Mpa)	f_{cr} (Mpa)	ε_{cr}	r_t	X_{crp}
WS-T1-S1	27778	1.5654	0.00008	1.2400	10000
WS-T1-S2	33996	2.0493	0.00008	1.2270	10000
WS-T2-S1	30033	1.7371	0.00008	1.2380	10000
WS-T2-S2	29889	1.7260	0.00008	1.2380	10000
WS-T3-S1	30140	1.7454	0.00008	1.2380	10000
WS-T3-S2	30805	1.7969	0.00008	1.2377	10000
WS-T4-S1	30211	1.7509	0.00008	1.2380	10000
WS-T4-S2	30598	1.7808	0.00008	1.2377	10000
WP-T5-N0-S1	29486	1.6951	0.00008	1.2380	10000
WP-T5-N0-S2	29889	1.7260	0.00008	1.2380	10000
WP-T5-N5-S1	30211	1.7509	0.00008	1.2380	10000
WP-T5-N5-S2	30247	1.7536	0.00008	1.2380	10000
WP-T5-N10-S1	28885	1.6491	0.00008	1.2390	10000
WP-T5-N10-S2	30033	1.7371	0.00008	1.2380	10000

Table 3.16. Calibrated Values of the Constitutive Parameters for Concrete in Tension for the Boğaziçi University Specimens.

Specimen	E_c (Mpa)	f_{cr} (Mpa)	ε_{cr}	r_t	X_{crp}
SW-T2-S1-1	25022	1.362	0.00008	1.25	10000
SW-T1-S1-2	27026	1.509	0.00008	1.25	10000
SW-T2-S2-3	27900	1.575	0.00008	1.25	10000
SW-T2-S3-4	29150	1.669	0.00008	1.24	10000
SW-T3-S1-5	30282	1.756	0.00008	1.24	10000
SW-T4-S1-6	31213	1.829	0.00008	1.23	10000
SW-T5-S1-7	31280	1.834	0.00008	1.23	10000
SW-T6-S1-8	26548	1.474	0.00008	1.25	10000
SW-T1-S2-9	27153	1.519	0.00008	1.25	10000
SW-T1-N5-S1-10	28101	1.590	0.00008	1.24	10000
SW-T1-N10-S1-11	28380	1.611	0.00008	1.24	10000

4. COMPARISON OF ANALYTICAL AND EXPERIMENTAL RESULTS

This chapter presents comparison of the experimental results obtained from the aforementioned wall test programs with predictions of the finite element model calibrated as described in the previous chapter, in an effort to validate the applicability of the model in representing the response of structural walls with aspect ratio less than or equal to 1.0. Lateral load vs. top displacement response comparisons for a total of 15 wall specimens are presented for brevity, since some of the wall specimens tested were identical to each other. Analysis results presented in the comparisons consider the influence of the improved shear aggregate interlock and dowel action constitutive models with the cyclic strength degradation parameters implemented in this study.

4.1. Wall Specimens Tested at University of California Los Angeles

The squat wall tests conducted at UCLA were simulated as per their boundary and loading conditions, with a fixed end condition at the bottom and zero rotation at the top (via the rigid body constraint enforced at the top), together with a double-curvature moment diagram along wall height. The number of loading cycles to each target drift level was the same in the analyses as applied during testing, since the number of cycles is the governing parameter associated with cyclic strength degradation in the constitutive shear aggregate interlock and dowel action models implemented. The test results were processed to remove the contribution of strain penetration effects on top lateral displacements as described in Section 2.3.4, and the processed top displacement histories were used in the analyses. As a common response characteristic of all wall spandrel specimens tested, which had weakened plane joints at wall mid-height or wall-pedestal interface, the lateral load - displacement response was moderately unsymmetrical in positive and negative loading directions. As there were two specimens with identical properties for each specimen type, the comparisons are presented for one specimen of each type only, except for the Type 1 specimens for which the concrete

compressive strength differs significantly (25.5 MPa and 43.7 MPa for WS-T1-S1 and WS-T1-S2, respectively). All wall spandrels had an aspect ratio of 1.00 while all wall piers had an aspect ratio of 0.89, and shear span-to-depth ratios for all specimens was equal to half of the aspect ratio, due to the double-curvature loading condition.

Figure 4.1 shows the lateral load vs. top displacement response of Type 1 wall specimen WS-T1-S1. The model predicts the initial stiffness of the wall, as well as the reduction in the stiffness (more than 50%) due to the diagonal cracking, reasonably well. The model overestimates the wall lateral load capacity in the negative loading direction, and underestimates ductility of the wall. The specimen experiences pronounced pinching due to closure of diagonal cracks, which is also present, although less pronounced, in the model results.

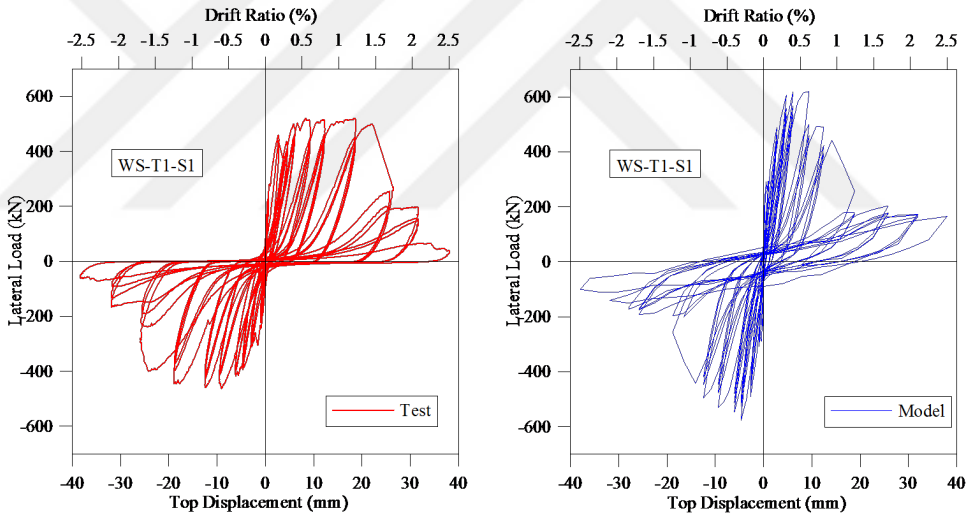

Figure 4.1. Lateral Load - Top Displacement Response of Specimen WS-T1-S1.

The lateral load vs. top displacement response of Type 1 wall specimen WS-T1-S2 is presented in Figure 4.2. The concrete compressive strength of this specimen was relatively higher compared to the other specimen of same type (WS-T1-S1) which increased the lateral load capacity of the wall which reflected on both the test results and the model predictions. The model slightly underestimates the initial and cracked stiffness of the wall, but captures its ductility reasonably well. The degradation estimated by the model tends to decrease the capacity more mildly, compared to the test results. The lateral load capacity of the wall in the negative direction was predicted

accurately by the model; however, the model slightly underestimates the capacity in the positive loading direction. Pinching characteristics of the response are captured by the model fairly well.

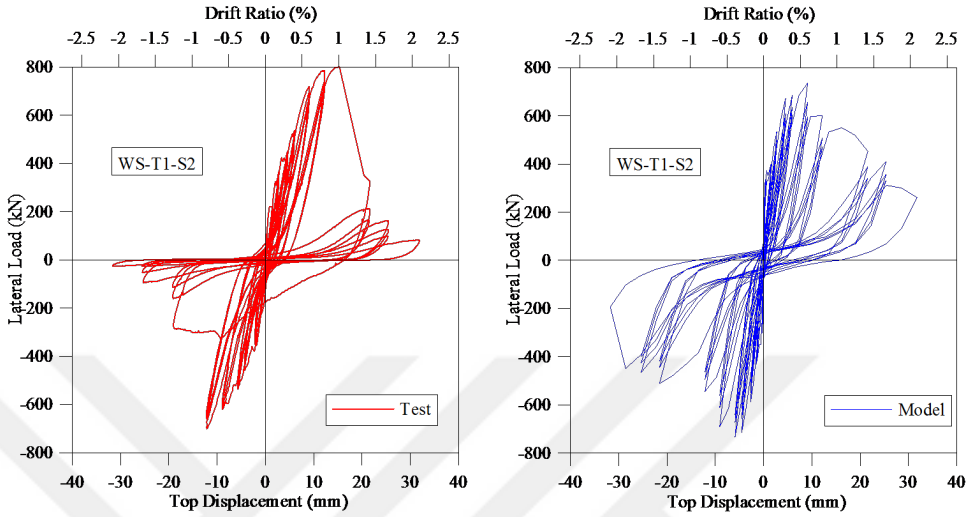

Figure 4.2. Lateral Load - Top Displacement Response of Specimen WS-T1-S2.

The lateral load vs. top displacement response comparison for the Type 2 wall specimen WS-T2-S2, shown in Figure 4.3, indicates similar initial stiffness predicted by the model and measured for the wall specimen. For this wall, lateral load response does not degrade immediately after the capacity is reached, which is also reflected in the analytical results. The beginning of loss of lateral load capacity is significantly affected by the difference in the amount of boundary reinforcement among Type 1 and Type 2 specimens, as the behavior is more brittle in Type 1 walls with larger boundary reinforcement, whereas capacity is maintained for several cycles in the case of Type 2 specimens, due to flexural yielding of the lesser amount of boundary reinforcement. The lateral load capacity of specimen WS-T2-S2 in the positive loading direction is captured by the model, while the capacity in the negative direction is underestimated. Ductility prediction of the model in the positive loading direction is also reasonable. At 1.5% drift level, crushing of concrete caused drastic reduction in the experimentally-measured lateral load capacity of the wall specimen. Degradation in lateral load capacity estimated by the model is relatively more gradual.

Type 3 wall specimens have relatively lower longitudinal web reinforcement ratio

compared to the first two types. With the presence of a weakened plane joint at wall midheight, where some of the longitudinal web bars are cut, the lateral load capacity of these specimens decrease. Figure 4.4 shows the response comparison for specimen WS-T3-S1. The initial and cracked stiffness of the wall is well-estimated by the model. The model also predicts the lateral load capacity of the wall fairly accurately, especially in the positive loading direction. The lateral load degradation behavior is predicted reasonably by the model, although the sudden decrease in lateral load observed in the test result at 1.5% drift in the negative direction causes the model to slightly overestimate the lateral load during loading cycles to larger drift. Pinching behavior of the specimen is also represented by the model fairly well, although the analytical response is slightly less-pinched.

All pier walls (Type 5) specimens tested at University of California Los Angeles had identical dimensions and reinforcement details. Concrete compressive strength of all wall pier specimens were also very similar. As no weakened plane joint is present in the walls, the control parameter investigated was the influence of axial load level on the wall response.

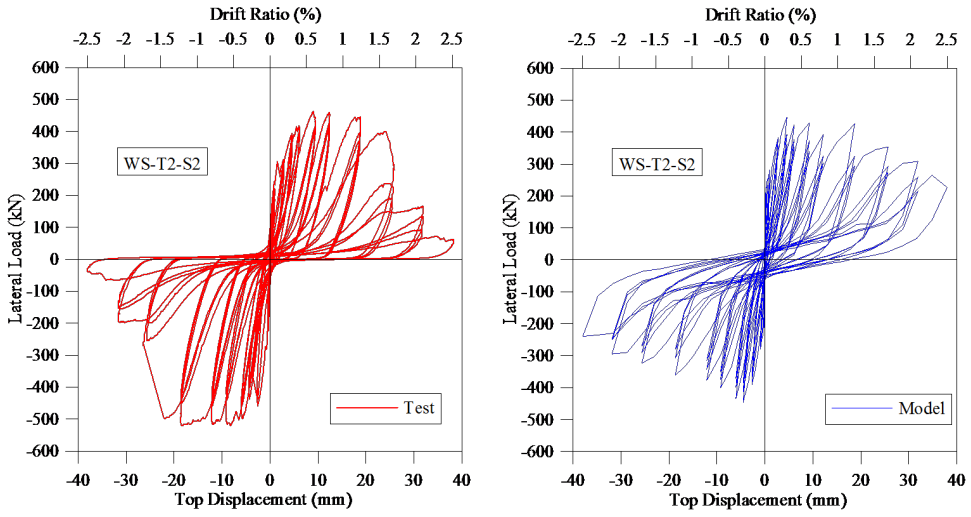

Figure 4.3. Lateral Load - Top Displacement Response of Specimen WS-T2-S2.

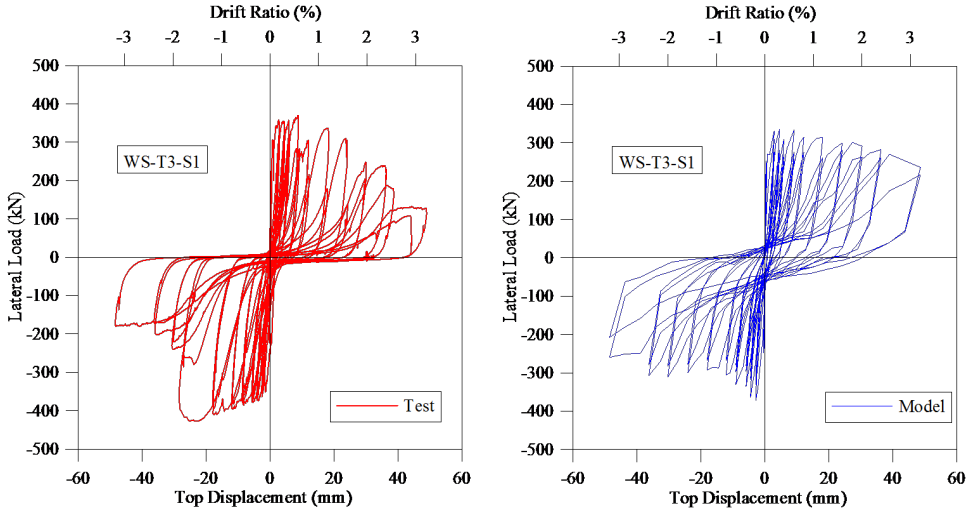

Figure 4.4. Lateral Load - Top Displacement Response of Specimen WS-T3-S1.

As can be observed in Figure 4.5, for Type 5 (wall pier) specimen WP-T5-N0-S1 with no axial load, the initial and cracked stiffness is well-captured by the model, while lateral load capacity is estimated fairly well in the positive loading direction and is overestimated in the negative loading direction. Ductility prediction of the model is also reasonable. The model estimates a more gradual degradation in the lateral load after capacity is reached. In the test results, a more sudden decrease in lateral load takes place due to the formation of a single large diagonal crack on the specimen, which decreases accuracy of the model in predicting the lateral load at larger drift levels. For this specimen, the model also fails to represent the pronounced pinching behavior observed in the test result, because of the same reason.

As depicted in Figure 4.6 for Type 5 specimen WP-T5-N5-S1, subjected to an axial load corresponding to 5% of its axial load capacity, the model exhibits good accuracy in predicting the stiffness, lateral load capacity, and ductility characteristics of the wall, in both positive and negative loading directions. The failure mode of this specimen was formation of diagonal cracks followed by crushing of concrete at the wall center, resulting in pronounced degradation in the lateral load. This degradation in lateral load, although captured by the model, is more gradual in the analytical results.

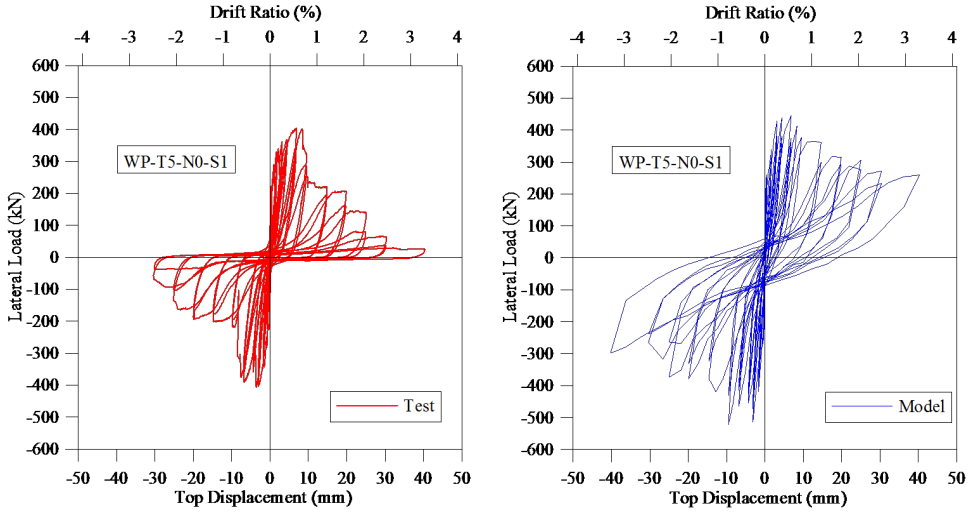

Figure 4.5. Lateral Load - Top Displacement Response of Specimen WP-T5-N0-S1.

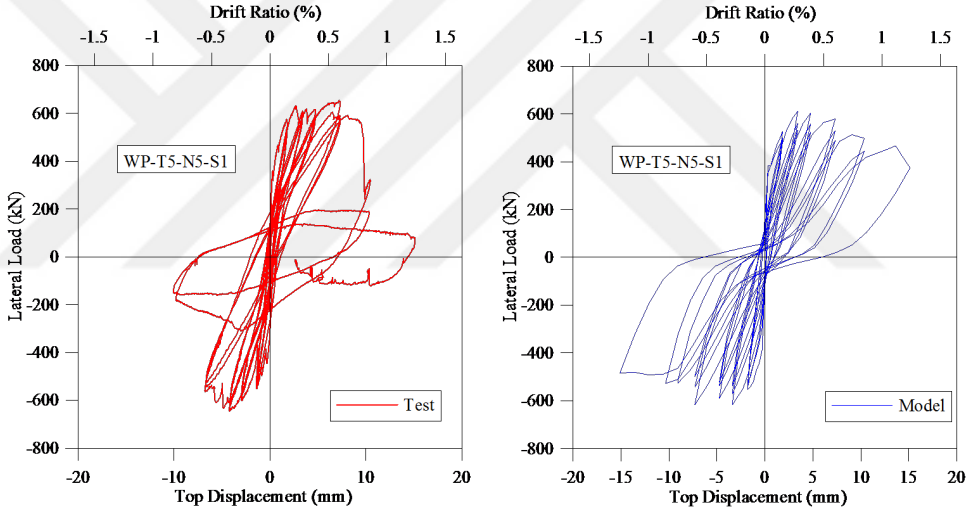

Figure 4.6. Lateral Load - Top Displacement Response of Specimen WP-T5-N5-S1.

A similar correlation was obtained for Type 5 specimen WP-T5-N10-S2, subjected to as axial load corresponding to 10% of its axial load capacity. The response was well-predicted by the model in terms of stiffness, lateral load capacity, and ductility. The failure mode of this specimen was also crushing of concrete at the wall center, resulting in sudden degradation in lateral load, which was captured by the model, although the model predicted relatively more gradual degradation.

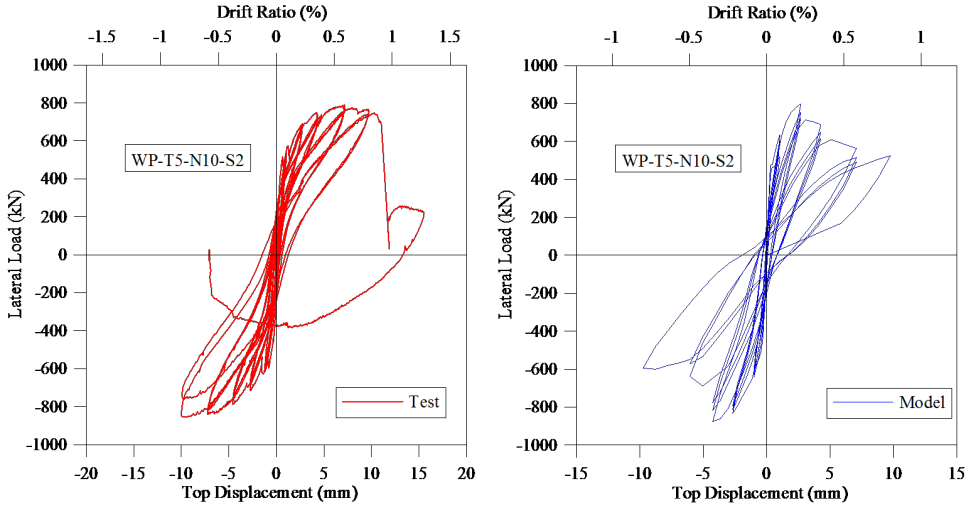

Figure 4.7. Lateral Load - Top Displacement Response of Specimen WP-T5-N10-S2.

It is a significant attribute that the overall response prediction of the model for the axially-loaded wall specimens (WP-T5-N5-S1 and WP-T5-N10-S2) is accurate, because the model is apparently successful in representing the influence the axial load on the shear-controlled response characteristics of walls. Considering that design codes and standards neglect the influence of axial load in calculation of the shear strength and stiffness of RC walls, mainly due to lack of experimental data, availability of a modeling approach considering interaction between axial load and shear capacity is promising towards improvement of code provisions on wall shear strength.

4.2. Wall Specimens Tested at Boğaziçi University

The wall tests conducted at Boğaziçi University were also simulated as per their loading conditions, top displacement history, and the number of loading cycles applied at each target drift level. As companion specimens with identical properties exist for most of the specimen types, the comparisons between analytical and experimental results are presented for one specimen of each type only, unless there is a significant difference in the concrete compressive strength of the identical specimens or the applied axial load level.

Among Type 1 wall specimens which all have an aspect ratio of 0.5, SW-T1-

S1-2 and SW-T1-S2-9 have the same properties in terms of dimensions, reinforcement ratios, and loading history; and there is no axial load applied on these specimens. The measured and predicted lateral load vs. top displacement responses of specimen SW-T1-S1-2 are compared in Figure 4.8. The failure mode of this specimen was diagonal tension, where crushing of concrete propagated along diagonal struts. The initial stiffness is reasonably captured by the model, although the cracked stiffness is overestimated. The lateral load capacity of the specimen is slightly overestimated in the negative loading direction, whereas it is well-predicted in the positive loading direction. For this specimen, at 1.2% drift level, concrete started to crush at the center of the wall, initiating strength degradation. The model overestimates the ductility for the wall; however, degradation of the lateral load and pinching behavior are represented fairly well.

The remaining Type 1 wall specimens were subjected to axial load during the tests. Specimen SW-T1-N5-S1-10, the properties of which were identical to SW-T1-S2-9, was tested under 5% axial load level. The model captured the increase observed in the lateral load capacity of the specimen due to applied axial load, as depicted in Figure 4.8. The model overestimated the stiffness of the wall and underestimated its ductility; however, degradation in the lateral load and pinching characteristics were reasonably predicted.

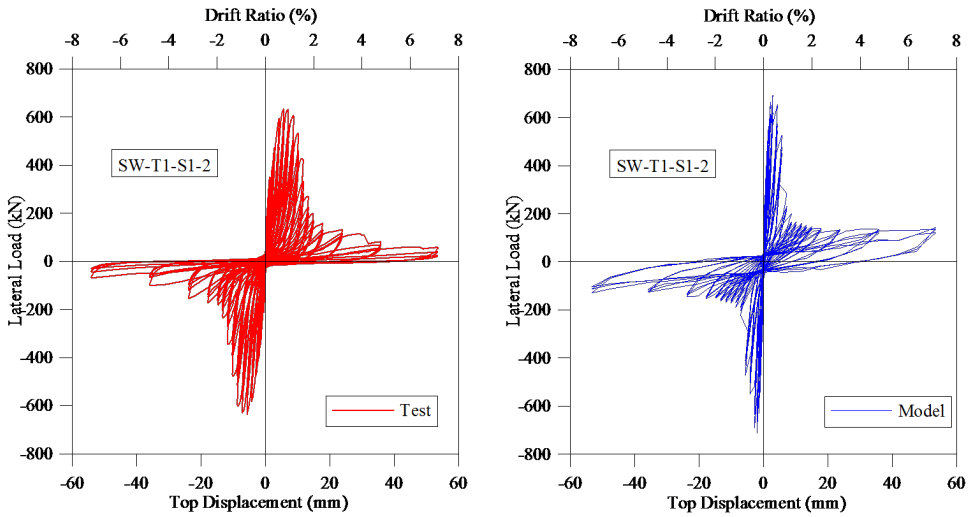

Figure 4.8. Lateral Load - Top Displacement Response of Specimen SW-T1-S1-2.

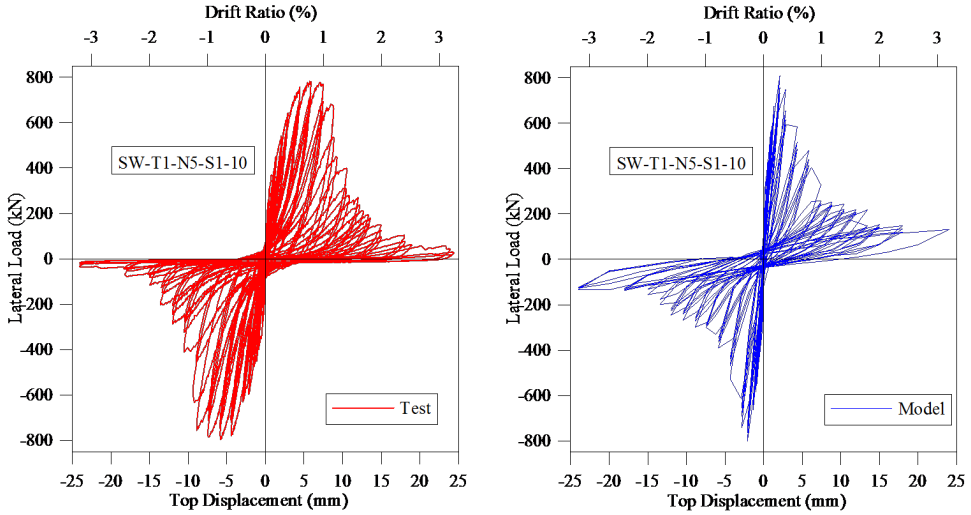

Figure 4.9. Lateral Load - Top Displacement Response of Specimen SW-T1-N5-S1-10.

Specimen SW-T1-N10-S1-11 was another Type 1 specimen, and was tested under 10% axial load level. Similarly to the case of specimen SW-T1-N5-S1-10 the model captures the lateral load capacity of the specimen (especially in the positive loading direction), overestimates its stiffness, underestimates its ductility, and reasonably represents its lateral load degradation and pinching characteristics as seen in Figure 4.10. This specimen experienced sudden strength degradation in the positive loading direction due to crushing of concrete, whereas degradation in the analysis results is more gradual, as is typically the case for the model.

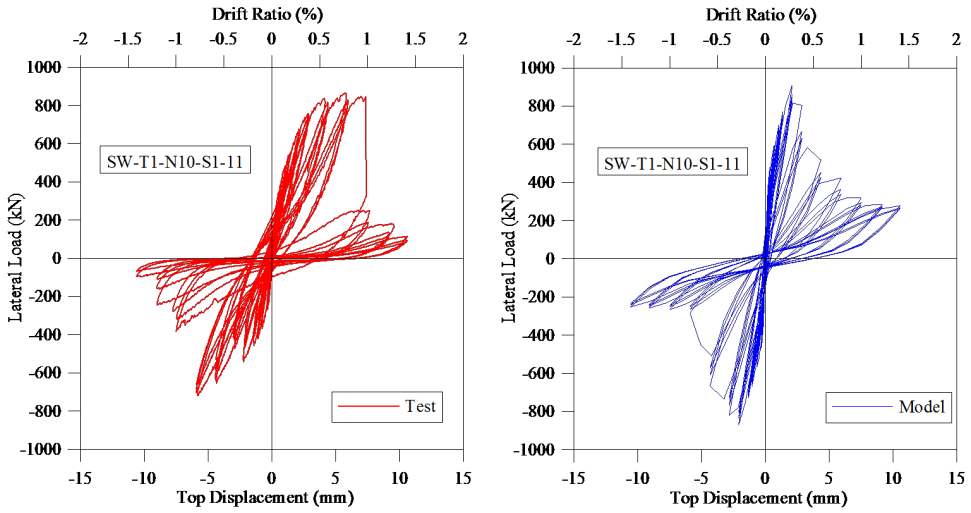

Figure 4.10. Lateral Load - Top Displacement Response of Specimen SW-T1-N10-S1-11.

Type 2 wall specimens had identical properties, with specimen SW-T2-S1-1 having lower concrete compressive strength compared to the remaining Type 2 specimens, due to the age of concrete during testing. Figure 4.11 shows the lateral load vs. top displacement response comparison for specimen SW-T2-S1-1. Although the initial stiffness of the wall is well captured by the model, the cracked stiffness is overestimated and its ductility underestimated. In both positive and negative loading directions, the model successfully predicts the lateral load capacity of the wall. For all Type 2 specimens, the failure mode was diagonal compression failure, leading to crushing at the base of the wall. Concrete crushing decreased the experimentally-measured lateral load capacity significantly at 1.5% drift. Although the model captures the degradation in lateral load capacity, the degradation in the model results initiates earlier and is more gradual. Similarly, for specimen SW-T2-S3-4 (Figure 4.12), the model accurately predicts the initial stiffness, and lateral load capacity of the wall, underestimates its ductility, and predicts a more gradual degradation in lateral load.

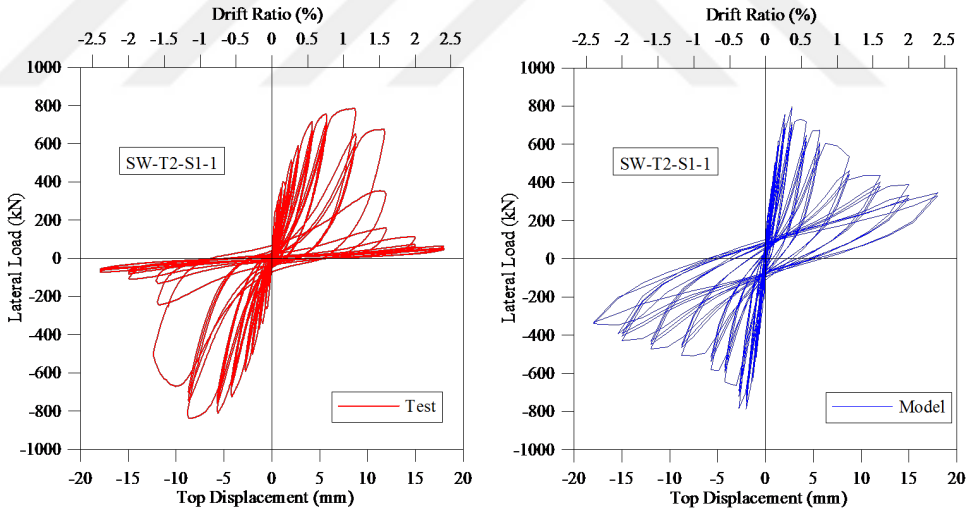

Figure 4.11. Lateral Load - Top Displacement Response of Specimen SW-T2-S1-1.

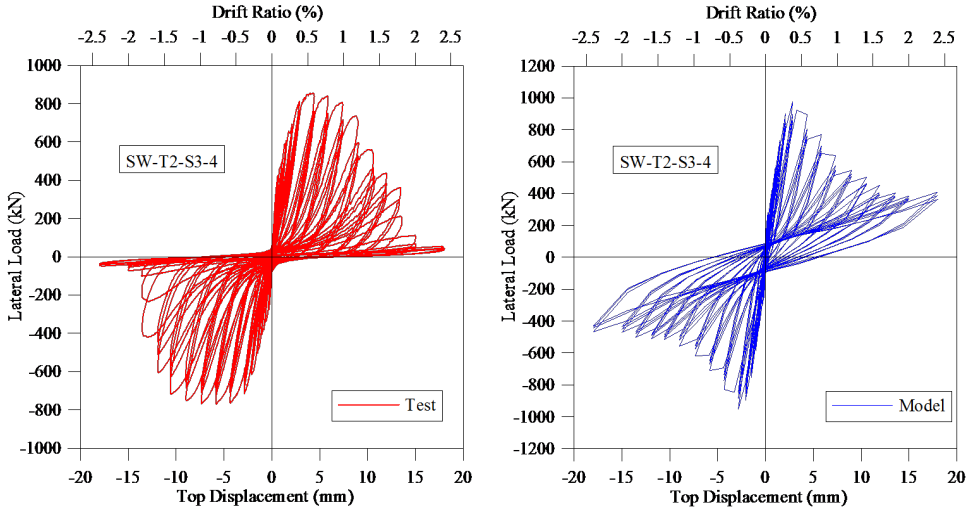

Figure 4.12. Lateral Load - Top Displacement Response of Specimen SW-T2-S3-4.

The Type 4 wall specimen SW-T4-S1-6 is the one with the lowest aspect ratio of 0.33, among the structural walls investigated in this study (FFigure 4.13). The failure mode of this specimen was similar to the Type 2 walls, as this specimen also failed due to crushing of concrete under diagonal compression. The associated degradation in lateral load capacity is reflected in the model results; however, the model predicts a less ductile behavior, with earlier and more gradual degradation in lateral load. As well, the lateral load capacity of the wall is notably overestimated by the model, especially in the negative loading direction. Pinching characteristics of the response as well as the stiffness of the wall are reasonably predicted by the model.

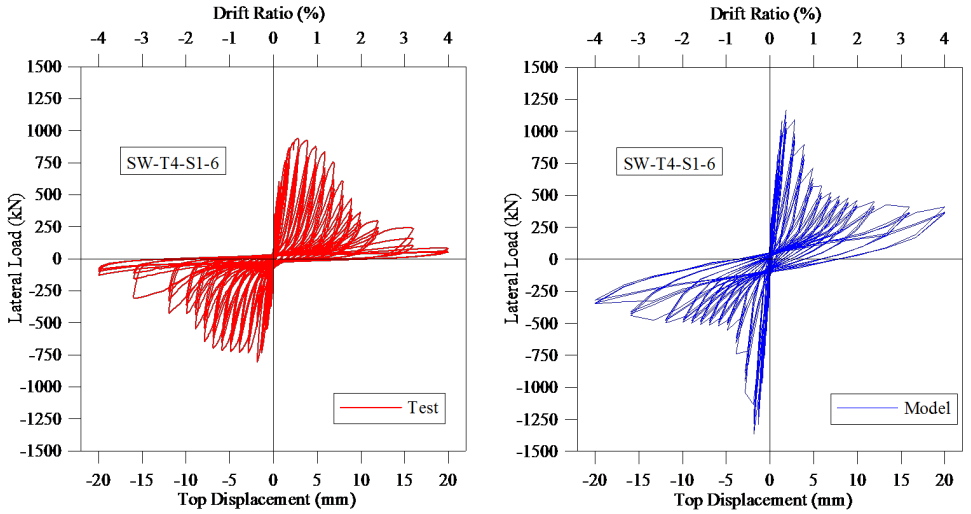

Figure 4.13. Lateral Load - Top Displacement Response of Specimen SW-T4-S1-6.

The Type 5 and Type 6 wall specimens were the most slender walls tested at Boğaziçi University, with an aspect of 1.00. Another common feature of these specimens was that they had high boundary reinforcement ratios. In the test results, after the lateral load capacity of these walls was reached, the walls maintained their capacity for several cycles. The response comparison for specimen SW-T5-S1-7 is shown in Figure 4.14. Lateral stiffness of the wall is captured by the model. Lateral load capacity in both loading directions, ductility, and pinching behavior are also reasonably predicted. However, the model tends to estimate more pronounced degradation in lateral load with increasing drift levels.

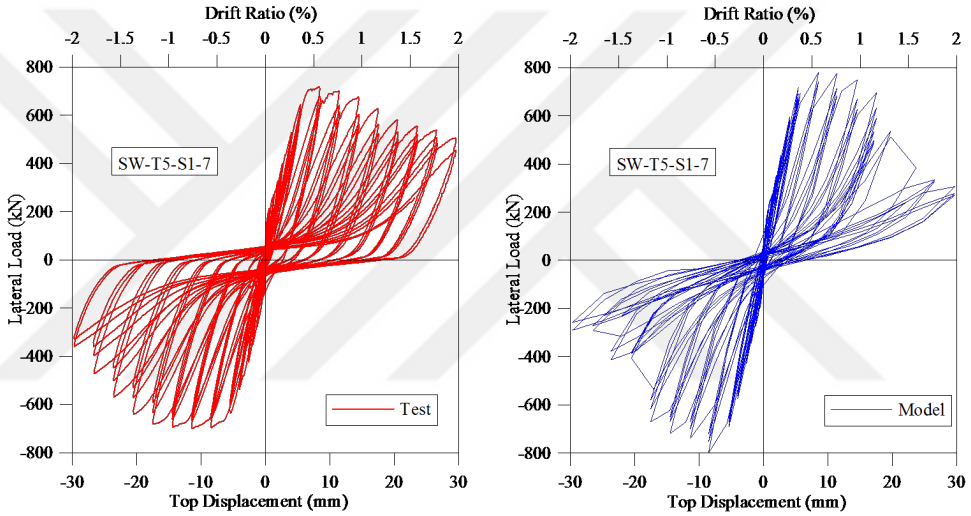

Figure 4.14. Lateral Load - Top Displacement Response of SW-T6-S1-7.

Type 3 specimens had a differentiating failure mode compared to the rest of the wall specimens tested at Boğaziçi University. Specimen SW-T3-S1-5 had low longitudinal boundary reinforcing ratio and failed under shear sliding along a single horizontal crack that spanned across the wall-pedestal interface. Boundary reinforcement of the wall yielded at very early drift levels, the horizontal crack propagated across the entire length of the wall-pedestal interface, and the response was governed by shear sliding along the crack. To represent this phenomenon, formation of a horizontal crack at the base of the wall was imposed on the model formulation. As observed in Figure 4.15, the analytical model fails to accurately represent the overall lateral load vs. top displacement response of the wall. Especially, unfavorable predictions were obtained for the lateral load capacity of the wall and pinching characteristics of the response. However,

parameters of the constitutive aggregate interlock and dowel action models (incorporating a friction coefficient of 1.0 for the compressive stresses in concrete perpendicular to the crack and a friction coefficient of 0.35 for clamping effect of reinforcing steel bars) had provided reasonable response predictions for the remaining specimens tested at Boğaziçi University.

A second analysis was conducted for this specimen, using a friction coefficient of 0.35 for both the compressive stresses in concrete perpendicular to the crack and for the clamping effect of reinforcing steel bars. The results of the new analysis are shown in Figure 4.16. As can be observed, decreasing the concrete stress friction coefficient to a value of 0.35 provided an improved prediction of the lateral load capacity of the specimen. However, the model still failed to represent the cyclic stiffness degradation (e.g., unloading stiffness) and pinching characteristics of the experimentally - observed response. In order to improve these features in the model prediction, a new hysteretic constitutive model formulation was developed and implemented, to represent the clamping effect of reinforcement on the shear aggregate interlock mechanism. Hysteric rules following the so-called Peak-Oriented Model (Figure 4.17) were implemented for the clamping effect on aggregate interlock (to replace the origin-oriented hysteretic rules in the original model formulation), where the unloading from the envelope follows the elastic stiffness of the shear (friction) stress vs. shear (sliding) strain envelope, zero stress is maintained until sliding direction is reversed, and reloading to the envelope in the opposite direction is peak-oriented. The cyclic strength degradation parameters were retained in the new Peak-Oriented hysteretic model.

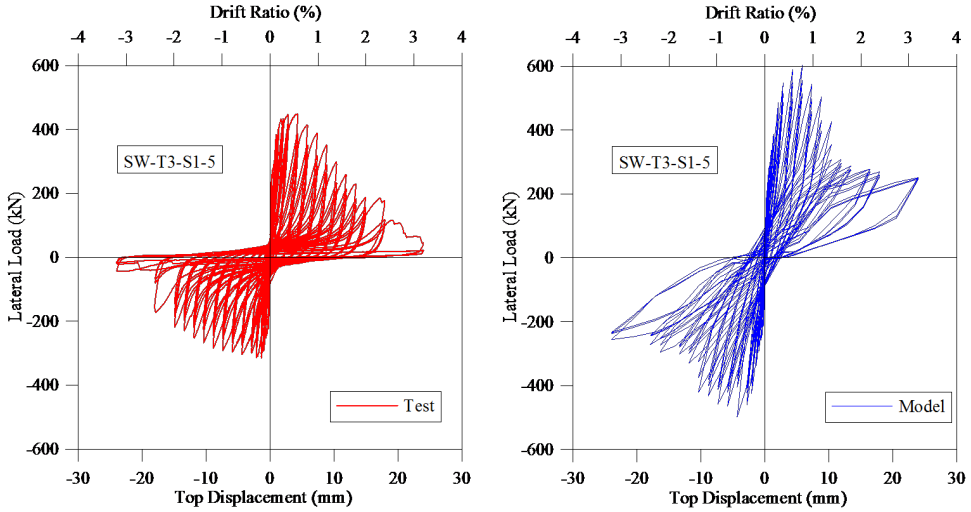

Figure 4.15. Lateral Load - Top Displacement Response of SW-T3-S1-5 (Original Model).

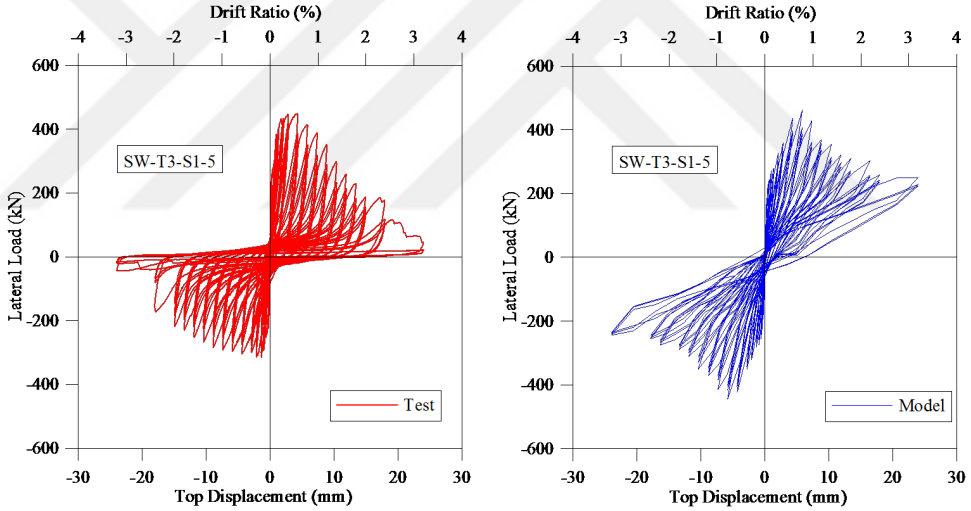

Figure 4.16. Lateral Load - Top Displacement Response of SW-T3-S1-5 (Concrete Friction Coefficient in Shear Aggregate Interlock Mechanism Reduced in the Model).

Using the new Peak-Oriented constitutive model for the clamping effect of reinforcement on the shear aggregate interlock mechanism across cracks, a third analysis was conducted for specimen SW-T3-S1-5. The lateral load vs. top displacement response comparison obtained using the updated model formulation is presented in Figure 4.18. As can be observed in the figure, the model now provides significantly improved predictions for the cyclic stiffness degradation and pinching characteristics of the response. The updated model reasonably predicts the lateral load capacity and ductility

of the wall, as well as hysteretic characteristics of the load-displacement response, including cyclic stiffness and strength degradation and pinching.

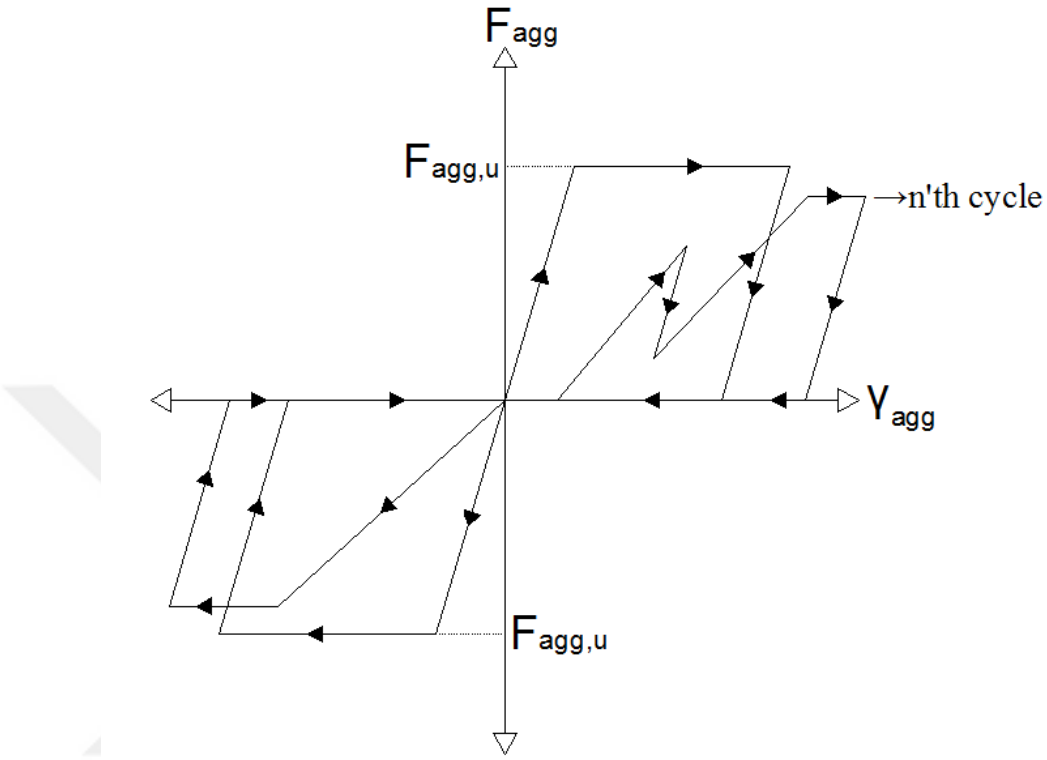

Figure 4.17. Peak-Oriented Model for Contribution of Reinforcing Steel on Shear Aggregate Interlock.

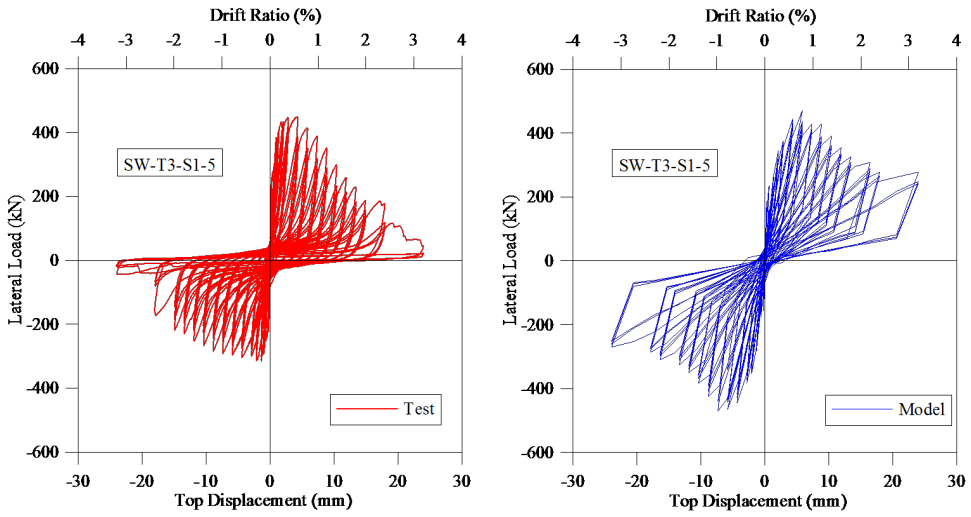

Figure 4.18. Lateral Load - Top Displacement Response of SW-T3-S1-5 (Peak-Oriented).

4.3. Overview

The aim of this chapter was to present the results of correlation studies conducted between the analytically-predicted and experimentally-observed lateral load vs. top displacement response of the wall specimens investigated in this study. The analytical model was subjected to the same loading conditions applied during testing including loading protocol and axial load conditions. For the walls experiencing shear sliding failure at the base, a horizontal crack was enforced on the model at the same location.

Response comparisons with test results on the low-rise wall specimens revealed that the model provides reasonable predictions of the lateral stiffness, lateral load capacity, degradation in stiffness and lateral load, hysteretic response shape, and pinching characteristics of the wall specimens investigated. The lateral load capacity of the walls was estimated by the analytical model fairly well, except for specimen SW-T4-S1-6 with an aspect (or shear-span-to-depth) ratio of 0.33, which is the lowest among all specimens. The model tends to underestimate the ductility of the wall specimens tested at Boğaziçi University, whereas it provides reasonably predictions of the ductility of the UCLA specimens. Cyclic strength and stiffness degradation, and pinching behavior in the load-displacement response of the walls were also captured reasonably well by the model.

5. SUMMARY AND CONCLUSIONS

5.1. Overview

The aim of this study was to validate and improve a finite element modeling methodology to simulate the hysteretic lateral load vs. displacement response of low-rise structural walls, whose behavior is governed by shear deformations. The constitutive modeling approach used is based on a fixed-strut-angle panel model formulation, and improvements were made on the constitutive panel model for better representation of the shear-aggregate-interlock effects in concrete and dowel action on reinforcing bars, which constitute the the shear stress transfer mechanism across cracks and thus significantly influence the lateral load behavior of low-rise walls with aspect ratios of 1.0 or less.

The model was calibrated for squat wall specimens tested by Massone (2006), Orakcal *et al.*, (2009), and Terzioglu (2011), and model predictions were compared with the experimentally-observed cyclic lateral load vs. displacement responses of representative specimens. Cyclic degradation parameters were implemented in the constitutive model formulations representing shear aggregate interlock effects along cracks and dowel action on reinforcement. In order to obtain better response prediction for walls experiencing shear sliding failure, an alternative peak-oriented hysteretic model was developed and implemented for representing the contribution of the clamping effect of reinforcement on the shear aggregate interlock mechanism, and formation of a horizontal crack at the base of the wall was imposed on the analytical model.

5.2. Conclusions

The following conclusions can be drawn based on the results obtained using the analytical model adopted in this study, upon comparison with the experimentally-observed response of low-rise structural walls:

- The adopted modeling approach is capable of simulating the nonlinear hysteretic response of low-rise structural walls under in-plane reversed-cyclic loading conditions, with an acceptable level of accuracy. Reasonable predictions were obtained for the experimentally-observed cyclic response characteristics of the walls investigated, including their lateral load capacity, stiffness, ductility, cyclic stiffness and strength degradation, hysteretic shape, and pinching behavior.
- The model tends to overestimate the lateral stiffness and underestimate the ductility of some of the wall specimens investigated. As well, in most cases, the degradation in lateral load predicted by the model is more gradual compared to experimental results.
- The model successfully represents the influence of axial load on the shear-controlled lateral load behavior of walls, which may be important considering that design codes and guidelines neglect the influence of axial load in calculation of the shear strength and stiffness of walls.
- It was observed that the cyclic strength degradation parameters implemented in this study on the constitutive models associated with shear aggregate interlock and dowel action mechanisms improves the accuracy of the model in predicting the loss of lateral load capacity and lateral stiffness at high drift levels. As well, consideration of strain penetration effects on the response provides improved model predictions for the initial stiffness of walls.

For walls experiencing shear sliding type of failure, an alternative hysteretic (peak-oriented) modeling approach was developed to represent the clamping contribution of reinforcing steel bars on the shear aggregate interlock mechanism along the cracks. Implementation of this new hysteretic model resulted in improved prediction of the lateral load response of walls exhibiting shear sliding failure.

5.3. Recommendations for Future Studies

The following recommendations can be made for future studies on the subject:

- A wider range of experimental data can be used to further validate the model and

improve its formulation (e.g., implementation of more refined constitutive models for aggregate interlock and dowel mechanisms, incorporation of reinforcing bar buckling and fracture under low-cycle fatigue, incorporation of bond slip), towards developing a more robust model formulation to simulate the response of walls with various response characteristics.

- Size effects (strain localization effects) can be considered in improving the formulation of the model, and the accuracy of model predictions for local responses (e.g., strains in concrete and steel) can be investigated.
- The model, either in its current state, or with a modified (possibly simplified) formulation, can be extended to conduct analytical studies on structural systems.

REFERENCES

Barda, F., 1972, "Shear Strength of Low-Rise Walls with Boundary Elements", Ph.D. Dissertation, Lehigh University, Bethlehem, Pennsylvania.

Bazant, Z. P. and P. G. Gambarova, 1984, "Crack Shear in Concrete: Crack Band Microplane Model", *Jounal of Structural Engineering*, Vol. 110, No. 9, pp. 2015-2035.

Belarbi, A. and T. C. Hsu, 1994, "Constitutive Laws of Concrete in Tension and Reinforcing Bars Stiffened By Concrete", *American Concrete Institute Structural Journal*, Vol. 91, No. 4, pp. 465-474.

Benjamin, J.R., and H.A. Williams, 1953, "Investigation of Shear Walls, Part 3 - Experimental and Mathematical Studies of Reinforced Concrete Walled Bents under Static Shear Loading", *Report No. 1, Department of Civil Engineering*, Stanford University, Stanford, California.

Chang, G.A. and J.B. Mander, 1994, "Seismic Energy Based Fatigue Damage Analysis of Bridge Columns: Part I-Evaluation of Seismic Capacity", *National Center for Earthquake Engineering Research.*

Clarke, M. J. and G. J. Hancock, 1990, "A Study of Incremental-Iterative Strategies for Non-Linear Analyses", *International Journal for Numerical Methods in Engineering*, Vol. 29, pp. 1365-1391.

Darwin, D., 1993, "Finite Element Analysis of Reinforced Concrete Structures II", *American Society of Civil Engineers Journal of Structural Engineering*, Vol. 1, pp. 203-232.

Filippou, F.C., E.G., Popov and V.V. Bertero, 1983, "Effects of Bond Deterioration on Hysteretic Behavior of Reinforced Concrete Joints", *Energy and Environmental*

Rerearch Center Report No. 83/19 Earthquake, Engineering Research Center, University of California, Berkeley, California.

Galletly, G.D., 1952, "Behavior of Reinforced Concrete Walls under Static Load", *Department of Civil and Sanitary Engineering*, Massachusetts Institute of Technology.

Gulec, C.K., 2009, *Performance-Based Assessment and Design of Squat Reinforced Concrete Shear Walls*, Ph.D. Thesis, State University of New York.

Gullu, M.F., 2013, *Finite Element Modeling Of Reinforced Concrete Structural Walls*, M.S. Thesis, Boğaziçi University.

Gullu, M.F., K. Orakcal, 2014, "Nonlinear Finite Element Modeling of Reinforced Concrete Structural Walls", *Proceedings, 2nd European Conference on Earthquake Engineering and Seismology*, Istanbul, Turkey, No. 1485.

He, X.G. and A.K.H. Kwan, 2001, "Modeling Dowel Action of Reinforcement Bars for Finite Element Analysis of Structures", *Computers and Structures*, Vol.79, No. 6, pp. 595-604.

Hirosawa, M., 1975, "Past Experimental Results on Reinforced Concrete Shear Walls and Analysis on Them", *Kenchiku Kenkyu Shiryo*, No. 6, pp. 277-280.

Horoz, B., 2015, *Modeling of Coupled Nonlinear Shear and Flexural Responses in Medium-Rise RC Walls*, M.S. Thesis, Boğaziçi University.

Husain, H.M., N.K. Oukaili and H.S. Muhammed, 2009, "Dowel Action Between Two Concretes", *Journal of Engineering*, Vol. 15, No. 2, pp. 3583-3605.

Ince, R., E. Yalcin and A. Arslan, 2006, "Size-Dependent Response of Dowel Action in RC Members", *Engineering Structures*, Vol. 29, pp. 955-961.

Kolozvari, K., T. Tran, J.W. Wallace and K. Orakcal, 2012, "Modeling of Cyclic Shear-

Flexure Interaction in Reinforced Concrete Structural Walls", *Proceedings, 15th World Conference on Earthquake Engineering*, Lisbon, Portugal, No. 2471.

Kolozvari, K., T. Tran, J.W. Wallace and K. Orakcal, 2014, "Modeling of Cyclic Shear-Flexure Interaction in Reinforced Concrete Structural Walls. I: Theory", *American Society of Civil Engineers Journal of Structural Engineering*, Vol. 141, No. 5, pp. 541-550.

Maekawa, K. and J. Qureshi, 1996b, "Computational Model for Reinforcing Bar Embedded in Concrete under Combined Axial Pullout and Transverse Displacement", *Proceedings of Japan Society of Civil Engineers*, Vol. 31, No. 538, pp. 227-239.

Maekawa, K. and J. Qureshi, 1997, "Stress Transfer across Interfaces in Reinforced Concrete Due to Aggregate Interlock and Dowel Action", *Journal of Materials, Concrete Structures, Pavements*, Vol. 34, No. 557, pp. 159-172.

Mander, J.B., M.J.N. Priestley and R. Park, 1988, "Theoretical Stress-Strain Model for Confined Concrete", *American Society of Civil Engineers Journal of Structural Engineering*, Vol. 114, No. 8, pp. 1804-1826.

Mansour, M.Y., T.C. Hsu and J.Y. Lee, 2002, "Pinching Effect in Hysteretic Loops of R/C Shear Elements", *American Concrete Institute Special Publications*, Vol. 205, pp. 293-321.

Mansour, M.Y. and T.C. Hsu, 2005, "Behavior of Reinforced Concrete Elements under Cyclic Shear", *American Society of Civil Engineers Journal of Structural Engineering*, Vol. 131, No. 1, pp. 44-53.

Martin-Perez, B. and S.J. Pantazopoulou, 1999, "Effect of Bond, Aggregate Interlock and Dowel Action on the Shear Strength Degradation of Reinforced Concrete", *Engineering Structures*, Vol. 23, pp. 214-227.

Massone, L.M., 2006, *Analytical and Experimental with Shear - Flexure Interaction in*

RC Walls, Ph.D. Thesis, University of California.

Mattock, H.A. and M.N. Hawkins, 1972, "Shear Transfer in Reinforced Concrete - Recent Research", *Precast/ Prestressed Concrete Institue*, Vol. 1, pp. 55-75.

Mau, S.T. and T.C. Hsu, 1986, "Shear Design and Analysis of Low-Rise Structural Walls", *American Concrete Institute Structural Journal*, Vol. 83, No. 2, pp. 306-315.

Menegotto, M. and E. Pinto, 1973, "Method of Analysis for Cyclically Loaded Reinforced Concrete Plane Frames Including Changes in Geometry and Non-Elastic Behavior of Elements under Combined Normal Force and Bending", *Proceedings, International Association for Bridge and Structural Engineering Symposium on Resistance and Ultimate Deformability of Structures Acted on by Well-Defined Repeated Loads*, Lisbon, Portugal.

Moradi, A.R., M. Soltani and A.A. Tasnimi, 2012, "A Simplified Constitutive Model for Dowel Action across RC Cracks", *Journal of Advanced Concrete Technology*, Vol. 10, pp. 264-277.

Oesterle, R.G., Fiorato, A.E., Johal, L.S., Carpenter, J.E., Russell, H.G., and Corley, W.G. 1976, "Earthquake resistant structural walls-Tests of isolated walls", *Report to National Science Foundation*, *Principal Component Analysis Construction Technology Laboratories*, Skokie, IL, 317.

Orakcal, K., D. Ulugtekin and L.M. Massone, 2012, "Constitutive Modeling of Reinforced Concrete Panel Behavior under Cyclic Loading", *Proceedings, 15th World Conference on Earthquake Engineering*, Lisbon, Portugal, No. 3573.

Orakcal, K. and J.W. Wallace, 2006, "Flexural Modeling of Reinforced Concrete Walls - Model Calibration", *American Concrete Institute Structural Journal*, Vol. 103, No. 2, pp. 196-206.

Orakcal, K., L.M. Massone, and J.W. Wallace, 2006, *Analytical Modeling of Reinforced Concrete Walls for Predicting Flexural and Coupled - Shear - Flexural Responses*, Pacific Earthquake Engineering Research Report No. EEC-9701568, Berkeley.

Orakcal, K., L.M. Massone, and J.W. Wallace, 2009, "Modeling of Squat Structural Walls Controlled by Shear", *American Concrete Institute Structural Journal*, Vol. 106, No. 5, pp. 646-655.

Orendil, A.E., 2014, *Analytical Modeling of Squat Walls with Shear-Controlled Responses*, M.S. Thesis, Boğaziçi University.

Palieraki, V. and E.N. Vintzileou, 2009, "Cyclic Behavior of Interfaces in Repaired/ Strengthened RC Elements", *Architecture Civil Engineering Environment*, No. 1, pp. 97-108.

Panagouli, O. and K. Iordanidou, 2013, "Study of the Residual Strength of an RC Shear Wall with Fractal Crack Taking into Account Interlocking Interface Phenomena", *Mathematical Problems in Engineering*, Vol. 2013, Article ID. 101484.

Pang, D. and T.C. Hsu, 1995, "Behavior of Reinforced Concrete Membrane Elements in Shear", *American Concrete Institute Structural Journal*, Vol. 92, No. 6, pp. 665-677.

Paulay, T., M.J.N. Priestley and A.J. Synge, 1982, "Ductility in Earthquake Resisting Squat Shearwalls", *American Concrete Institute Journal*, Vol. 79, No. 4, pp. 257-269.

Petrangeli, M., P.E. Pinto and V. Ciampi, 1999, "Fiber Element for Cyclic Bending and Shear of RC Structures. I: Theory", *Journal of Engineering Mechanics, American Society of Civil Engineers*, Vol. 125, No. 9, pp. 994-1001.

Powell, G. and J. Simons, 1982, "Improved Iteration Strategy for Nonlinear Structures", *International Journal for Numerical Methods in Engineering*, Vol. 17, pp.

1455-1467.

Saatcioglu, M. and S. Razvi, 1992, "Strength and Ductility of Confined Concrete", *American Society of Civil Engineers Journal of Structural Engineering*, Vol. 118, No. 6, pp. 1590-1607.

Sagaseta, J. and R. L. Vollum, 2011, "Influence of Aggregate Fracture on Shear Transfer through Cracks in Reinforced Concrete", *Magazine of Concrete Research*, Vol. 63, No. 2, pp. 119-137.

Soltani, M. and K. Maekawa, 2008, "Path-Dependent Mechanical Model for Deformed Reinforcing Bars at RC Interface under Coupled Cyclic Shear and Pullout Tension", *Engineering Structures*, Vol. 30, No. 4, pp. 1079-1091.

Soroushian, P., K. Obaseki, M. I. Baiyasi, B. El-Sweidan and K. Choi, 1988, "Inelastic Cyclic Behavior of Dowel Bars", *American Concrete Institute Structural Journal*, Vol. 85, No. 1, pp. 23-29.

Stevens, N.J., 1987, *Analytical Modeling of Reinforced Concrete Subjected to Monotonic and Reversed Loadings*, Ph.D. Thesis, University of Toronto.

Terzioglu, T., 2011, *Experimental Evaluation of The Lateral Load Behavior of Squat Structural Walls*, M.S. Thesis, Boğaziçi University.

Thermou G.E., V.K. Papanikolaou, A.J. Kappos, 2011, "Analytical Model for Predicting the Response of Old-Type Columns Rehabilitated with Concrete Jacketing under Reversed Cyclic Loading", *Conference on Computational Methods in Structural Dynamics & Earthquake Engineering*, Greece.

Thermou G.E., V.K. Papanikolaou, A.J. Kappos, 2014, "Flexural Behaviour of Reinforced Concrete Jacketed Columns under Reversed Cyclic Loading", *Engineering Structures*, Vol. 76, pp. 270-282.

Theodossius, P.T. and E. N. Vintzileou, 1987, "Concrete-to-Concrete Friction", *Journal*

of Structural Engineering, Vol. 113, No. 4, pp. 832-849.

Tran, T.A., 2012, *Experimental and Analytical Studies of Moderate Aspect Ratio Reinforced Concrete Structural Walls*, Ph.D. Thesis, University of California, Los Angeles.

Tran, T.A. and J.W. Wallace, 2012, "Experimental Study of Nonlinear Flexural and Shear Deformations of Reinforced Concrete Structural Walls", *Proceedings, 15th World Conference on Earthquake Engineering*, Lisbon, Portugal, No. 3913.

Tsai, W.T., 1988, "Uniaxial Compressional Stress-Strain Relation of Concrete", *American Society of Civil Engineers Journal of Structural Engineering*, Vol. 114, No. 9, pp. 2133-2136.

Ulugtekin, D., 2010, *Analytical Modeling of Reinforced Concrete Panel Elements under Reversed Cyclic Loadings*, M.S. Thesis, Boğaziçi University.

Vecchio, F.J. and M.P. Collins, 1986, "The Modified Compression-Field Theory for Reinforced Concrete Elements Subjected to Shear", *American Concrete Institute Structural Journal*, Vol. 83, No. 2, pp. 219-231.

Vecchio, F.J. and M.P. Collins, 1993, "Compression Response of Cracked Reinforced Concrete", *American Society of Civil Engineers Journal of Structural Engineering*, Vol. 83, No. 2, pp. 219-231.

Vintzeleou, E.N. and T.P. Tassios, 1987, "Behavior of Dowels under Cyclic Deformations", *American Concrete Institute Structural Journal*, Vol. 84, No. 1, pp. 18-30.

Vintzeleou, E.N. and T.P. Tassios, 1990, "Concrete-to-Concrete Friction", *American Society of Civil Engineering Journal of Structural Engineering*, Vol. 113, No. 4.

Vulcano, A., V.V. Bertero and V. Colotti, 1988, "Analytical Modeling of RC Structural Walls", *Proceedings, 9th World Conference on Earthquake Engineering*, Vol. 6, Tokyo-Kyoto, Japan, pp. 41-46.

Walraven, J.C. and H.W. Reinhardt, 1981, "Theory and Experiments on the Mechanical Behavior of Cracks in Plain and Reinforced Concrete Subjected to Shear Loading", *International Association for Bridge and Structural Engineering*, Vol. 26, No. 1A, pp. 1-68.

Wood, S.L., 1990, "Shear Strength of Low-Rise Reinforced Concrete Walls", *American Concrete Institute Structural Journal*, Vol. 87, No. 1, pp. 99-107.

Zhao, J. and S. Sritharan, 2007, "Modeling of Strain Penetration Effects in Fiber-Based Analysis of Reinforced Concrete Structures", *American Concrete Institute Structural Journal*, Vol. 104, No. 2, pp. 133-141.